



POLITECNICO DI TORINO

Department of Mechanical and Aerospace Engineering (DIMEAS)

Master's Degree Thesis in
Biomedical Engineering

Design and optimization of 3D Bioplotted scaffolds with a multi- layered architecture for osteochondral tissue regeneration

Supervisors

Prof. Gianluca Ciardelli

Dr. Chiara Tonda Turo

Dr. Elena Mancuso

Candidate

Marta Porta

Abstract

Knee osteoarthritis (OA) affects about 300 million people worldwide. In its early phases, OA involves the joint cartilage only; however, as it progresses the subchondral bone is more obviously involved, creating an osteochondral (OC) disease pattern. In recent years, 3D tissue engineered substitutes have emerged as promising alternative to traditional strategies (i.e. autografts transplantation, subchondral drilling, etc..). Although successful in many aspects, these 3D scaffolds lack in mimicking the complex architecture of the natural stratified OC tissue. To address this hurdle, in this study we investigated the development and optimization of a multi-layered scaffold with incorporated vertical porosity and ceramic content gradients, by using a 3D Bioplotter system. A tri-layered structure based on a composite of poly (ϵ -caprolactone) (PCL) and strontium-doped nano-hydroxyapatite (Sr-nHA) was designed. The overall architecture was made of three phases, printed continuously to mimic the native stratified OC tissue. Specifically, the first six layers (bottom portion) were made of PCL/Sr-nHA (20% w/w) in order to reproduce the bone counterpart, whereas to mimic the top cartilaginous tissue the upper portion was based on five layers made of PCL/Sr-nHa, with a lower ceramic content (10% w/w). The distance between the strands for both these portions was set to 0.8 mm. To simulate the harder mechanical properties of the calcified cartilage, the strands' distance of this intermediate layer was reduced to 0.7 mm. Bare PCL scaffolds were used as control for all the experiments performed. Physico-chemical characterization was conducted in order to prove the presence of both materials in the concentrations designed as well as to examine the surfaces' topography, porosity and wettability; while compressive tests were performed to assess the mechanical properties of the resulting tri-layer architecture. U2OS cells were used in order to assess the biological properties of the novel developed scaffolds. MTT colorimetric assay and DAPI qualitative assay showed an increased cells proliferation during the first week of seeding. Furthermore, The ALP activity showed osteoblast differentiation starting from 14 days of seeding. Alizarin Red staining evidenced calcium deposits after 7 day of seeding indicating cell-mediated scaffold's mineralization. In conclusion, based on the physico-chemical and biological characterization results, the as produced PCL/Sr-nHA scaffold, both in terms of material composition and architecture, demonstrated to be a promising candidate towards the development of a functional implant for OC tissue regeneration.

Acknowledgment

I would like to acknowledge everyone who has helped in the completion of this thesis and their great support during my studies.

Firstly, I would like to thank my supervisors Prof. G. Ciardelli and Dr. C. Tonda Turo of the Politecnico di Torino for giving me the opportunity to join the Ulster University, and for ensuring a good support, also from a distance, for the development of this work.

I sincerely would like to thank my supervisor Dr. Elena Mancuso of Ulster University for her constant encouragement, passionate participation, knowledge and patience during my studies. Thanks Elena for consistently allowing this paper to be my work but steering me in the right direction anytime I needed help or advices. Thanks Daniele for introducing me to the 3D Bioplotter showing me its 'secrets'. Thanks Josephine for the introduction to the cells and biomaterials world and all your comments.

I would also like to thank the experts and PHD students who were involved in the validation survey for this research project: Dilli, John, Naomi, Kieran, Michael and Eleni.

During my time in Belfast I met many great people. Special thanks to Sashi, Niamh, Pardys, MJ, Appoorva, Chris, Bruno, Daniele, Valentina and Jeremy for making that time in NIBEC so valuable and all your support. I have had the good fortune to share the workspace with great students who were always helpful and cheering during all those less sunny days of my studies in the always cloudy Northern Ireland.

Finally, I would like to acknowledge my 'old' friends, that always sustained me even if they were far, and my family who encourage me to undertake this experience and who have been very patient with me, especially these last months. Many thanks for your support!!!

Acronyms and Abbreviations

2D, 3D	2-dimensional, 3-dimensional
3DP	3-dimensional printing
AB	Antibiotics
AC	Articular cartilage
AM	Additive Manufacturing
ALP	Alkaline phosphatase
BCA	Bicinchoninic Acid
BTE	Bone tissue engineering
Con I	Collagen Type I
Col II	Collagen Type II
DAPI	4',6-diamidin-2-fenilindolo
DW	Deionized water
ECM	Extra cellular Matrix
FBS	Fetal Bovine Serum
FDA	Food and Drug Administration
FDM	Fused Deposition Modeling
FTIR	Infra-red Fourier Transform
HA	Hydroxyapatite
μCT	Micro-computed tomography
mRNA	Messenger ribonucleic acid
MTT	Methylthiazol tetrazolium
OA	Osteoarthritis
OC	Osteochondral
OP	Osteopontin
PBS	Phosphate buffered saline
PCL	Polycaprolactone
PFA	Paraformaldehyde
SB	Subchondral bone
SEM	Scanning electron microscopy
Sr-nHa	Strontium-doped hydroxyapatite

TE	Tissue Engineering
TGA	Thermogravimetric analysis
U2OS	Human Bone Osteosarcoma

Table of Contents

Introduction.....	9
Aim and objectives.....	11
Thesis structure.....	12
Chapter 1: Human osteochondral tissue structure and function.....	15
1.1 Osteochondral Unit (OC) - The components of osteochondral tissue.....	15
1.2 Subchondral bone and calcified cartilage.....	16
1.3 Articular cartilage.....	17
1.4 The osteochondral tissue as a gradient tissue.....	19
1.5 Osteoarthritis.....	21
1.5.1 Introduction and epidemiology.....	21
1.5.2 Changes in the OC unit during the evolution of OA disease.....	24
1.5.3 OA current treatment strategies.....	27
1.6 Properties and functions of OC unit.....	30
Chapter 2: State of the art in OC tissue engineering.....	31
2.1 OC Tissue Engineering.....	31
2.2 OC tissue-like scaffold requirement.....	32
2.2.1. Development of biphasic and multiphasic scaffolds.....	34
2.3 Materials and fabrication Techniques for OC- multi-layered scaffolds.....	39
2.3.1 Composite biomaterials.....	40
2.3.2 Additive manufacturing technologies and 3D bioprinting.....	42
2.3.3. Clinical Progresses and Insight.....	44
2.4 Cells for OC tissue engineering.....	45
2.5 Cell/scaffold interaction.....	47
2.6 Challenges for the development of OC TE strategies.....	49
Chapter 3: Materials and methods.....	51
3.1 Scaffold design and preparation.....	51

3.1.1	Materials.....	51
3.1.2	Scaffold design.....	51
3.1.3	Scaffold fabrication.....	52
3.2	Scaffold's chemical and physical characterization techniques.....	54
3.2.1	FTIR analysis.....	54
3.2.2	Contact angle analysis	56
3.2.3	TGA analysis.....	57
3.2.4	SEM analysis.....	59
3.2.5	Scaffold mechanical behaviour.....	61
3.2.6	Micro CT analysis.....	62
3.2.7	Theoretical calculation of scaffold's porosity.....	66
3.3	<i>In vitro</i> characterization.....	67
3.3.1	Scaffolds sterilization.....	68
3.3.2	Cell seeding.....	69
3.3.3	Cell viability: MTT for cells metabolism measurement.....	69
3.3.4	Cell viability: DAPI staining.....	71
3.3.5	Cell morphological analysis.....	73
3.3.6	Osteogenic potential.....	74
3.3.7	Mineralization potential.....	76
3.4	Statistical analysis.....	77
Chapter 4: Results.....		78
4.1	Introduction.....	78
4.2	Characterization of precursor powders and extruded filaments.....	79
4.2.1	FTIR analysis.....	79
4.2.2	TGA analysis.....	81
4.3	Scaffold 3D model and fabrication.....	83
4.4	Characterization of extruded surfaces.....	85
4.4.1	Contact angle analysis of printed materials.....	85
4.4.2	SEM analysis.....	86
4.5	Characterization of scaffold's architecture.....	87

4.5.2 Micro CT analysis.....	87
4.5.2 Scaffold porosity.....	89
4.6 Characterization of mechanical properties on the printed scaffolds.....	89
4.7 Cells viability.....	91
4.7.1 Cell metabolism: MTT assay.....	91
4.7.2 Cell attachment: DAPI assay.....	92
4.8 Cell adhesion and morphology: SEM analysis.....	95
4.9 Osteogenic potential.....	97
4.10 Mineralization potential.....	99
Chapter 5: Discussions.....	101
5.1 Introduction.....	101
5.2 Scaffold design and production.....	101
5.3 Chemical topographical and mechanical characterization of tri-layered printed PCL/ Sr-Ha scaffold.....	103
5.4 <i>In vitro</i> response of U2OS cells cultured on Tri-layered PCL/SrHa scaffold.....	106
Chapter 6: Conclusions and Future perspective.....	109
6.1 Conclusions.....	109
6.2 Future perspective.....	110
Bibliography.....	112

Introduction

Osteoarthritis (OA), representing the most common form of arthritis, affects 300 million people worldwide, and it is considered the main cause of permanent disability and the third cause of temporary workplace incapacity (1). Clinically, OA manifests as a loss of the articular surface in synovial joints, often leading to discomfort, chronic pain, instability and a reduction of joint movement (2). The high prevalence of the disease and the large clinical burden (36 million ambulatory care visits and 750,000 hospitalizations in 1997 in US) is estimated to increase because of the progressive aging population and obesity incidence (3). Osteochondral lesions, developing as both cartilaginous and bone tissue degeneration, are notably complex injuries. The complexity is due to the stratified and graded structure of the OC tissue (articular cartilage, calcified cartilage and subchondral bone), the complex biological and mechanical development of the disease that involves a strong crosstalk between compartments and the lack of regenerative activity of the hyaline cartilage (2) (4) (5). Different clinical techniques have been used for the treatment of this disease such as debridement, chondrocytes implantation, bone marrow stimulation techniques, grafts and mosaicplasty (6). However, surgical strategies have limitations in tissue repair, including grafts deterioration, lack of integration into native tissue and insufficient mechanical properties, often leading to unsatisfactory patient outcomes (7) (8).

As a result, the development of tissue engineering (TE) techniques for the treatment of OA is of pressing interest. Although, the different properties presented by the OC unit makes challenging the integration and stability of the newly formed tissue at the cartilage–bone interface. Innovative TE strategies, allowing the possibility to fabricate scaffolds with heterogeneous composition and graded properties, and mimicking the hierarchical and stratified structure of the OC unit, have prevented the progress of restorative solutions in this field (9) (10). Various attempts have been presented in the literature, these are classified into monophasic, bi-phasic and tri-phasic scaffolds. Several works in the literature have been reported the limitations of the monophasic scaffolds, since they are not able to properly simulate the OC biological environment, and also they are ineffective to mimic cartilage/bone tissue interface, which is characterized by anisotropic functions and structural properties (11).

In recent years, biphasic tissue engineered scaffolds, based on the combination of a cartilaginous and a bone-like phase, and multi-phasic scaffolds have been investigated as an alternative approach (12). A big advantage introduced with these strategies is the possibility to optimize different parts of the scaffold by combining diverse material formulations as well as fabrication technologies. Also, these strategies allow the addition of specific growth factors as well as appropriate chemical, mechanical and biological stimuli, in order to mimic both cartilage and bone properties and promote cells attachment, proliferation and differentiation (13). However, the issues of delamination, less accurate graded 3D structure, as well as poor mechanical properties and interface stability are limiting their clinical investigation (14) (15). Additive manufacturing processes and extrusion printing have been developed for the fabrication of complex tissue engineered scaffolds with tailorable mechanical properties and porous design, obtained by the implementation of computer CAD models. Additionally, the possibility to print different materials continuously allows the fabrication of scaffolds with multiphasic architectures, providing selective biomimeticity for the OC compartment, and also quite importantly reducing production's costs by using a single-step manufacturing process (16). Composite materials, based on polymers (i.e. PCL and poly (lactic-co-glycolic acid)) and ceramics (i.e. calcium phosphate, HA and doped-HA) , have been widely used in OC tissue engineering since by tailoring their concentration, they provide final properties specific for each tissue (i.e. bioactivity, mechanical properties etc.). In order to solve the still open challenges in the OC TE field, the main goal of this thesis is the design and optimisation of a 3D composite scaffold with a multi-layered architecture for OC tissue repair and regeneration. The study aimed to develop an innovative scaffold-based strategy with tailored properties in each scaffold's layer, thus promoting targeted regenerative processes and providing a good stability at the interface between the cartilage and the bone-like tissue compartments. The achievement of the seamless triphasic and biomimetic structure, obtained by using a single-step 3D multi-material manufacturing process, may represent a ground-breaking solution in OC TE, providing further insights towards the fabrication of patient-specific, cost-effective solutions. In this work an advance 3D Bioplotter system was used to produce 3D printed OC-tissue like substitutes with a high-level control on materials' composition and tailorable final inner design. Specifically, the scaffolds consisted of a tri-layered structure based on a PCL matrix doped with strontium-substituted hydroxyapatite (Sr-HA).

The content of the ceramic phase decreased along the structure going from the bottom (bone layer, made of PCL/Sr-nHa; 20% w/w) to the top (cartilaginous layer, made of PCL/Sr-nHa; 10% w/w), reproducing the complex stratified structure of the osteochondral (OC) unit. Additionally, the inner pattern of the scaffold was optimized to better simulate the mechanical and structural properties of the OC unit. The distance between the strands for both these portions was set to 0.8 mm. To simulate the harder mechanical properties of the calcified cartilage, the strands' distance of this intermediate layer was reduced to 0.7 mm. Bare PCL scaffolds were used as control for all the experiments performed. Scaffolds' production was followed by the physico-chemical characterization of the samples. The investigation started with the chemical analysis of the printed filaments using FTIR and TGA technologies, proceeded with the morphological and topographical structure characterization of the printed surfaces using SEM scansions contact angle measurement, with the characterization of scaffold's geometry and morphology and the calculation of the porosity of the entire structure, obtained by μ -CT scansions, and then with the mechanical characterization. Finally, the *in vitro* tests are aimed to test the biocompatibility of the printed materials of the scaffold. The viability of U2OS cells is analyzed by qualitative and quantitative assays (MTT assay, DAPI staining), cell attachment is explored by SEM scansions after chemical fixation on the substrates, osteogenic potential is quantitatively measured with the ALP enzymatic activity detection and scaffolds' mineralization is explored by Alizarin Red staining.

Aim and objectives

The main aim of this work study was to explore a new approach for the development of a reproducible and functional scaffold able to mimic the complex OC unit and enhance its repair and regeneration. The improved physico-chemical, structural and biomimetic properties of this device, along with its the reduced costs made possible by using the same sustainable manufacturing process, which is based on a multi-material solvent-free extrusion system, are aimed to lead to a breakthrough in the treatment of OC defects.

In order to achieve the main aim, different objectives (OBs) were set. Particularly these are:
-OB1: the optimization of the biomaterial formulations toward the scaffold fabrication;

- OB2: the manufacturing of the 3D scaffold with a tailored design and composition;
- OB3: the optimization of the printing parameters for each material formulation;
- OB3: the evaluation of the resulting 3D scaffold performance in terms of physico-chemical and mechanical properties.
- OB4: the assessment of the biocompatibility and the biological performances of the scaffold.

Thesis structure

The first Chapter provides an introduction about the OC unit and its main components. The understanding of the complex structure and composition of the OC unit, as well as the properties and functions played into the joint's site, is crucial for the achievement of a suitable solution for OC defect repair. In this Chapter will be also reviewed the main concept of Osteoarthritis (OA) disease, its biological progression and the changes induced on the OC compartments during its development. The current challenges on the treatment of this pathology and the main surgical strategies adopted for the OC reconstruction are also investigated.

The second Chapter reports the actual strategies used in Tissue Engineering for OC treatment and tissue repair in terms of method and manufacturing process, but also the materials currently used will be examined. The increasing use of additive manufacturing processes such as 3D bioprinting will be inspected, converging around the possibility to achieve biomimetic multilayered scaffolds by multiple combination of different materials with the same fabrication process. The chapter will focus on the recent wide use of composite ceramic/polymer materials, which matching the physiological composite and complex structure of the OC tissue can represent an optimal strategy to obtain biomimetic and structurally suitable structures. Finally, the importance of the use of cells in tissue engineering, in terms of active source for tissue engineering that provides tissue integration and extracellular matrix regeneration, will be presented. The last section of the chapter is aimed to illustrate the influence of scaffolds' chemical, physical and biological characterization over cells' growth and structure's osteointegration.

In Chapter 3 the material and the methods used in this study are discussed. The presentation starts with the scaffold's design and fabrication methods, focusing on the optimization of the 3D printing parameters for all the used materials. It will follow the description of the equipment used for the chemical and physical characterization of the scaffolds, starting from the precursors powders and following with the extruded filaments, printed surfaces and the final built scaffold's structure. The *in vitro* tests performed on the printed samples are then described in terms of cells' type used, seeding methodology and type of assays performed to test the biocompatibility of the scaffolds. In Figure 1 a flow chart representing the main steps achieved for this work is presented.

Chapter 4 is dedicated to the presentation of the results of the study. The chemical and physical characterization involved FTIR analysis on the precursor powders used for the printing scaffolds; FTIR and TGA for the study of printed filaments' compositions; SEM imaging and contact angle for the analysis of the extruded surfaces' topography as well as wettability. The μ -CT evaluation of the scaffold's porosity and morphology will be followed by the data of the mechanical properties of the scaffolds, obtained from the compressive tests. Finally, the cell study's results and the scaffold's biocompatibility will be discussed. The examination will start with the observation of the cells' proliferation and viability on the seeded scaffolds; it will follow a presentation about the identification of cells' potential osteogenic activity during their culture on the substrates and an analysis of the mineralization of the scaffolds.

In Chapter 5 a discussion about the obtained results of the study will be presented. Initially, the feasibility of the scaffold and the optimization of the printing parameters for the achievement of the functional reproducible and reliable multilayered structure will be discussed. It will follow the analysis of the physico-chemical and mechanical results investigating the need to resemble the natural OC tissue. A discussion about the obtained biocompatibility of the scaffold in terms of cell viability, attachment, osteogenic and mineralization potential will be presented. Finally, the conclusions of this work revealed from the obtained results and discussions will be submitted.

The sixth Chapter is dedicated to the analysis of future works directions, further improvement for the study and current challenges open in OC Tissue Engineering.

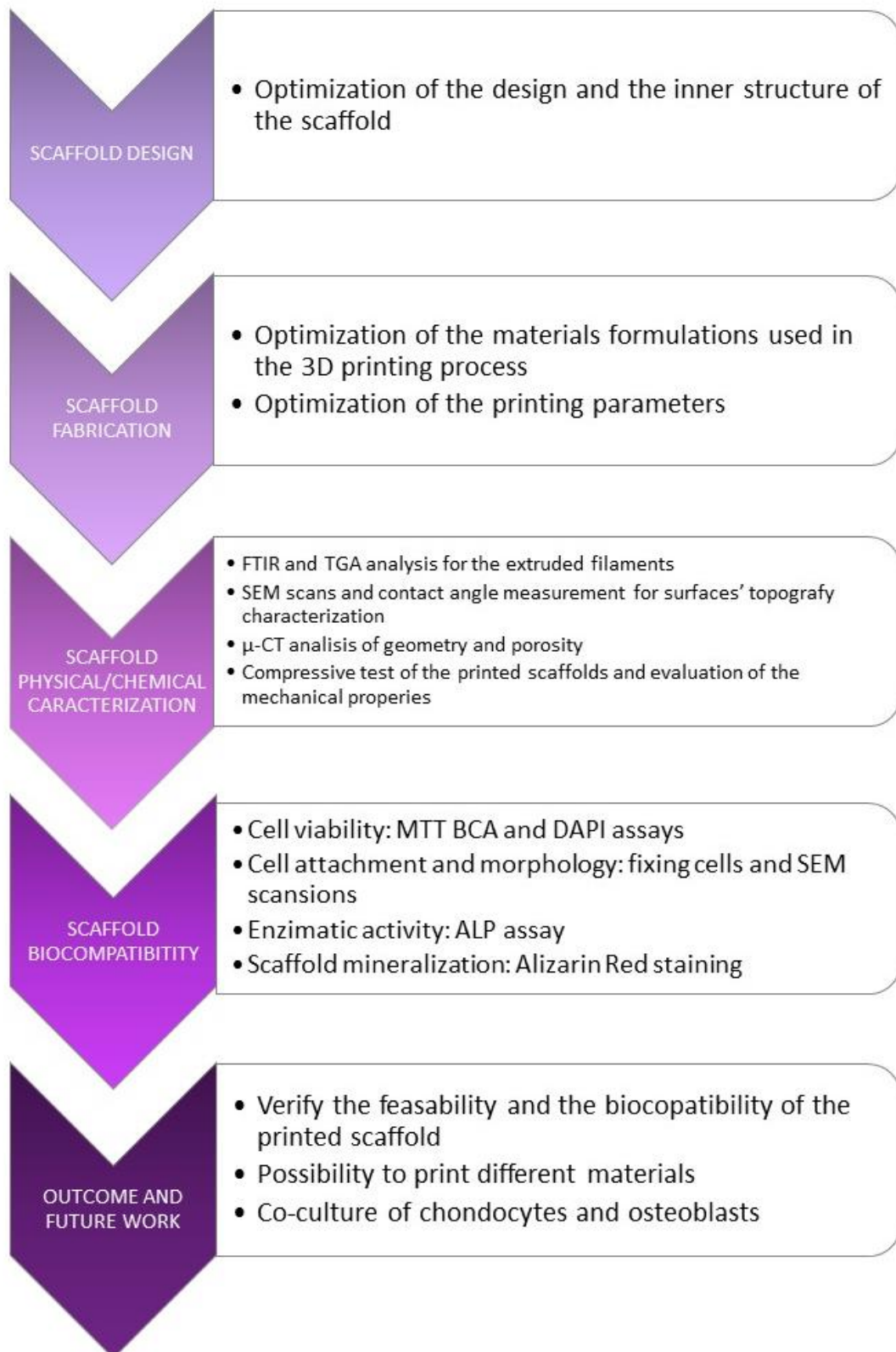


Figure 0 Flow chart describing the methodology adopted in this study for the achievement of the Tri-layer scaffold for OC tissue repair and regeneration

Chapter 1: Human osteochondral tissue structure and function

1.1 Osteochondral Unit (OC)

Human joints are complex anatomical structures that separate two or more adjacent elements of the skeletal system to form functional units, uniquely adapted to permit constrained motion (2). The OC unit of the articular joint is a highly organized structure formed at its most basic level by two core components: the subchondral bone and the articular cartilage. The subchondral bone is further divided into the subchondral bone plate, which represents the terminal part of the cancellous bone tissue, and the calcified cartilage zone (17). Their separation line takes the name of 'cement line' while the line that defines the transition between the calcified cartilage and the articular cartilage is called 'tide marker'(4) (18). In Figure 1.1 the main components of the OC unit are represented.

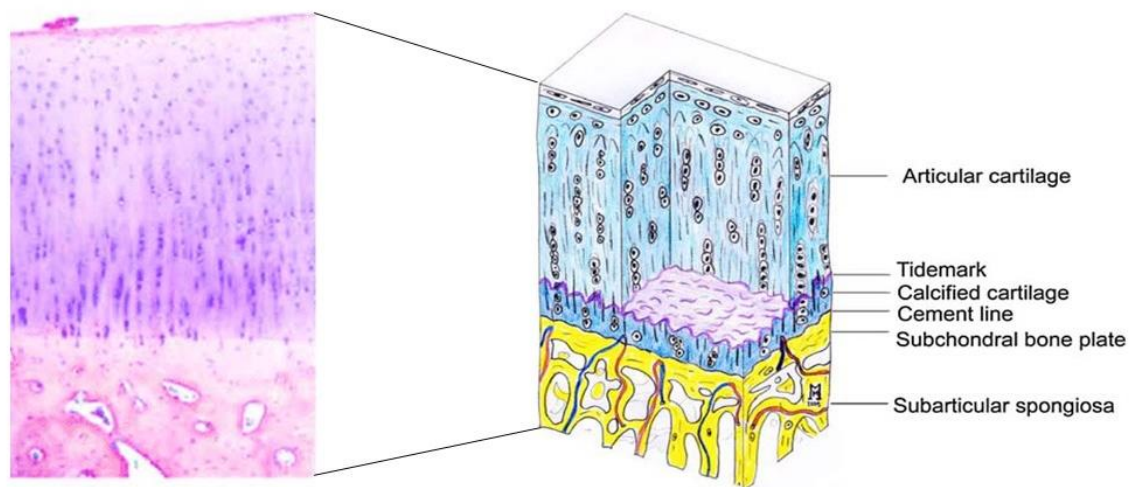


Figure 1.1 Schematic representation of osteochondral tissue and its main components. Adaptation from (3)

Both the subchondral bone and the articular cartilage consist of connective tissue characterized by cells dispersed in the Extra Cellular Matrix (ECM) whose composition is crucial to provide structural, mechanical and chemical stimuli for tissue's functionality and cells sustainment.(19)

1.2 Subchondral bone and calcified cartilage

The subchondral plate consists of two mineralized layers, which together form a single unit, separating the articular cartilage from the bone marrow. The subchondral plate or cortical endplate is used to refer to the layer lying immediately in contact with the cancellous bone. This region, being made of bone tissue, consists mainly of collagen type I and it is composed of lamellated sheets of parallel collagen fibrils, which continue into the lamellae of the trabecular bone. Structurally it is composed by a collagenous matrix, that provides flexibility, and in which the inorganic phase (hydroxyapatite crystals), with a percentage around 85% on the dried weight, is dispersed to enhance tissue's hardness and strength. Bone cells entrenched into the matrix compose a relatively small amount of the bone volume, but they play an important role into the bone functionality. The osteocytes represent the mature bone tissue cells located into lacuna, contributing to maintain the mineral concentration of the matrix. Osteoblasts are considered osteocytes' precursors and their functionality is related to new tissue's formation while osteoclasts are large multinucleate and originated from macrophages cells, responsible for bone resorption or breakdown. This cells, binding the bone matrix protein vitronectin, secrete acid and proteases, dissolving the mineral of bone and destroying the ECM matrix (20) (21). Osteoclasts also help in blood calcium regulative activity (22).

The subchondral plate presents structural characteristics similar to the trabecular bone tissue: volume fraction in a range between 6% to 36%, trabecular thickness of 100-190 μm , and space between them in a range of 320-1670 μm (23). The thickness of the subchondral plate is not uniform along the articular surface as well as its density distribution. They vary depending on the joint morphology and the mechanical situation reflecting the long-term stress acting on the site, in a range approximately between 100 to 900 μm . Both thickness and density distribution along the surface are associated to the sum of the mechanical stimuli that acts on the subchondral plate, since bone tissue can be remodelled towards an optimized distribution of strain-energy density (24) (25) (26). In fact, bone tissue is characterized by the capacity to react to critical stimuli, enhancing the production or absorption of the ECM (17). This process, called bone turnover, involves the ongoing balance between osteoblasts and osteoclasts activity, guaranteeing a constant and suitable remodelling of the bone in the healthy tissues (27). However, in abnormal states of rapid

bone remodelling, the increased rate of bone turnover interrupts the phase of mineral production, leading to a state of relative hypo-mineralization, associated with the reduction of bone stiffness. On the other side, in states of low bone turnover, the continued deposition of minerals tends to increase bone stiffness so that the bone is more resistant to mechanical solicitation and deformation (2).

The second part of this compartment, the calcified cartilage, represents the interface region between the subchondral bone and the articular hyaline cartilage, and it provides the function of good adhesion between the two layers. The tide mark that separates the two regions is not a straight line across a joint, but a complex three-dimensional structure that corresponds to the mineralization front of the calcified cartilage and provides a gradual transition between the two dissimilar parts (5)(11). Furthermore, it is functional to transmit mechanical stress and biological stimuli from the softer cartilage tissue to the harder subchondral bone plate, and it plays an important role in transferring fluids to each layer. Its composition is also made of a mixture of the components of the two adjoining layers. The amino acid content of the dry tissue is 20.16%, type II collagen, which characterizes the hyaline cartilage structure, is 13.69%, while the inorganic constituent, consisting in the low crystallizing hydroxyapatite, is found to be 65,39% of the dry weight (28). This area is populated by chondrocytes (cartilage cells) with a hypertrophic phenotype, which uniquely produces collagen type X and can calcify the surrounding matrix (29).

1.3 Articular cartilage

Articular cartilage is an avascular and a-neural tissue consisting of water for the 70% and two major organic components: type II collagen and aggrecans. The maintenance of this balance is due to chondrocytes, the main articular cartilage's cell type, and is crucial for keeping joint interface function. Chondrocytes cover just 1%-5% of the total cartilage volume and in mature tissue present a low proliferative and metabolic state (18) (30). The physical properties of articular cartilage are characterized by the fibrillar collagen network, which provides tensile strength, and by the entrapped proteoglycan aggregates, which provide compressive resilience. During compression, the large quantity of water molecules associated with the hydrophilic glycosaminoglycan chains and the charged solutes are

extruded. When compression stress is released, the proteoglycans have sufficient fixed charge to osmotically reabsorb the water and small solutes into the matrix, resulting in restoration of the original cartilage shape.

Cartilage also provides a unique articulating surface with a low coefficient of friction. This property is facilitated by a boundary layer of lubricants, such as lubricin and hyaluronic acid, which are produced by chondrocytes and synovial cells. Furthermore, joint motion and mechanical loading induce the movement of synovial fluid across the cartilage, enhancing the diffusion of molecules into cartilage and thus providing nutrition(2). The magnitudes of the contact pressure at any one location may typically go from zero to a large value and then back to zero in some fraction of a second. The joint pressures imposed by these intermittent loads introduce very high cyclic hydrostatic pressure in the bound and unbound intercellular fluid phase of cartilage, known as the interstitial fluid. The pressurization of the interstitial fluid component of cartilage can ultimately be credited both for providing the excellent lubrication between the two cartilage layers and for distributing as well as transmitting the joint forces to the underlying bone tissues in an efficient manner (31). Depending on the type of joint and the subject, the hyaline cartilage has a thickness in the range of 1 to 4 mm, and it could be divided into three different layers, which are Superficial, Middle and intermediate zone as it is shown in Figure 1.2 (32).

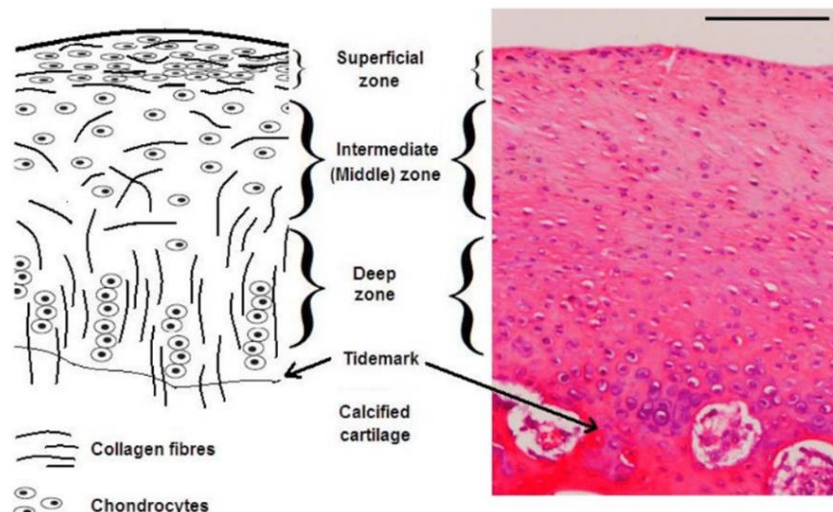


Figure 1.2 Representation of the hyaline cartilage's structure(left) The histological image (haemotoxylin and eosin (H&E) staining) on the right is taken from the femoral condyle of a rabbit knee joint and demonstrates the distribution of chondrocytes within the different zones(right) (32)

The layers present differences in both composition and chondrocytes morphology organization. In the superficial zone, the chondrocytes appear flat in shape at proximity to each other, and the collagen fibres are aligned parallel to the articular surface. In the intermediate zone, chondrocytes are oblique in shape and collagen fibres are randomly organized in different directions (30). The deep zone is characterized by chondrocytes with spherical but elongated shape and displaced in columns. The collagen fibres in this zone are oriented perpendicularly to the articular surface and penetrate through the tidemark into the calcified cartilage to provide structural stability between the two compartments (32). Despite the underneath subchondral bone, articular cartilage is structurally deficient in vascular distribution and cannot regenerate once the tissue is injured(33). This is a crucial aspect to evaluate for the OC disease progresses and eventual treatments strategies development.

1.4 The osteochondral tissue as a gradient tissue

In human joints the interface between the subchondral bone and the articular cartilage represents a critical aspect in tissues integration, because they tend to provide different physico-chemical characteristics. The stratified structure of the OC unit, defined by a selective organization of cells and extracellular matrix (ECM) composition, plays a crucial role on the structural and mechanical properties of each area. The hierarchical architecture of the unit, due to the changing in cell morphology, structure composition, mechanical and kinematical characteristics, reflects the functional roles of each zone in joint movements. This is determinant for eventual tissue degeneration process. (18) Also, the high- level complexity of this tissue makes it challenging for the development of new treatment strategies and for the design and fabrication of novel tissue engineered scaffolds.

In Figure 1.3 a representation of the hierarchical structure of the OC unit and its compartments is presented. As discussed the complexity of the structure shows an anatomical and functional separation of the unit in three compartments and furthermore the articular cartilage is spatially organized in three different zones (32). Figure 1.3 shows the existence of gradients in the whole tissue structure that are thought to be critical for joint functionality and loads transmission(9). The decreasing trend shown by collagen II level between the surface and the deep layer is offset by the opposite behaviour presented

in glycosaminoglycans and collagen X content, produced by hypertrophic chondrocytes dispersed into the calcified layer (30) (29). The water content also decreases with the depth from 84% on the surface area to 40-60% of the dry weight in the deep zone since it plays a crucial role, together with proteoglycans osmotic activity, on friction's reduction over the articular contact area and load stimuli's transduction (9).

The calcified cartilage, as intermediate layer, presents both of the main components of articular cartilage and subchondral bone: respectively Collagen Type II and hydroxyapatite. However, the amount of Collagen Type II is found to be minor than the one in the deep zone as well as the Ha content (65% of the dry weight) is reduced compared to the subchondral bone region (85% of the dry weight), reflecting the presence of graded properties also within compartments (28). The graded mechanical properties of the articular cartilage reflect its complex and stratified structure. Moreover, it was shown that compressive forces are sensitive to the ECM composition, but at the same time are responsible of the tissue stimulated GAGs' synthesis and ECM remodelling (34). The structure stiffness tends to increase along the depth of hyaline cartilage and the Young's modulus in the elastic region is estimated to vary linearly in the compartment

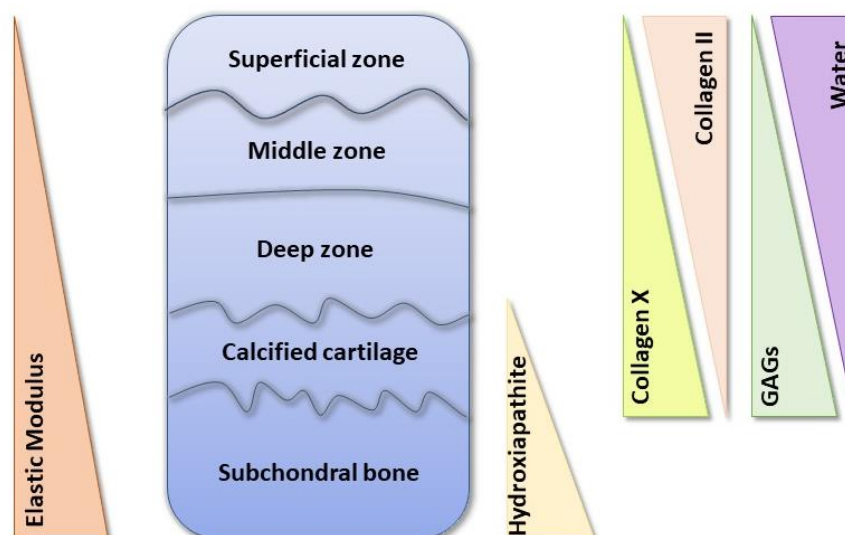


Figure 1.3 Schematic representation of OC unit anatomy which illustrates the presence of gradients on GAG, water, proteins ceramic components and compressive modulus present a concentration's gradient along the structure's length. Adapted from (34)

The calculated range lies between 1.9 MPa for the surface zone, and 15 MPa for the deep zone; whereas the subchondral bone reaches values of 4 GPa due to the hardness of its ceramic composition (28).

1.5 Osteoarthritis

1.5.1 Introduction and epidemiology

Osteoarthritis (OA) is the most common joint disorder worldwide, and it is considered one of the leading causes of pain and disability (35). Symptomatically, in United States (US), knee OA occurs in 10% of men and 13% of women aged 60 years or older (36) (37). Approximately, 27 million US adults and 8.5 million UK adults are estimated in 2013 to manifest clinical OA defined on the basis of symptoms (3). The already large clinical burden (36 million ambulatory care visits and 750,000 hospitalizations in 1997) is estimated to increase, since the disease is will affect the 20% of the population by 2030, reaching nearly 67 million people in US. This is due to the increasing of both obesity and population aging (38) (3). Among the different joints, knee and hip are the most commonly affected. This because these articulations are usually subjected to intense loads and their movements are characterised by complex articular kinematic.

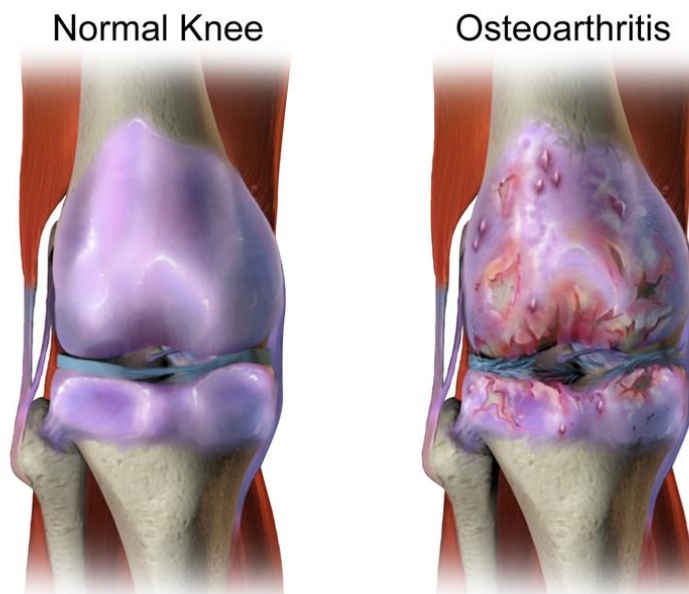


Figure 1.4 Normal knee and knee with osteoarthritis (39)

OA develops as a progressive degradation of the articular tissue due to a complex interaction between local and systemic factors. The events associated to the pathology are the loss in joint mobility, the degradation of the cartilage tissue and the chronic and persistent pain. The considered risk factors associated to this pathology can be connected to the subject, i.e. age, sex, obesity, genetics, ethnicity and diet, or to the joint itself such as injuries, malalignment or abnormal loadings of the joints (40). The hallmark symptom of OA is pain. This drives individuals to seek medical attention and contributes to functional limitations in mobility and work activity reducing the quality of life (3). Pain is a complex subjective phenomenon influenced by biological, psychological and social factors and it appears to everyone as a unique perception. Unlike many other pain conditions in which the underlying injury typically heals or resolves, OA is a disease that does not resolve but it evolves into a chronic situation that eventually leads to surgeries and joints arthroplasty.

OA can be identified as chondral and osteochondral; this last involves also the underlying subchondral plate, which is more obviously affected as the disease progresses and becomes more severe (41). Pure chondral injuries are painless, and the tissues repair activity is limited. This is due to the lack of vascularity and poor neural system in the chondral tissue. Consequently, an early identification of OA is crucial to improving clinical decision-making and advancing the understanding of disease progression and treatment options' research (42). Traditionally, OA has been diagnosed with radiographs, especially used to evaluate osteophyte formation and joint space narrowing caused by tissues degeneration. Recently, additional modalities have enhanced OA diagnosis and management through improvements in soft tissue depiction. The magnetic resonance imaging (MRI) provides high resolution, specificity and sensitivity to evaluate cartilage lesions progression. The ultrasound (US) technique allows dynamic acquisition in real time while optical coherence tomography (OCT) manages the capture of cross-sectional echographs with infrared light, acquiring near-real time images. Grading scales, such as the Kellgren-Lawrence grading scheme (43), Outerbridge classification (44) and the Osteoarthritis Research Society International (45) classification score, establish guidelines for the diagnosis of OA progression. They provide a classification in different classes (5 for Kellgren-Lawrence, 3 for the Research Society International's study) depending on injury's

severity. The main radiological feature considered as evidences of OA defect presence are essentially the same in all the studies:

- The formation of osteophytes on the joint margins or in some cases, in the joint space.
- The periarticular ossification, that involves the formation of mature lamellar bone in soft tissues.
- The narrowing of articular cartilage associated with sclerosis of subchondral bone.
- The presence of small cystic with sclerotic walls situated usually in the subchondral bone.

In Figure 1.5 the X-Ray Radiographies of a knee and a hip joint present the clinical evolution of the OC disease. According to the Research Society international classification score, the initial Grade 0 (Figure 1.5 -A,E), which represents the healthy articulation, can be compared to the others to examine the onset of the main features of the OA and the progression of the disease characteristics. Figure 1.5 B, C, D and F,G,H represent Grade 1, Grade 2 and Grade 3 respectively on the grading scale. Grade 1, as an early stage of the OA, presents the described features but moderately expressed, while at Grade 2 and 3 the symptoms are clear and evident. A progressive narrowing of the articular cartilage and a sclerosis of the subchondral bone are evident. Sclerosis appears as a region in which the tissue become denser and more radiopaque, due to the unbalanced bone turnover activity that tends to enhance tissue's production along the more sollicitated articular areas of the bone (27). The thickening of the subcondral plate is also accompanied by the formation of osteophytes at articulation margins, due again to the unphysiological load of the joint. The images show that they tend to rise in shape with the progress of the disease's severity. The comparison shows also the effect of flattening and deformation of the subchondral cortical plate referred to as bone attrition, which eventually may culminate with the direct contact of the bone counterparts, leading to pain and difficult joint mobility.



Figure 1.5 Evolution of the OC disease according to the Osteoarthritis Research Society International grading scheme(45). The X-ray radiographies of the knee and hip joints A) Grade 0 B) Grade1 C) Grade2 and D) Grade 3 show crescent severity of the disease and evidence the presence of the main clinical OA features. The Osteoarthritis and Cartilage 2007 15, A1-A56DOI: (10.1016/j.joca.2006.11.009)

1.5.2 Changes in the OC unit during the progression of OA disease

During the progression of OA disease, biomechanical and biological processes lead to alterations in terms of the composition, structure and functional properties of the OC unit (2).

One of the earliest OA changes in the cartilage is the increased water content and the swelling of the matrix, associated with the loss of the negatively charged glycosaminoglycans (46). Cartilage degradation occurs from the superficial to the deeper zone and it drives a chemical modification into the collagen matrix and its proteins' composition. The following increasing in chondrocyte anabolic and catabolic activity, and the production of reactive oxygen species lead to the appearance of surface fibrillations. The microscopic cracks in the superficial zone tend to develop, with the progress of the

disease, first into the exfoliation of fragments of cartilage and fissures and then into delamination and exposure of the underlying zones of calcified cartilage and subchondral bone(2) (47).

Genomic and proteomic analyses have identified genes encoding proteins that are differentially expressed in cartilage from patients with OA in comparison with healthy cartilage, showing an induction of hypertrophy in chondrocytes. In this condition, occurring during oxidative stress, the expression of genes and promoter regions (such as HIF2 α MMP13 or COL10A1) that encourage cartilage damage are enhanced (48).

The development of the disease is characterized by the penetration of the calcified cartilage by vascular elements and sensory and sympathetic nerves at sites of microcracks and fissures created in the OA junction. The result is the expansion and the advancement of the calcified cartilage into the overlying hyaline articular cartilage and the tidemark duplication (49).

During the evolution of OA also the subchondral bone undergoes marked changes in its composition and structural organization, including the increase of the cortical plate thickness and the alteration in subchondral trabecular bone mass and architecture. Within the subchondral bone the osteocyte canalicular network is disrupted, and osteocytes apoptosis occurs. As a result, an alteration in bone remodelling and turnover processes develops. The appearance of modifications on the mineralization state of the joint and loads distribution enhances structural damage at both microscopic and macroscopic levels. Additional changes include the development of bone cysts and bone osteophytes growth at the joint margins, resulting in the “bone attrition” process, for which the subchondral cortical plate becomes flattened and deformed (5).

Figure 1.6 shows the histologic features that occur during the development of OA disease. In the healed tissue the loss of cells and matrix is accompanied by cell cluster’s formation, the thickening of the calcified area and the vascular invasion of the cartilaginous tissue.

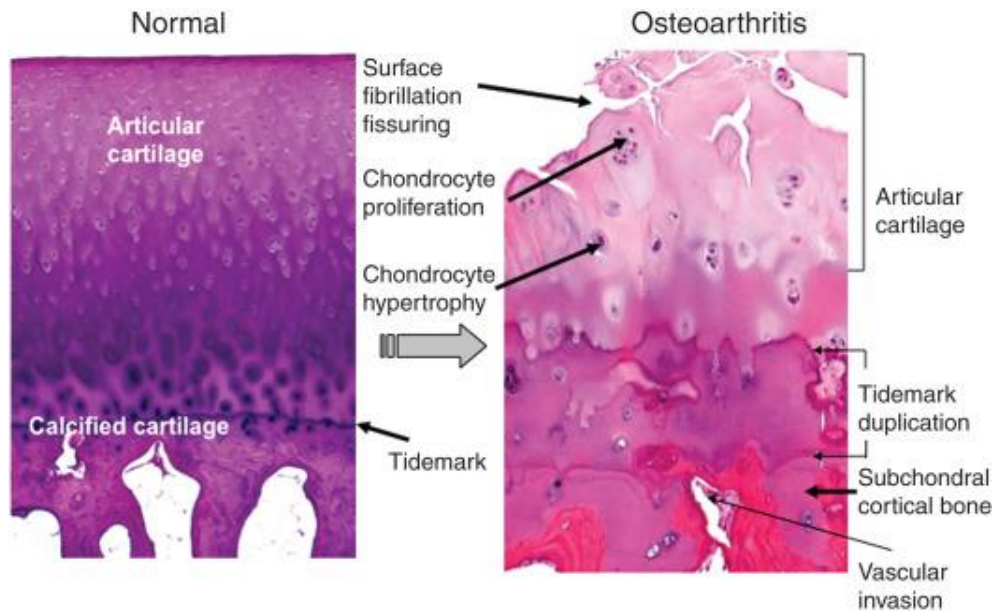


Figure 1.6 Histologic features occurring in OC unit and its components (35)

It is not clear if changes within subchondral bone precede changes in the articular cartilage and the sequence of the progression of the disease, in terms of biological, chemical and mechanical properties' adaptation, is still object of study. However, the two processes are closely related and the modification of one of them tends to induce changes in the other one, evidencing a strong biological and physical crosstalk between these tissues. Bones have the capacity to rapidly alter their architecture and structural properties *via* the cell-mediated processes of modelling and remodelling. In contrast, although recent studies have shown that chondrocytes can also modulate their functional state in response to loading, the capacity of these cells to repair and modify their surrounding extracellular matrix is relatively limited in comparison to skeletal tissues.

Furthermore, several studies have provided insights into the interactions between bone cells and chondrocytes, and the contribution of these interactions to OA joint pathology. It was found that chondrocytes viability tended to be enhanced in co-culture with bone-like cells compared to the single culture. Co-culture also modulated gene expression patterns in the osteoblasts, with upregulation of MMP13 (Matrix metalloproteinase 13), COL2A1 (Collagen Type I alpha 1 chain), OPN (gene that encodes Osteopontin) and ALPL (gene that provides instruction for producing an enzyme called Alkaline phosphatase) (50). In another study, it was demonstrated that co-culture of chondrocytes with sclerotic osteoblasts,

derived from the sclerotic bone of patients with OA, showed reduced expression of ACAN (which encodes aggrecan), COL2A1 (which encodes collagen type II) and SOX9 (gene that provides information for producing proteins critical for the embryonic development), and increased expression of metalloproteases MMP3 and MMP13, responsible for the oxidative stress induction during the OA pathology (50) (51). This evidences that subchondral bone cells induce phenotypic changes in human osteoarthritic chondrocytes.

Finally, considering the existence of an intense biological and physical crosstalk between articular cartilage and subchondral bone, OA must be addressed as a multifactorial and complex disease that affects the whole joint and its OC components (5).

1.5.3 OA traditional treatment strategies

As presented, OC defects are subdivided according to their depth and width. Consequently, the clinical treatment must be largely consistent with the classification of the injury and the patient's demand (32). The heterogeneity of human OA population and the lack of widely accepted sensitive and specific tools for assessing OC pathology represent challenges to the development of new therapies and recovery strategies(2). Both non-operative and operative techniques have been employed in the treatment of OC unit diseases according to the primary necessity, in order to restore movements and to reduce the pain in joint's site. The non-operative techniques include the systematic use of no opioid analgesics, such as analgesics acetaminophen or nonsteroidal anti-inflammatory drug (NSAID), or opioid therapies as a relief of the pain (52). Recently, numerous clinical studies have found favourable effects by the administration of glucosamine and chondroitin sulphate. These compounds, once absorbed from the gastrointestinal system, seem to enhance proteoglycan synthesis in articular cartilage reducing the development of the tissue degradation during OA (53).

However, since these strategies tend to provide temporary relief, but they do not reduce the disease's progression, some operative techniques have been necessary to ensure advanced cartilage repair and joints' functionality replacement. Essentially, these are surgical procedures, such as : debridement, bone marrow stimulation techniques, OC transplantation techniques, chondrocyte implantation and joint arthroplasty (54). Briefly, Debridement and Arthroscopic Lavage represents a primary treatment for small injuries

with diameter smaller than 2cm. This approach consists of the elimination of fragments of damaged cartilage within the joint. In theory, arthroscopy for OA should relieve symptoms by removing debris and inflammatory cytokines from the joint site but there is a lack of evidence about the effective benefit of the solution (6). The execution of this procedure could be a helpful strategy to reduce pain in selected patients, but it is not considered a definitive solution since it does not prevent the development of the OA disease. This technique is generally reserved for lower demand older patients with limited symptoms who would have difficulty with restricted post-operative mobility (41).

Bone marrow stimulation techniques (BMS) is generally used to heal defects smaller than 10 mm deep and consists of the subchondral lamina's penetration to promote cartilage tissue repair. Indeed, BMS has the intent to stimulate the migration of mesenchymal pluripotent stem cells from the bone marrow, by applying drilling microfracture or abrasions on the subchondral bone surface. The blood, produced from the microfracture, rapidly fills the OA defect space and organizes into a fibrous clot. Blood cells and platelets, together with undifferentiated cells trapped into the defect, start secreting fibrocartilage, which is made of collagen I, producing a progressive hyalinization and chondrification. However, this treatment allows to fill and repair the OC damage but lacks the histological and mechanical properties of the articular native cartilage (55). In Figure 1.7 the surgical procedure is illustrated (56). After removing the damaged cartilaginous tissue, microfractures with 0,5-1 mm of diameter and 3-4 mm of separation are generated on the subchondral plate, producing the formation of the fibrous mesenchymal clot.

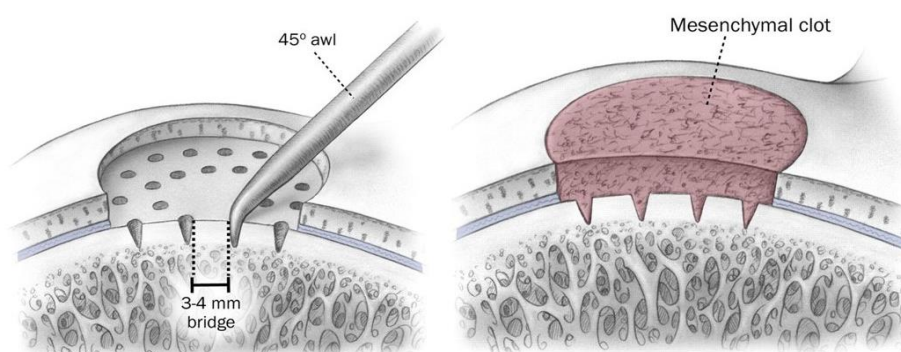


Figure 1.7 Microfractures technique and the formation of the fibrous mesenchymal clot (55)

Osteochondral Transplantation Techniques involve the transplantation of OC autologous or allogenic grafts. The mosaicplasty or osteochondral autologous transfer system (OATS) exploits the implant onto the defect site of autologous cartilage tissue extracted from a non-weight bearing region of the joint, usually the tissue of the peripheries of the femoral condyles at the level of the patella femoral joint is used (6). OATS is generally chosen as a strategy for small to medium chondral and osteochondral defects (2-3 cm of diameter) while larger defects are preferentially treated by using allograft tissue (32). The Autologous Chondrocyte Implantation (ACI) technique involves the re-implantation of autologous cells taken from the underneath periosteal flap tissue, cultivated and proliferated. Chondrocytes are harvested from the site during arthroplasty surgery and expanded during 3-4 weeks in monolayer culture. The re-implantation of the cells is performed by injecting them underneath a sutured collagen membrane (6). The disadvantages of this technique are the two-stage procedure and the costs associated with the cell manipulation. A variation of the procedure is the Matrix Autologous Chondrocyte Implantation (MACI), which provides the culture of cells on a porous biocompatible scaffold that is afterwards implanted into the cartilaginous defect to enhance the structural properties of the graft (19). The use of a 3D structured scaffold provides a template that facilitates chondrocyte adhesion, expansion whilst maintaining a chondrocytic phenotype limiting dedifferentiation, which has been observed in two-dimensional systems. (57). Dedifferentiation is a reverse epigenetic reprogramming resulting in the loss of phenotypic specialization and progression of cells to a less differentiative state. In fact, the differentiated phenotype of articular chondrocytes is characterized by the production of type II collagen and cartilage-specific proteoglycan. It was shown in a recent study that their culture in serial monolayer tends to cause a modification in their phenotypes enhancing the synthesis predominately of type I collagen and a low level of proteoglycan leading cells toward a less differentiated state. At the same time, suspension culture of chondrocytes in 3D agarose scaffolds allowed the re-expression of differentiated phenotypes (57) (32).

With arthroplasty is intended a surgical procedure that concerns the replacement, remodelling or realignment of the articular surface of a musculoskeletal joint. Osteotomies are performed since the nineteenth century to unload the damaged compartment and to transfer the weight load from the affected areas. This procedure has the intent to reduce pain, slow the degenerative process, and delay joint replacement in OA diseases (6). With

the development of orthopaedic surgery and biomaterial studies, joint replacement has become a well-accepted, cost effective and safer strategy for the treatment of severe OA disease (58). In joint replacement therapies, the damaged OC tissue is partially or totally removed and resurfaced. An artificial implant, consisting of a metal shell (such as titanium, stainless steel, or alloys), a polymer piece (such as polyethylene in order to glide smoothly), and a metal stem, is implanted to replace the damaged joint (10). However, the irreversibility of the procedure makes it recommended only in patients for whom other treatment modalities have failed or are contraindicated. Durability of prosthetic components depends on the joint and the state of solicitation and is generally about 15–20 years. Therefore, arthroplasties should be avoided, whenever possible, particularly in young subjects. This has led to a shift of the research focus towards more innovative and functional strategies for the treatment of OA (32).

1.6 Properties and functions of OC unit

The natural joint is a complex composite structure with changing properties compositions and anisotropy at different locations. The main properties and functionality of the system that must be considered for the analysis of the tissue's replacement strategies are: (59)

The distribution of high static and cyclic dynamic loads (they can reach a value almost 10 time higher than the body weight of the subject depending on the joint)

The protective function of the cancellous bone from high and intermittent stress.

The achievement of a solid and long-lasting fixation obtained by the integration of the material into the native tissues.

The constant lubrication of the contact surfaces with a fluid film.

The improved wear properties of bearing surfaces.

The low coefficient of friction to allow the movement of the bone counterparts into the articular cavity.

The reduction of the nominal contact pressure over the contact surfaces.

The guarantee of joint's conformity and the preservation of the articular movement's kinematic.

Chapter 2: State of the art in OC tissue engineering

2.1 OC Tissue Engineering

Tissue Engineering (TE) is a relative new research field aiming to find innovative solutions for the development of functional tissue-like 3D substitutes. Combining the biology and engineering principles, this science leads the human body's natural reaction to trauma and injuries to generate a cascade of biochemical processes to enhance tissue repair and regeneration (60). TE mainly utilizes cells, biomaterials, biochemical (e.g. growth factors) and physical signals (e.g. mechanical loadings) or their combination, to generate tissue-like structures (61).

The interaction between the three TE main pillars (Figure 2.1), biomaterials for scaffold's production, cells as active regenerative elements and signals for modulation of tissue response, seems to be a central focused point for the achievement of a functional structure with high-specific regenerative functions. Even if TE applications may lack one of these pillars, their combination is essential for the success of the strategy and this explains the recent effort on the development of new studies on all the elements of the triad (61).

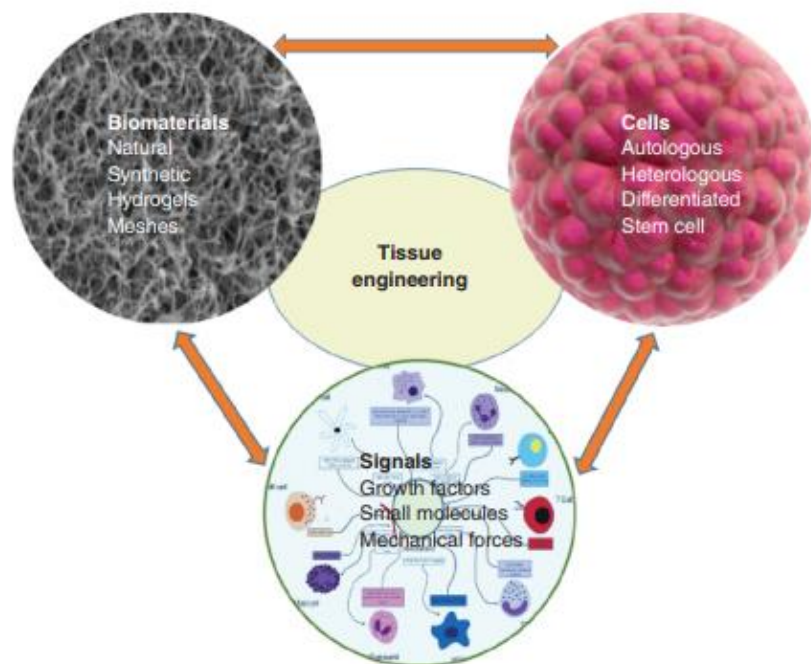


Figure 2.1 Schematic representation of the triad of TE. The combination of cells, scaffolds and signals is crucial to assemble biomimetic tissue-engineered constructs for replacing damaged tissues in humans (61)

Several approaches have been achieved for the generation of the tissue-like structure. The most common one is the fabrication of a pre-made porous scaffold (synthetic or natural) by the use of a fabrication technologies process such as fiber based techniques (FBTE), such as Electrospinning or Microfluidic spinning, or solid free- form (SFF) technologies, such as AM or 3DP (62) (63). The production can be followed by the loading of the structure with cells seeded on the top or into the scaffold's cavities, while in other methods, cells' introduction is generated by encapsulation into natural or synthetic hydrogels, directly during scaffold's production (64). Recently have been developed new approaches that involve scaffolds' generation from decellularized ECM, using either xenogeneic or allogenic tissue. This approach provides the closest natural biochemical and mechanical properties needed in the implant site, but is limited by the supply of autologous grafts and the immune-response of the non-autologous tissues (61).

The evolution of TE, occurred during the past decade, is strictly associated to the development of multiple and interconnected fields such as chemistry, biomaterials' engineering, growth factors delivery process's improvement, advances in understanding biophysical cues on cellular behaviour, study of scaffolds' architecture and manufacturing process(65). Advances in bio-fabrication technologies, including programmed self-assembly and three-dimensional printing, has allowed the production of complex porous scaffold architectures with integrated vasculature and multiple cell or extracellular matrix (ECM) types at high spatial resolution (65).

Therefore, TE offers a valid alternative to the invasive and non-conservative option of joint arthroplasty or the palliative effect and lack of biomimetic activity of the current OC defects' surgical treatments described in Chapter 2 (66). In fact, it allows the possibility of a sustainable and effective solution, when the damaged OC tissue is replaced with a long-lasting bio-manufactured replacement tissue (11).

2.2 OC tissue-like scaffold requirement

In TE, scaffold plays a key role in providing a 3D environment to support cell growth, matrix deposition, and tissue regeneration. OC tissue is anchorage-dependent and characterized by ECM with specific layered functions and composition (Chapter1)(2). Considering the

heterogeneity in composition, mechanical properties and biochemistry of the articular cartilage and the subchondral bone, the research has focused on engineered and manufactured structure independently for both the compartments of the OC unit. Bone and cartilage are classified typically as hard and soft tissue respectively and they require different and specific strategies for tissues' repairing (9). There are several characteristics that a tissue engineered scaffold for OC tissue regeneration should satisfy:

- Biocompatibility to minimize local tissue response and maximize cell growth and tissue integration;
- Biodegradability with a favourable resorption rate, which has the intent to provide structural support for the initial cell growth and then gradually leaving space for new tissue formation;
- Porosity and interconnectivity to promote cell migration, exchange of nutrients and wastes during remodelling (67);
- Selected mechanical properties to favourite tissue growth under native mechanical loads reproducing native tissue's rigidity and stiffness(10);
- Provide support for both chondrocytes and bone-like cells to attach, grow, migrate and differentiate in vitro and in vivo.
- Interact with cells actively to enhance their proliferation and differentiation

The important roles played by scaffolds in TE are analogues to the ECM functions in native OC tissue and are associated to their architectural, biological and mechanical features in order to create a bioactive template able to elicit specific and predictable cells and tissue response(68) (64). Currently, most of the natural and synthetic scaffolds are homogeneous in composition for simple cartilage defect repair, which is considered the tissue that needs a better guide to repair, since its structure does not provide any regenerative activity. The mono- phasic scaffolds evolved in materials and design from a bulk cubic structure (i.e PLA scaffolds produced in 1995 (69) for cartilage repair) to a porous and more complex architecture such as the achieved porous design made of biodegradable poly(ethylene glycol)-terephthalate/ poly(butylene terephthalate) (PEGT/PBT) co-polymers in 2005 (69) (70). Monophasic scaffolds were found to provide a good support in terms of cell attachment and proliferation, but they lack the inherent physical structure necessaire for simultaneously repair the two compartments of the OC unit (66).

Therefore, the innovation of the biphasic, multi-phasic and graded structured scaffolds represents a suitable solution required to meet this demand. Different studies have been published on both acellular and/or biological scaffolds. This second approach seems to produce better results in terms of hyalinisation and new cartilaginous tissue formation comparing to the cell free implant method (71). In Figure 2.2 examples of monophasic, biphasic and graded scaffolds for OC tissue repair are presented.

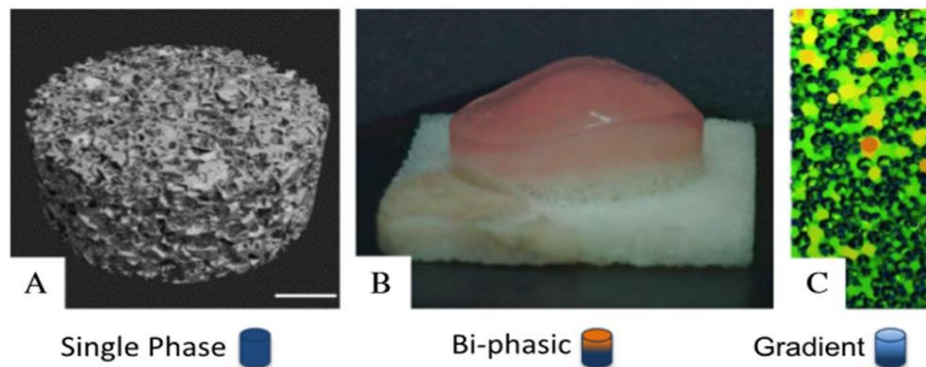


Figure 2.2 (66) Biodegradable scaffolds for tissue engineering including (A) electron micrograph reconstruction of PEGT/PBT single phase scaffold fabricated through compression moulding (72); (B) anatomically shaped agarose/bone bi-phasic scaffold (70), and (C) MicroCT of PLGA gradient scaffold (73).

2.2.1. Development of biphasic and multiphasic scaffolds

Biphasic scaffolds are made of with two parts: the cartilage segment and the subchondral moiety and this functional separation allows structure's characterization with different mechanical strengths and spatial structures of different parts. Additionally, the layered design allows different loading abilities of growth factors supporting separately chondrogenesis for cartilage regeneration in the upper layer, and the osteogenesis in the repair of subchondral bone in the underlying layer (74). Different materials and manufacturing processes have been explored for the achievement of bioinspired biphasic scaffolds, in order to mimic complexities and natural structures of OC tissue. Usually, cartilaginous layer is composed of lower strength hydrogels while the underlying subchondral layer is made of higher strength materials, such as, tricalcium phosphate and bioceramic materials. An increasing number of bi-layered scaffold have been assessed in vitro and preclinically determined toward in vitro in vivo osteochondral defects animal models and some of them are presented in Table 1 (74). Some of the strategies involve the

implant of bare acellular scaffolds, some others are seeded with chondrocytes bone-like cells or MSC cells and encapsulated biotic factors, such as growth factor for OC regeneration. The manufacturing of this type of scaffold is achieved by independent and different production processes by which two different scaffolds are produced and eventually combined to form the complete structure. This route provides the advantage of the possible simultaneous seeding of different type of cells on the two separate parts, but it presents the problem of the careful follow-up of the interface surface's stability. In fact, the presence of two separate parts into the scaffold's structure may lead to the *in vivo* separation of the two layers, due to the inappropriate resistance to the physiological shear and mechanical stresses, causing poor osteochondral reconstruction (75) (66). Moreover, this strategy involves the necessity and the optimization of two different fabrication's method, making the production itself time and cost consuming (11).

In order to better mimic the complexity of the native tissue structure and to provide a more functional biomimetic template, the interest in OC regeneration is dramatically developing in the investigation of new fabrication strategies and biomaterials' solutions for the achievement of tri-phasic and multiphasic scaffolds. The major focus of the multi-phasic scaffolds is the interface between the subchondral bone and the articular cartilage, introducing a layer on the scaffold that would mimic the calcified cartilage found in the native OC tissue. However to date, the design and formation of a stable interface between cartilage and subchondral bone in a multiphasic scaffold still remain challenging in OC tissue engineering (76). Many strategies have been explored with the combination of conventional and unconventional methods for the achievement of bio-inspired scaffolds. The intermediate layer is generally introduced to provide gradually changing characteristics from the two different compartments. The gradual transition may be produced by the layer's composition, using for example a combination of the materials of the adjoining layers; or structural, generated by the design itself of the structure, obtained directly during the manufacturing process (77) (78). The scaffolds' fabrication may be achieved by sequential steps of a unique technique or by using different manufacturing processes for the different layers such as FDM, freeze- drying, freeze-thawing or sintering (79) (11). Many studies achieved good results in terms of porosity and stiffness of the structure and graded mechanical properties, better reproducing the native load conditions comparing to

the monophasic scaffolds' results (77). Furthermore, progresses have been reached on the layer specific tissue regeneration induced by both the design of the scaffolds and the introduction of specific growth factors for chondrocytes and osteoblasts(80). In fact, it was demonstrated that the differentiation of BMCs cells into distinct phenotypes can be modulated not only by the specific material composition but also by zonally-organized 3D tissue (34) (81).

Since the complex structure of the OC unit also involves the presence of composition and mechanical gradient within the compartments (in particular water and proteins for the cartilaginous layer, and mineral and organic constituents in bone counterpart) recent approaches are directed towards the production of inhomogeneous and anisotropic structure, enabling the possibility to reproduce the complex spatial tissue's gradient. (34) (31) (82). The second part of Table 1 reports also some example of multiphasic and graded scaffolds. In Figure 2.3 two different innovative manufacturing processes of biomimetic multilayer (a) and graded (b) scaffolds for OC tissue repair and regeneration are presented.

Table 2.1 Summary of the recent bi-phasic and multiphasic scaffolds for OC tissue repair and regeneration

	SCAFFOLD DESCRIPTION	MANUFACTURING PROCESS	MECHANICAL CHARACTERIZATION	IN VITRO AND/OR IN VIVO ANALYSIS	REF.
Bi-phasic	Top: PLCL Bottom: PLGA/ β -TCP BMSCs cells seeded	T: sintering B: gel pressing	Good compressive resistance	Well organized cartilaginous tissue formation Presence of calcium-phosphate in bone layer	(83)
	Top: silk fibroin Bottom: silk/nano CaP Acellular	Salt leaching + freeze drying	/	Good tissue integration with a layer of connective tissue adhered on the entire surface Enhanced bone tissue formation	(15)
	Top: collagen type I Bottom: col I/MgHa	T: aqueous solution and precipitation B: co-precipitation	Good mechanical properties	Enhanced chondrocytes proliferation and differentiation Osteo and chondrogenesis promotion	(84)
	Top: alginate/hyaluronic acid Bottom: alginate/Ha	Directed ionotropic gelation	/	Good biocompatibility ECM deposition in in vivo models Slow bone tissue formation	(85)
	Top: PVA/gel/V Bottom: n-Ha/Pa-6 MSC culture	Freezing-thawing	/	New cartilage-like tissue formation Chondrogenic and osteogenic differentiation of MSC cells	(80)
Multi-phasic scaffolds	Top: ColI /HYA Middle: ColI/Ha (40/70%w/w) Bottom: ColII Ha (30/70% w/w)	Suspension and precipitation	Graded mechanical properties	Selective cell differentiation	(86)
	Top: Col I/ Col II/ HYA Middle: Col I/HYA Bottom: Col I/HA Acellular	Freeze-drying	/	In vivo equine model: Tidemark restoration Formation of well-structured subchondral bone and articular cartilage Biocompatibility	(87)
	Top: Chitosan/gelatin hydrogel loaded with TGF- β 1 Middle: conically graded Chi/gel/PLGA Bottom: PLGA loaded with BMP-2 MSCs culture	T: UV polymerization B: separation/leaching	Good connection between phases Graded mechanical properties	In vivo rabbit model TGF- β 1 promotes MSC proliferation and differentiation and hyaline cartilage regeneration BMP-2 stimulates chondrogenesis and osteogenesis	(88)

	Top: alginate with superficial chondrocytes Middle: alginate with middle-deep chondrocytes Bottom: PCL with osteoblasts	T: ionic crosslinked alginate wit CaCl ₂ B: FDM	Good integration of the layers	In vivo mice model Limited mineralization of the PCL part Limited blood vessel network formation	(12)
	Top: Col I /HYA Middle: lyophilization of the two layers Bottom: Coll/ HA	Freeze/lyophilization	Increased stiffness with scaffold depth	In vitro study Chondrogenesis and osteogenesis of MSC cells	(78)
Graded scaffold	Scaffold: PLGA microsphere Porogen: NaCl BMSCs culture	thermal sintering and porogen leaching	Graded structure porous	In vitro study Support both chondrogenesis and osteogenesis	(73)

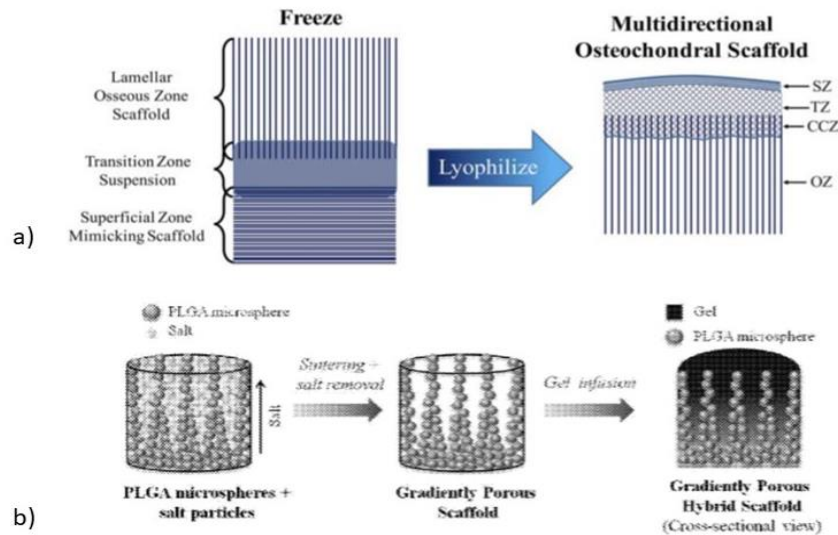


Figure 2.3 representation of two different innovative manufacturing processes of: (a) biomimetic multilayer and (b) graded scaffolds for OC tissue repair and regeneration (78) (73)

2.3. Materials and fabrication Techniques for OC- multi-layered scaffolds

Two are the main type of polymeric materials mainly chosen for OC tissue engineering: synthetic and natural. The most widely used synthetic polymers are poly (L-lactic acid) (PLLA), poly (glycolic acid) (PGA), and polycaprolactone (PCL). They provide great flexibility allowing facilitating synthesis, processing, and modification, but on the other hand these polymers lack bioactivity and specific tissue reconstructive functions (89). A recent study, for instance, proposes a bilayered scaffold fabricated by combining a sintering method and a gel pressing method with poly(lactide-co-glycolide), beta-tricalcium phosphate, and poly(lactide-co-caprolactone). The composite PLGA/ β -TCP part provides osteoconductive activity for bone regeneration while the elasticity of the PLCL can reproduce the mechano-active properties for cartilage regeneration. (83) Natural polymers are also widely used for OC tissue reconstruing for their intrinsic biomimetic properties due to peptide sequences on their chains that affect cell adhesion, proliferation, and differentiation resembling the ECM matrix proteins (90). Collagen, gelatin, silk, and chitosan are the most used as natural polymers for scaffold fabrication, but they need precautions to prevent their physiological denaturation. A bilayer biomimetic scaffold made of an organic compound (type I collagen), and magnesium-doped Hydroxyapatite, to reproduce respectively the cartilaginous and

bone part, was fabricated and the *in vitro* and *in vivo* tests proved the increased activity in cells attachment, proliferation and differentiation in this environment(14).

Furthermore, since both synthetic and natural polymers have advantages and disadvantages, research has progressed to fabricate hybrid materials to maximize the benefits of both. For instance, in a recent study PCL combined with various amounts of chitosan was fabricated to create bioactive nanofibers for the stimulation of osteogenic differentiation (91) (92).

Bones and cartilage appear to be complex material made of organic and inorganic matrix in which cells are dispersed, showing the reproduction of structures at both macroscopic and microscopic levels. Furthermore, a crescent development of nanotechnology strategies in TE and biocomposite materials is due to the proved ability of nanostructured scaffolds to provide a closer structural support approximation to native osteochondral architecture for cells and regulate cell proliferation, differentiation, and migration, which results in tissue's reconstruction (90) (93). The technologies used for the fabrication of porous scaffolds for tissue engineering are both conventional (such as gas Foaming, freeze-drying, emulsification, freeze-drying phase separation and spinning methods) that allow to obtain biodegradable, biocompatible and biomimetic structures with less control over their internal architecture, and unconventional (such as stereolithography, selective laser sintering, fused deposition modelling and 3D-Printing) that including rapid prototyping techniques, provide the achievement of highly interconnected porous and reproducible structures. Electrospinning is a widely used conventional technique in TE because enable the production of porous scaffolds by material's nanofibers deposition, providing a good biomimetic structure for the growing tissues (loh) e chong Between the non-conventional techniques 3D printing has developed good successes in the recent researches and it is considered a good source for the reach of functional strategies in OC TE.

2.3.1 Nanocomposite biomaterials

Nano biomaterials and nanocomposites represent promising field in OC tissue engineering, due to their capacity to resemble the natural ECM organization providing functional bone tissues stimuli and micro and nano scale osteo-mimetic architecture. Since natural OC tissue features are nanometric in dimension, recent researches and studies, showed that the presence of nanometric structures and nanomaterials play a key role in stimulating cells

growth as well as guiding tissue regeneration(10) (93). Moreover, they tend to influence properties such as the wettability the roughness and the surface contact area of the scaffolds promoting biomaterial-driven bone regeneration through increased protein adsorption, nutrient exchange, and porosity relative to macroscale biomaterials (90).

Hydroxyapatite ($\text{Ca}_5(\text{PO}_4)_3(\text{OH})$) and calcium phosphates represents a widely studied class of materials for healing in bone. Ha can be synthesized and easily reduced in powder, but it is characterized of a limited brittleness and poor degradability. Since natural bone mainly consists of collagen fibers and apatite crystals (85% of the dry weight), the inorganic–organic composite materials have a great application prospect in bone tissue engineering joining the osteoconductivity to a good mechanical stability of the structure(94). Currently, many studies in TE show the use of Ha in combination with synthetic polymers in order to enhance the bioactivity and scaffolds' integration into native tissues (95) (94) (96). Some recent studies also showed that the presence of the Hydroxyapatite has also benefits on cartilage reconstruction, making this material extremely interesting for the treatment of OC disease and OC tissue repair(97). Moreover it is shown that the presence of the ceramic phase into a polymeric matrix tends to increase the viscoelastic and mechanical properties of the template(96). According to the data provided by the literature, both Ca^{2+} cations and anions - orthophosphates (PO_4^{3-}) and hydroxyl (OH^-) - can be substituted in Ha lattice to optimize physicochemical and mechanical properties and impart additional biological properties(98). In particular, Strontium ion, as Ca substituted, has been clinically tested to have a favourable effect on bone tissue. In vitro and in vivo studies demonstrate that Sr increases the viability and activity of osteoblast, whereas it inhibits osteoclastogenesis and osteoclast differentiation(99). The precise molecular targets of Sr in bone cells are still being investigated. As a divalent cation similar in structure to Ca^{2+} , Sr^{2+} may act on similar cellular targets, being recognized by calcium-sensing receptor (CaSR) and activating Ca^{2+} -sensitive pathways (100). There have been many articles in which Ha enriched with strontium ion was used to fabricate a scaffold for bone and OC tissue regeneration (101) (94) (102) (103).

2.3.2 Additive manufacturing processes and 3D bioprinting

Additive manufacturing processes take the information from a computer-aided design (CAD) file that is later converted to a stereolithography (STL) file (104). In this process, the drawing made in the CAD software is approximated by geometrical shapes and sliced, containing the information of each layer that is going to be printed. The realization of the final product develops from the optimization of the design parameters, achieved when the actual final prototype design shows the perfect match with the desired characteristics. The steps required for the production development of functional structures using rapid prototyping in AM are summarized in Figure 2.4.

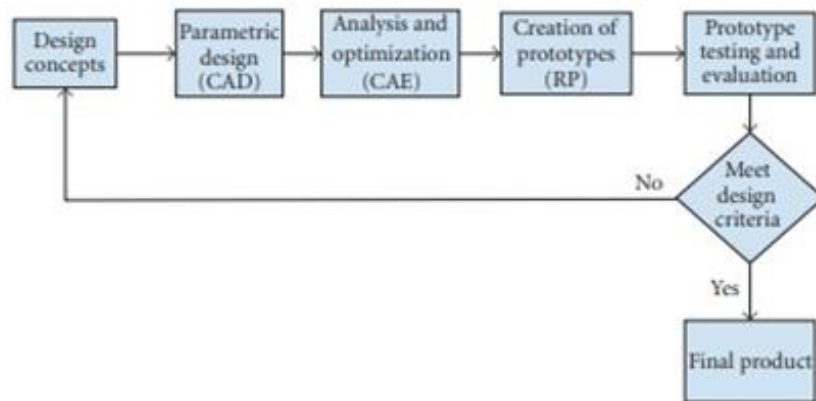


Figure 2.4 Product development cycle (105)

The classification of these processes involves the split based on the type of material's phase used during the processing. The liquid-and powder-based processes such as FDM, stereolithography and 3DP seem more promising than solid-based processes of which LOM is the predominant one today(62). Three-dimensional printing involves the laying down of successive layers of material to form 3D models, thus enabling better control of pore sizes, pore morphology, and porosity of matrix as compared with other fabrication methods. In general, the binder solution is added onto the syringe from an "inkjet" print head. The structure is printed layer by layer by subsequent deposition of the material repeatedly above the previous layer allowing to obtain complex 3D shapes with high resolution and controlled internal structures. There are two types of pores fabricated by this process, that is, pore by design and pore by process. However, only a limited number of polymers can be fabricated using this method given the high temperatures involved in this method (62).

3D printing represents a technology with large potential, providing low cost simple and rapid prototyping of complex structures and production layer by layer without the need to assemble different parts to form the tissue replacement (106). Recent progresses in TE in Image-based design (IBD) solid free-form (SFF) fabrication and additive manufacturing processes have been optimized to achieve load bearing scaffolds with biomimetic architecture matching the articular geometry (75) (107). These techniques, enabling a precise control over scaffold design, inner pattern and porosity may be functional to produce scaffolds with mechanical and biological properties that provide immediate load bearing while promoting tissue ingrowth. In addition, biological chemical and physical stimuli aging on the composition of the bioink might be added (108). The achievement of physical and chemical graded structure or the encapsulation of growth factor and organic biomimetic component into the matrix play a key role in bioactive properties and scaffold's integration into native tissues. Furthermore, they allow to fabricate physically graded, biphasic and multiphasic structures using a single manufacturing process solving the problem of the assembly of the different parts separately produced with other TE strategies (82). This allows to better control the interface bone-cartilage stability but also the triggering of simultaneous bone and cartilaginous cells culture rather than depending on the assembly of separate living structures (75).

Three-dimensional (3D) bioprinting biphasic scaffolds have been first reported in 2002 (109). In this study it was developed a new, heterogeneous, and osteochondral scaffold using the TheriForm™ three-dimensional printing process for osteochondral regeneration. The upper cartilage region was composed of poly d,l-PLGA/l-PLA with a porosity of 90%, and the lower cloverleaf-shaped bone portion was 55% porous and consisted of a l-PLGA/TCP composite to enhance cell differentiation and mechanical properties. The transition region between these two sections was fabricated as a gradient of materials and porosity to prevent delamination. Synthetic polymers are widely studied as materials to produce bio-printed scaffolds (107). Particularly, PCL is a FDA approved polymer with biodegradable properties, low temperature processing, good for 3D printing procedures, and slow degradation with nontoxic degradation products (110). Printed scaffolds made of PCL and hydroxyapatite with various porous geometries have been investigated as template for OC tissue regeneration (101) (111) (110) (112).

2.3.4 Clinical Progresses and Insight

Scaffolds able to treat OC defects are currently not an available option for patients in typical medical care. Very few scaffold designs have even made it to clinical trials. Homogenous scaffolds have failed to reach prevalent clinical efficiency because bulk properties of these substitutes do not mimic properly the functions of native tissue. Bi-layer, multi-layer and hierarchical structures have been achieved more success *in vitro* and preclinical studies, compared to the monophasic ones, and represent the researchers' direction in tissue engineering approaches (11).

TruFit™ Plug (Smith & Nephew, Andover, MA) is one of the first bilayered resorbable commercial scaffold composed of semi-porous PLGA–Poly-glycolic acid (PGA) (75:25) and calcium sulphate (CaSO₄), used for OC unit defects (113). The two scaffolds, aimed to mimic the subchondral bone and the articular cartilage layer, are linked together with a small amount of solvent after individual preparations. However, the results' evaluation revealed no evidence of bone ingrowth, osteoconductive activity or ossification comparing to the actual technique used for the treatment of OA defects such as mosaicplasty or chondroplasty (11). (113) Chondrofix© (Zimmer Biomet, United States)(114) represents an innovative solution. It is composed of donated human decellularized hyaline cartilage and cancellous bone and provides relevant mechanical properties that are comparable to unprocessed osteochondral tissue. Another bi-phasic scaffold currently used in clinical trials is known as the Agili-C™ CartiHeal. The bone layer of the scaffold consists of crystalline aragonite (calcium carbonate based) and the cartilage compartment is made of hyaluronic acid. The clinical trials, achieved after the performances' optimization in goat implantation, look promising in terms of cartilage restoration (11). Finally, Maioregen™ (Fin-Ceramica Faenza SpA, Faenza, Italy), is the only actual example of tri-phasic scaffold approved in clinical usage. It is made of a superficial layer consisting of type I collagen, a lower layer that consists mostly of magnesium enriched with nanohydroxyapatite (Mg-HA) and a middle layer, composed of both Mg-HA and collagen (70/30 %w/w), that reproduce the calcified cartilage layer. The nucleation of HA nanocrystals onto self-assembled collagen fibers could be graded in concentration along the scaffold structure, mimicking the hierarchical layered structure of OC tissue and also resembling the composition of the ECM's of cartilage and bone tissues(115). The clinical trials showed interesting results. The

histological analysis suggested complete resorption of the biomaterial after 6 months and cartilage tissue appeared not only repaired but engaged in an ongoing maturation process. These clinical results obtained by the Maioregen™ highlights the advantages of having a hierarchical graded structure that mimics more closely the natural structure of the OC tissue and testifies that the use of biomaterials that resemble the ECM of native tissues tends to improve the scaffold's performances (11).

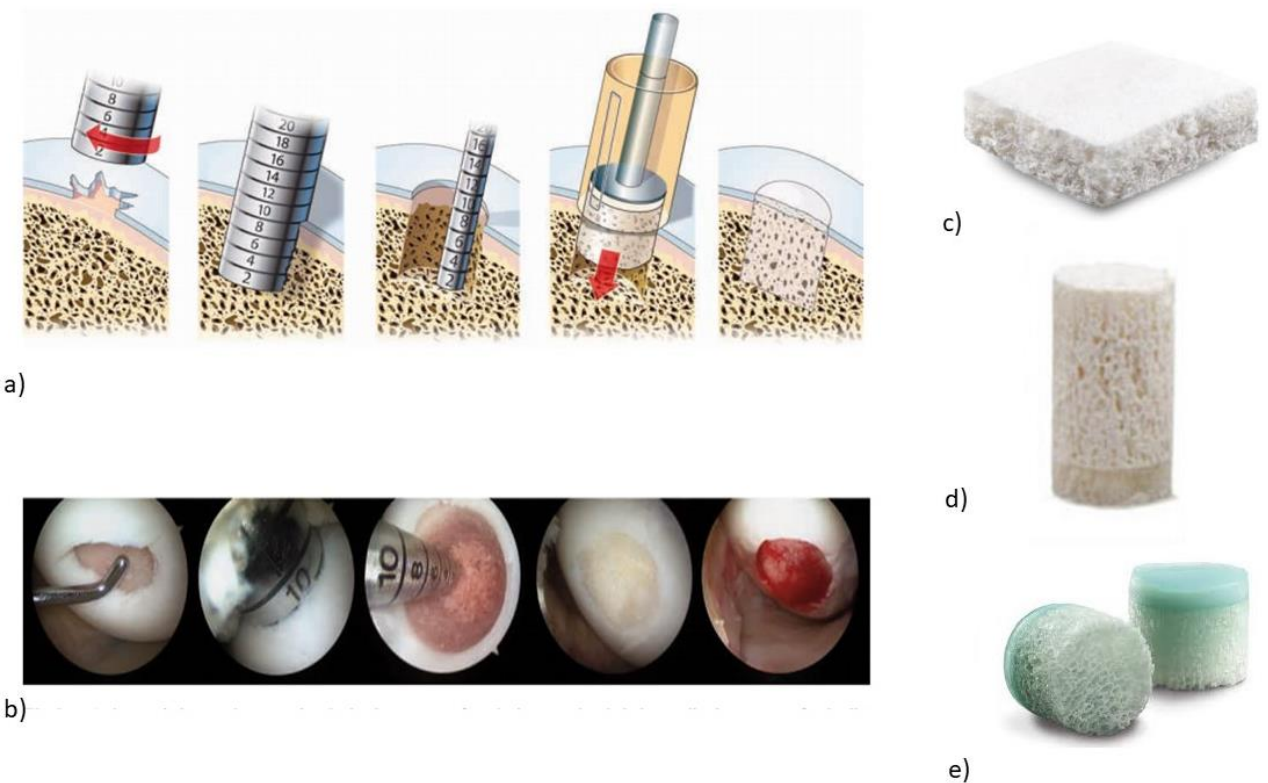


Figure 1.5 a) Surgical technique of applying cylindrical TruFit™ synthetic bioabsorbable scaffolds b) Arthroscopic images demonstrating the *in vivo* process of synthetic osteo-chondral plug application (116) c) d) e) Commercial multi-phasic scaffolds for OC tissue regeneration MaioRegen© TruFit™ Plug Chondrofix©(113,114)

2.4 Cells in OC Tissue Engineering

The production of an engineered tissue *in vitro* requires the use of cells to populate scaffolds producing ECM products resembling the native tissue's structure. Primary cells, taken from the patient and cultured directly into the scaffold before being re-implanted, allow to obtain good results in terms of implant integration (117). The main advantage of

using primary human primary osteoblast cells (HOb's) is the lack of interspecies differences and the retainment of their differentiated phenotype. However, primary human cells present heterogeneous phenotypes relating to the skeletal location from which they were isolated (20). Moreover, the harvest intervention is invasive, and the research is moving on the investigation of the use of alternative and more feasible sources of cells.

Recently, a crescent interest on the use of alternative cell sources solution have been investigated, avoiding the invasive harvesting procedure for the subject and the risk of cells' damage(117). Attention has become focused upon the use of stem cells, a source of undifferentiated cells that can divide and renew themselves over a long period. This kind of cells can develop into many different types of cells body modifying their gene expression, enabling population of multiple tissue types such including brain, blood and vessels, skeletal muscles, skin and bone. However, it requires the importance of using a terminally differentiated cell stock without latent stem cell-like properties and the need to control the differentiation into the desired tissue lineage. The bone marrow derived stem cells can differentiate to osteogenic lineage and have largely been used for bone and cartilage repair (92) (118) (119). The generation of osteoblast lineage cells from multipotent mesenchymal stem cells involves a generally accepted model of osteoblast cell differentiation. It encompasses the progression from osteoprogenitor cells to preosteoblast, osteoblasts, and then bone lining mature cells or osteocytes. *In vitro* studies in monolayer culture system have shown that the differentiation progresses through a characterised temporal sequence of expression osteoblast markers (120). Three phases of the process were identified, characterized by changes in protein and gene expression such as alkaline phosphatase(ALP), bone sialoprotein(BNP), c-fosproto-oncogen, Cfba-1 (Runx2) - core-binding factor α 1, Colla1-type I collagen followed by osteocalcin, Osteonectin, Osteopontin, Osx-Osterix typically attributed to the last differentiative osteoblast's activity(120). During a later stage of the bone formation phase, osteoblast cells can become osteocytes, transforming into inactive and mature osteoblasts. They become bone lining cells or undergo programmed cell death.(20).

Cell culture and cell lines have assumed an important role in studying physiological, pathophysiological and differentiation processes of specific cells, allowing the study of genotypic alteration in controlled environments. A cell line is a permanently established

cell culture, usually explanted directly from a living animal or human, that has the characteristic to proliferate indefinitely in appropriate fresh medium and substrates maintaining relative stable phenotypic (121). However, some studies show evidence of heterogeneous phenotypes occurring in cell lines after several cells passages and this is estimated to be due to a non-physiological proliferation of cells since the mechanism of contact inhibition is disturbed. Despite this advantage cell lines are largely used in bone TE researches and the most common are MC3T3E1 (122), Human Fetal Osteoblastic Cell Line (hFOB) (123), MG63 (124), Human osteosarcoma cell line SaOs2 (125) and U2OS (126) (20).

2.5 Cell/Scaffold interaction

When cells adhere to the scaffold's surface, a sequence of physico-chemical reactions will happen. Immediately after the implantation of the substrate into the organism's tissue, proteins absorption to its surface occurs, providing signals to mediate cell adhesion and modulating cells receptors, leading to the release of active compounds for signaling ECM matrix, cell proliferation and differentiation (127). Cells adhesion occurs from the interactions between cell-adhesion molecules (CAMs), transmembrane proteins such as integrin's, immunoglobulin (Ig) superfamily, cadherin's, and selectins. Cell/cell adhesion allows cells to communicate, modulating signal transductions and detecting and responding to changes in the surroundings (128). Cells have also specific CAMs (mainly integrins) that bind to molecules in the extracellular matrix and link the matrix to the intracellular cytoskeleton, forming a focal adhesion. Extracellular matrix acts as a support organising cells into tissues and can also be involved in cell signalling by activating intracellular pathways, when bound to the CAMs. Furthermore, cell attachment is a complex process affected by several aspects such as cell behaviour, surface's material, charge, roughness, stiffness and composition of the material itself (127).

Biomaterial development has been focusing on surface topographical analysis modifications to promote greater control over material and regulating biocompatibility. The hydrophilicity is a parameter generally related to the rate of cell spreading and differentiation. In hydrophilic substrates cells tends to show good fractal shapes and accelerated metabolic activity (129). Additionally, the incorporation of biomimetic

compound on the scaffold's surface allow to mediate the attachment and activation of neutrophils and inflammatory cells, leading to the implant's integration. For instance, soluble factors, xenobiotic factors, nutrients, oxygen and the chemical nature of the extracellular matrix (ECM) have long been recognized as essential signalling components of the local cellular niches (127). The surface charge has been also described in cell attachment phenomenon. In general it was found that the best cell adhesion appears on polar and charged surfaces that better interact with cells' transmembrane proteins (130). Material surface roughness or topography is another factor that modulates the biological tissue's response of the implant. Even if the response of cells to roughness is variable depending on the cells type and the scale of irregularities, it was proved that micro and nano-structured surfaces can generally stimulate osteoblast differentiation, showing enhanced ALP osteocalcin expression in comparison with smooth surfaces. Moreover, an increased cell spreading and proliferation in rough surfaces was reported (127) (131). Cell attachment can be also evaluated by the presence of F-actin filaments of peripheral stress fibers and filopodia departing from the cell bodies (132). In addition, nanoscale manipulation of surface features such as surface texture, geometry, spatial position, and height might potentially alter clustering of the integrins, the development of focal adhesions, and cytoskeletal structure, thus influencing the osteogenic differentiation to the surface (133).

Substrate stiffness and softness is another parameter that has been reported to influence cell attachment proliferation and differentiation. Collectively, a few common observations can be drawn from of the mechano-sensitivity of stem cells. This bioactivity is connected to of cytoskeleton contractility in response to mechanical stimuli, suggesting the importance of the force balance along the mechanical axis of the ECM–integrin–cytoskeleton linkage and their regulation by the mechanical signals in cells. Moreover, strong evidence suggested that the differentiation potentials of stem cells toward distinct lineages could be maximized if the cells were cultured in the mechanical microenvironment mimicking their tissue elasticity in vivo (134). It was also demonstrated that cells respond on both macroscopic and microscopic architecture of the tissue engineered scaffold. The scaffold shape must provide boundaries for tissue regrowth but at the same time permit cell attachment within a controllable microenvironment. The micro-macro architecture can

be achieved by changing pore size-design, interconnectivity, tortuosity to mimic the natural cells' environment matching its characteristics (135). In addition, nanoscale manipulation of surface features such as surface texture, geometry, spatial position, and height might potentially alter clustering of the integrins, the development of focal adhesions, and cytoskeletal structure, thus influencing the osteogenic differentiation to the surface (90).

In conclusions, research demonstrated the characteristic of the scaffold to direct cell behave, suggesting the potential for selective, controllable differentiation based solely on the geometry and on the presence of nanostructure on the substrates.

2.6 Challenges for the development of OC TE strategies

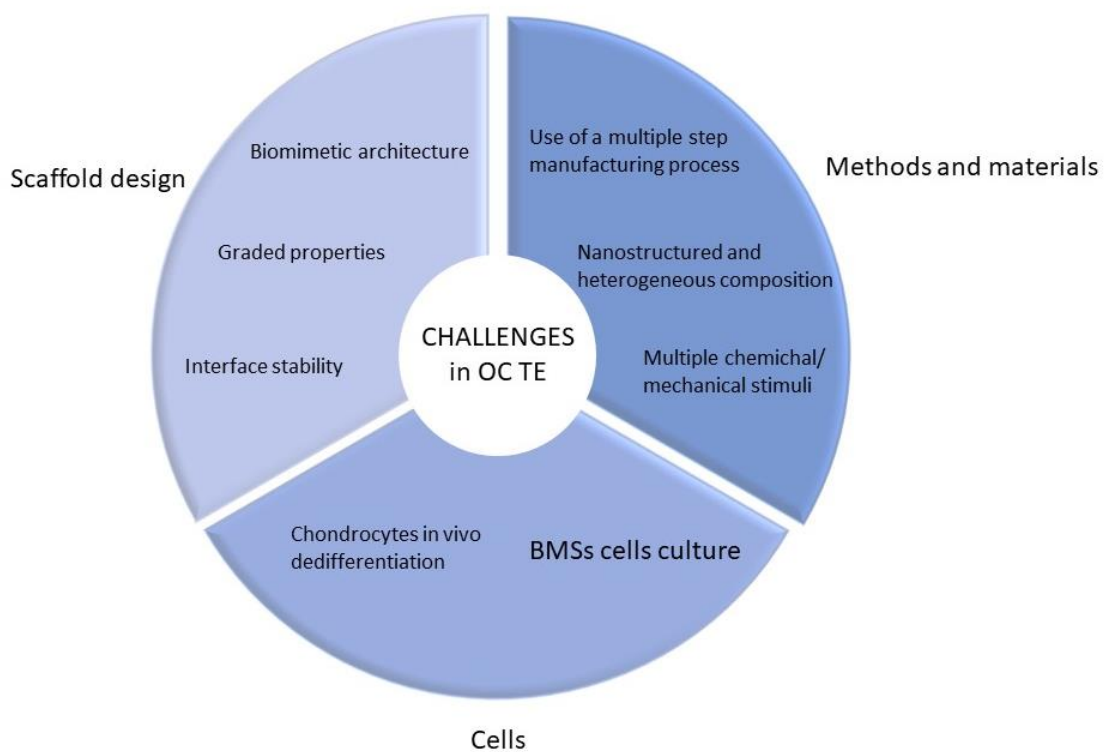


Figure 2.6 Synthesis of the main problem and current challenges in TE for repair and regeneration of the OC unit.

Osteochondral repair represents a growing topic of interest in the field of TE. The researchers' progresses obtained in the past years, led to the production of innovative and new bi-phasic and multiphasic solutions mimicking the bio-inspired design of the native tissue. Scaffolds' design and materials' composition is a steadily changing aspect in OC Tissue Engineering studied to obtain bioinspired scaffold's performances. An important aspect is the stability of the interface between subchondral bone and articular cartilage.

Besides the importance to uniformly transfer loads and solicitations between the two compartments, this intermediate layer must provide good stability and good shield stress response. In many bi-layer scaffolds, in fact, a failure of the implant caused by the physical separation of the two elements was found. However, to date, the design and formation of a stable interface in bi-layered and multi-layered scaffolds remains a significant challenge (75) (66) (11). Many studies are now showing deeper interest in graded scaffolds that, providing a gradual variation of the chemical, biological and mechanical properties could better resemble the structural interface of the native environment reflecting the complex variety of the ECM composition in both the articular cartilage and the subchondral bone (136) (66). Manufacturing processes techniques have also been widely investigated in this field because of the necessity to assemble two parts with different composition on the same scaffold. The use of a multiple-step manufacturing process makes the scaffold's fabrication time and cost consuming and necessitates of an extra step in which the two produced parts are joined together. 3D printing techniques, allowing the simultaneous printing of different materials, seems to be a good route in the latest researches for the achievement of samples with tailorable design and composition. In Figure 2.6 the main challenges in TE for OC tissue regeneration are illustrated.

Regarding the cellular scaffolds' field, an aspect of growing interest is the use of progenitor cells type despite tissue specific cells. The benefit of the use of MSCs cells in osteochondral scaffolds is related to the possible simultaneous differentiation of cells in osteogenic and chondrogenic direction(80) (66). Further studies will focus on the possibility of the BMSCs cells differentiation in chondrocytes-like cells without in vivo dedifferentiation. Another problem is caused by the BMSs cells' attitude to generate endochondral ossification. In fact, it was found that since MSC cells have the primary aim to form a fibrous clog assisting fracture bone healing, they would be inclined to not to arrest the chondrocytic phenotype but proceed to bone formation with consequent ossification of the entire structure(137).

This thesis work is addressed to overcome some of the current challenges and still open described clinical needs, providing an innovative and functional solution for OC diseases' treatments.

Chapter 3: Material and methods

3.1 Scaffold design and preparation

3.1.1 Materials

Powdered poly- ϵ -caprolactone (PCL) with a relative molecular mass of 50 kDa and a particle size $<600 \mu\text{m}$ was purchased by Polyscience Europe (Hirschberg; Germany). Sintered nano-hydroxyapatite with strontium substitution at 20% molar weight was produced and supplied by the Rudolfs Cimdins Riga (Biomaterials Innovation and Development Centre of Riga Technical University - Riga, Latvia). The PCL powder was used as purchased while the Sr-Ha powder was manually sieved with a particle size of 100 nm to eliminate bigger ceramic aggregates that would have adversely affected the printability of the composites. Two different concentrations (10% w/w and 20% w/w) of PCL/ Sr-nHa were prepared and left overnight on a mechanical shaker to allow a better uniformity of the blended powders before the use. Powders were stored into a desiccator to maintain the blend's thermo-chemical properties during the printing time.

3.1.2 Scaffold design

The scaffold design chosen for the purpose of this study is a cylindrical geometry with a height of 6 mm and 7 mm diameter. The prototype project of the cylinder was built through a CAD model using Solidworks, and the STL (Standard Triangulation Language) file was subsequently imported on a dedicated software (EnvisionTECH VisualMachine 3.0) to produce the slicing of the solid element. The entire structure was made up of fourteen layers. In particular, for the first nine layers of the scaffold based on the PCL/Sr-nHA with the highest ceramic percentage (20% w/w), the distance between two adjoining strands was 0.8 mm, and each layer was printed continuously following the geometry edge of the designed cylinder with a single extruded filament. Also, each layer was rotated of 90° respect to the longitudinal axes of previous one and shifted of half distance between the strands. The last five layers, corresponding to the cartilaginous tissue of the OC unit, were based on a lower content of Sr-nHa (10% w/w) in the PCL matrix following the same design of the first portion of the scaffold.

To best match the biomimetic function of the natural OC tissue, in order to mimic the calcified cartilage, the inner portion of the scaffold, consisting of three layers, was designed reducing the distance between the strands from 0.8 mm to 0.7 mm. The resulting crossed pattern of the scaffold was achieved by using the EnvisionTEC software dedicated. and provided by the factory as an interface with the 3D BioPlotter device. The same geometry and inner pattern described was used to produce the bare PCL scaffolds that were used as control (see summary Table 3.1).

Table 3.1 Design of the printed scaffolds

SCAFFOLD CODE	SCAFFOLD DIAMETER	SCAFFOLD HEIGHT	STRAND DIAMETER	NUMBER OF LAYERS	STRAND DISTANCE	COMPOSITION
PCL	7 mm	6 mm	0.4 mm	14	0.8 mm (layer 1 to 6)	PCL
					0.7 mm (layer 7 to 9)	
					0.8 mm (layer 10 to 14)	
PCL/Sr-nHA	7 mm	6 mm	0.4 mm	14	0.8 mm (layer 1 to 6)	PCL/Sr-nHa (20% w/w)
					0.7 mm (layer 7 to 9)	PCL/Sr-nHa (20% w/w)
					0.8 mm (layer 10 to 14)	PCL/Sr-nHa (10% w/w)

3.1.3 Scaffold fabrication

Scaffolds were produced *via* a 3D printing method using a 3D Bioplotter system (4th generation, 3D Bioplotter EnvisionTec). The equipment and its main components are illustrated in Figure 3.2. For each printing job approximately 0.8 g of powder was loaded into the steal syringe and let it to melt. Once the powder was completely melted, usually taking ~30 min, the fabrication process was started. The printing temperature and other parameters such as pressure, speed and waiting time between two different layers were selectively optimized for the three different formulations (PCL, PCL/10Sr-nHa and PCL/20Sr-nHa), and final optimal settings are reported in Table3.1. Pre-flow and post-flow represent the parameters expressed in [s] configured for each composition set to start the

materials' extrusions before or after the needle movement helping to obtain a homogeneous and continuous strand at the start and the end of its extrusion. The manufacturing process is described in Figure 3.3.

Table 3.2 Printing parameters optimized for each formulation.

	Temperature [°C]	Pressure [bar]	Speed [mm/s]	Wait time between layers [s]	Pre-Flow [s]	Post-Flow [s]
PCL	130	5.3	0.7	10	0.45	0.1
PCL/10 Sr-nHa	130	6.3	0.5	10	0.75	0.2
PCL /20Sr-nHa	140	6.5	0.4	10	0.75	0.2

Once reached the melted phase of the material, the syringe was pressurized, and the scaffolds were printed in an atmospheric controlled environment, maintained at a temperature of ~ 22 °C. A 24G stainless steel nozzle with external diameter of 700 µm and internal diameter 400 µm was used to extrude all the materials. The printing time needed for each sample was approximately 20 minutes while for the control PCL specimens the time was shortened given the use of a single material, which was approximately 16 minutes. The use of two different heads loaded with the two different compositions enabled the concurrently printing of the two layers of the scaffold one above the other by the development of a single printing project.



Figure 3.2 The EnvisionTEC 3D Bio-plotter system: (1) High temperature cartridges (2) Printing plate (3) Calibration system (4) Robot arm (5) Platform heater (138)

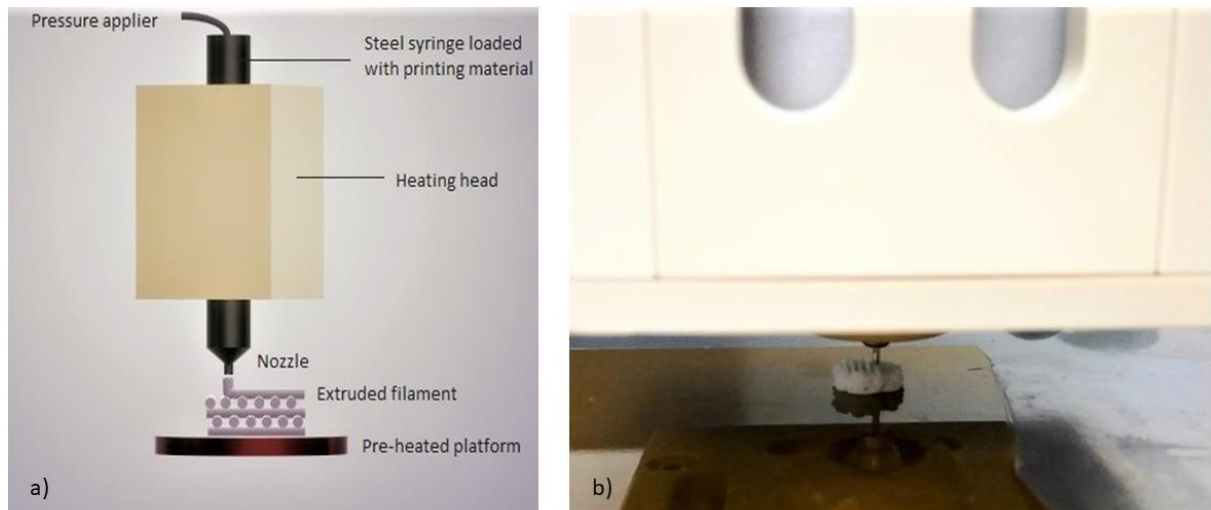


Figure 3.3 a) Scheme of the main components of the 3D Envision Tec Bioplotter and b) the actual manufacturing process

3.2 Scaffold's chemical and physical characterization techniques

Scaffolds' production was followed by the physico- chemical characterization of the samples. The investigation started with the chemical analysis of the printed filaments using FTIR and TGA technologies and proceeded with the characterization of the morphological and topographical structure of the printed surfaces using SEM scansions to investigate surfaces' roughness and contact angle analyzer to measure the wettability of the specimens.

The characterization of the geometry and morphology and the calculation of the scaffold's porosity of the entire structure was performed by μ -CT investigation. Finally, mechanical tests of compression were achieved on the scaffolds.

3.2.1 FTIR analysis

Fourier Transform Infrared (FTIR) analysis are achieved on both powders and extruded filaments to test the chemical stability of the printed material during the manufacturing process. FTIR is an analytical technique used to investigate chemical properties of the scanned tests to identify polymeric organic and inorganic materials. The FTIR test relies on infrared light to scan samples and observe bond properties to measure how well a sample

absorbs light at each wavelength (139). The beam described above is generated from a beam source containing the full spectrum of wavelengths to be measured. The light is directed through a Michelson interferometer, composed of a configuration of mirrors. One of this is moved by a motor and its position at each step allows to block some wavelength and let to pass just a little band. wavelengths are modulated at different rates, so that at each moment the beam coming out of the interferometer has a different spectrum. Computer post-processing is required to obtain the integration of the results, providing information about the rate of the total adsorption at each wavelength (140).

The FTIR instrument used in this work (Thermo Fisher Scientific, Nicolet iS20 spectrophotometer) was set to send infrared radiation of 10,000 to 100 cm^{-1} through the exanimated sample and to detect the resulting signal as a wavelength spectrum with a range of 4000.01 cm^{-1} to 550.09 cm^{-1} and a resolution of 4.00 cm^{-1} . The resulting signal represents a molecular characterization of the sample, relating the main peaks of the spectrum to the quantity of IR radiation absorbed and converted into rotational and vibrational energy by the sample molecules. The software OMNIC™ Spectra provided from Thermo Scientific was used for spectra identification tools and graphic representation. The test was achieved weighting 5 mg of the material of interest and pressing it on the surface of the instrument's lector. The analysis was repeated on three different samples for each set to guarantee the reliability of the measure. Because of the impossibility to get completely rid of the air on the tested sample surface, all the measures were normalized respect the air spectrum previously calculated to remove the environmental noise. The calculated spectra resulting from the Fourier Transform of the IR wavelength radiation were the % Transmittance and the % Absorbance of the sample.

As a first step in material's analysis process an FTIR analysis was carried out on the precursor powder used for the formulation's preparation. The Strontium doped Hydroxyapatite powder's spectrum was compared to the one of the natural Hydroxyapatite to analyze the effect of the Sr^{2+} substitution into the HA lattice.

Secondary, the mixed powder used for the blend's composition (PCL/10 Sr-nHa, PCL /20Sr-nHa) were tested to determine the presence of the characterized peaks of both constituent elements of the mixture. The PCL and SrHa spectra were also achieved with the same equipment and conditions from the purchased powder.

Finally, the same test was carried on the materials in the form of extruded filament's surfaces to analyze the manufacturing process on a chemical level. The aim was to analyse if the printing process influenced the chemical structure of the blend's constituents and if the contact surface of the scaffold offered a homogeneous leakage of the ceramic part into the PCL matrix. For this purpose, small squared 3x3 mm samples were printed to fill the lecture area of the instrument.

3.2.2 Contact angle analysis

The wettability of the printed surfaces was investigated by the measure of the contact angle on the three different materials. The principle consists of the measurement of the equilibrium contact angle formed in the case of a liquid in contact with a solid and a gas. The surface energy of the solid σ_s acts along the solid surface while the surface tension of the liquid phase σ_l acts tangential to the drop surface. As a result, the solid-liquid interfacial energy σ_{sl} acts in the opposite direction in order to balance the other tensions. The contact angle θ measured, is proportional to the forces applied on the surface and their thermodynamic equilibrium. It provides information about the energy of the solid and the interfacial tension, generally unknown parameters. (Figure 3.4)

For the purpose, a CAM 200, Optical Contact Angle and Surface Tension Meter equipment was used. The contact angle measurements were performed on flat surfaces using suitable rectangular scaffolds (5x5x2 mm) printed in bulk. Five different samples for each composition (PCL, PCL/10 Sr-nHa, PCL/20Sr-nHa) were analyzed. The samples were placed on the platform and focused by a camera (Firewire CCD Camera, with a resolution of 512x480 pixels and LED based background lighting). A deionized water drops of 5 μ l volume, provided by the equipment's dispenser, was dropped out from a needle and placed on the upper surface of the tested sample. The camera equipped with a unique monochromatic light source, which generates the highest quality images with minimal sample heating, was used to capture images of the drop's shape. The telecentric lens and high-resolution CCD camera ensure that these images are captured and transferred to the software without distortion or degeneration. Image analysis was performed by the CAM200 software fitting the profile curve to the Young-Laplace equation.

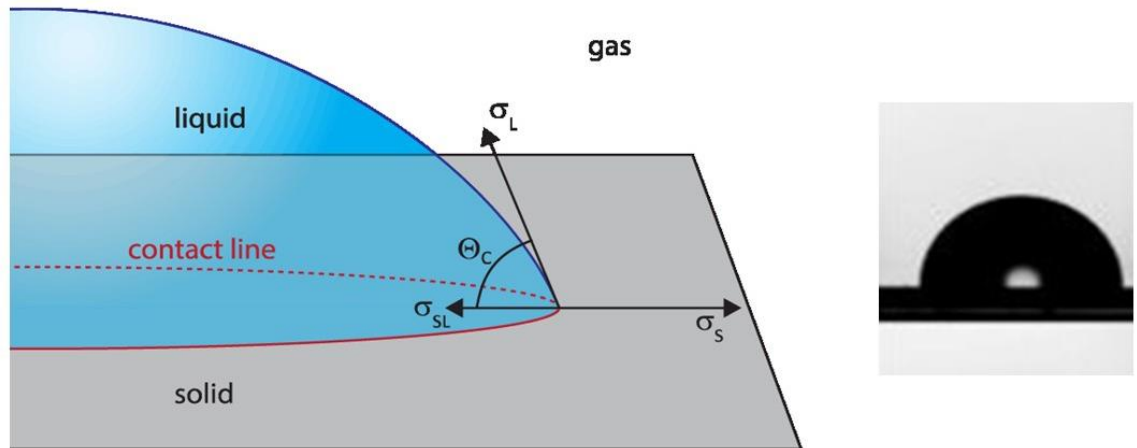


Figure 3.4 (141) Schematic representation of the contact angle measurement and a droplet picture obtained during the measurement with CAM 200, Optical Contact Angle and Surface Tension Meter

3.2.3 TGA analysis

TGA (thermogravimetric analysis) was performed in order to examine the printed materials' thermal behavior and to assess the actual composition of the printed materials. TGA is one of the most common thermal methods used for this purpose and exploits the effect of heat on materials to bring out mass changes related to chemical decompositions or reactions (142) (143). The device consists of a "Thermobalance" that measures the weight loss of the samples caused by material's degradation induced by the temperature's variation inside the chamber. The schematic diagram in Figure 3.5 (144) shows the main components of the device. It consists of a sensitive recording balance maintained inside a furnace designed for a specific temperature range or response time. The sample, inserted in an alumina crucible, is putted in a controlled atmosphere of inert or reactive gas such air or nitrogen and its weight is measured by a balance mechanism that employs an electromagnetic compensation principle whereby a beam carrying the sample and the counter mass are suspended from a coil of a galvanometer(145). Mass changes induce a pivot rotation and causes a variation of the current inside the coil. The signal related to the current or the voltage needed to maintain equilibrium is proportional to the weight loss and is digitalized and processed by a dedicated software. The true temperature of the sample is measured by a thermocouple placed as close as possible to the sample since it

cannot be approximate to the temperature of the furnace itself. In the event of chemical reaction, indeed, the temperature of the sample will be affected by the changing enthalpy and might be above the furnace temperature for exothermic decomposition.

The sensitivity of most balances is of the order of 1 microgram.

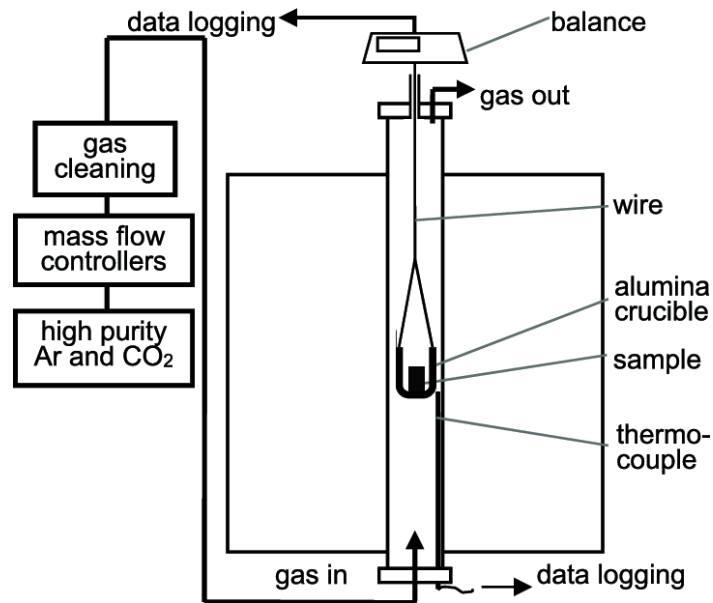


Figure 3.5 Schematic diagram of a Thermobalance (144)

The main object of interest in this study was to evaluate the amount of the ceramic content in the extruded filaments and to analyze the effect of the printing manufacturing process on the composition of the final scaffold. For this purpose, the three formulations were tested (PCL, PCL/10 Sr-nHa, PCL /20 Sr-nHa). The equipment used for the test was a TGA2 METTLER TOLEDO™ (SF) with a resolution of 1 µg, weighing accuracy of 0.005% and weighing precision of 0.0025%. The dedicated software STARe™ was used as an interface with the device to process the obtained information. The curves were processed using Matlab and the statistical analysis were carried on calculating the average and the standard deviation for each composition.

TGA analysis was performed in air and the initial weight of the samples was measured approximately around 10 mg for every test. The resulting curves were normalized to the

initial mass weight for each sample. Three samples for each composition were tested in a range of temperature between 25 and 800 °C with a heating rate of 10°C/min.

3.2.4 SEM analysis

The extruded surfaces of the printed materials were scanned with Scanning Electron Microscopy (SEM) technology in order to analyse the surface's morphology and visualize any difference among the three different formulations (PCL, PCL/10 Sr-nHa, PCL /20Sr-nHa) after the printing process. The technology used provides topographical and elemental information in a magnification range of 10X to 300,000X, with virtually unlimited depth of field.

The functionality is based on a focused beam of electrons scanned across the specimen's surface putted into a High vacuum-isolated chamber of 10^{-3} Pa. The data-processing of the back scattered secondary electrons produced is used to provide a topographical image of the specimen surface. Figure 3.6 (146) shows the principle of operation of the machine.

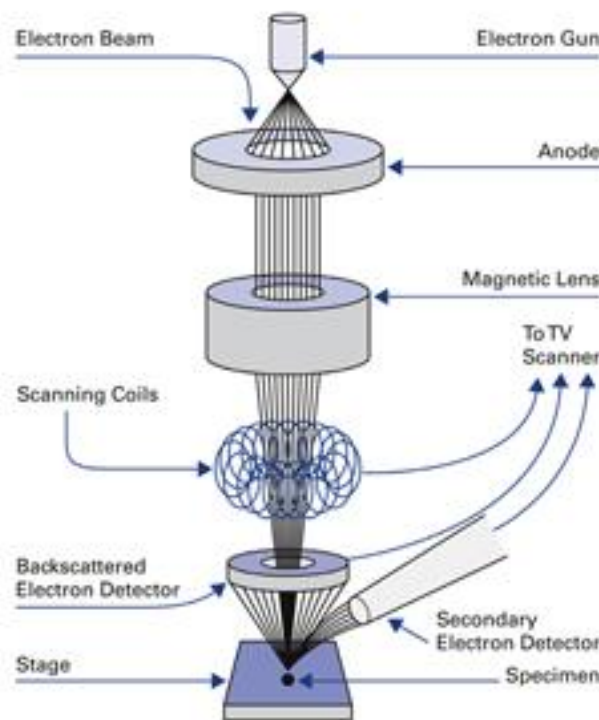


Figure 3.6 Scheme of a SEM technology functionality (147)

Briefly, SEM technology requires an electrical system to produce an electron beam. The electron gun produces the emission of thermoelectrons from a tungsten filament (cathode) heated at high temperature (2800K). The positive voltage (between 1 to 30 kV) applied between the anode and the cathode generates the electrons accelerations creating the focused beam. Two different stage lenses combined by magnetic lens and a scanning coils are located below the electron beam, enabling the adjustment of the diameter of the electron beam and the probe current. The fine electron beam obtained hits the sample's surface and after the interaction between the material and the particles a new flow of secondary and backscattered electrons is generated. A secondary electron detector is used for the detection of the backscattered electrons from the specimen in order to process the image. The high voltage applied to the detectors attracts the secondary electrons allowing the interaction with a scintillator (fluorescent substance) coated on the tip of the device. The light produced is directed to a Photo Multiple Tube (PMT), converted into an electric signal, amplified and transferred on a display unit(146) (148). The images' quality is influenced by different and interconnected factors such as the voltage at which the electrons are being accelerated, the convergence angle of the electron-beam cone, the beam current that hits the sample and the spot size of the beam. It is crucial for the user the necessity to find a good compromise between those parameters in order to achieve high- resolution images, to preserve of the sample's integrity, to guarantee a controlled signal-noise ratio and a small contrast resolution. (146) (147) (149)

During the study, the discussed parameters were optimized to obtain the best quality of the images. Before the scans, all the samples were coated with a conductive metal layer of Au to overcome the charging effect of the PCL surface caused by the interaction with the electron beam. The Au layer was deposited by diode sputtering process keeping the samples into the deposition chamber for 4 minutes. During this process the Au ions were generated by the collision of a sputtered gas (Argon flow power of 20W and flow Pressure of 10 Pa) on the surface of an Au target with 99% purity. The coated samples were placed on the SEM stage covered by a copper conductive tape and analysed using an electron probe of 7 kV voltage and a current intensity on 30 A. Different pictures were captured at different levels of resolution trying to maintain the working distance of each image unchanged (approximately around 6 mm). In order to investigate the surfaces'

characterization at different levels of magnification, the resolutions were set at 500 μm , 100 μm and 20 μm respectively

3.2.5 Scaffold mechanical behavior

The mechanical properties of the tri-phasic scaffolds were tested in compression and by comparing the results with those obtained by testing the bare PCL printed samples. During the test, the samples were placed in between two plates that distributed the applied load across the entire surface area of two opposite faces of the test sample. The samples' diameter and height were individually measured before the test and inserted into the processing data system to guarantee a higher accuracy of the measure. The principle of operation of the equipment is based on the collection of Data in a situation of constant load's variation. The strain along the longitudinal direction was calculated from the displacement's measure obtained by an extensometer that measured the distance between the upper and lower compression plates. The strength loaded on the sample was obtained multiplying the pressure applied by the machine with the actual surface of the sample. The test was carried out in an environment maintained at a temperature of 19°C and 50% of humidity. Two parallel stop conditions were set on the test: the reach of 490N of strength applied and the reach of 50% strain on the sample's deformation. The information was processed by using a Matlab program and The Elastic Modulus of the specimens was obtained by the calculation of the slope of the most linear part of the stress-strain curve (generally in the range between 2% and 8% strain) individually and manually selected for each sample.

Five specimens for each type were tested and data expressed as average and standard deviation. Figure 3.7 represents an image captured during a compressive test of a sample.



Figure 3.7 Compression test of a 3D scaffold

3.2.6 Micro CT analysis

The topology and architecture of the printed scaffolds were analysed by a SkyScan 1275, Bruker μ CT 2016.

The micro CT technology permits the investigation of the three-dimensional details of objects' structures by the interpolation of the two-dimensional information coming from 2D images obtained by an x-Ray system, into a three-dimensional structure model.

The Bruker Micro CT device offers a combination of systems and software that cover three major topics: image acquisition, image reconstruction and post data processing.

The physical basis of micro-CT techniques is that material attenuating the X-ray beam passing through it cause an attenuation rate that depends on X-ray energy and composition of the object. The intensity of the transmitted X-rays is related to the incident X-ray intensity as expressed by the Lambert-Beer law (148):

$$I = I_0 e^{\left(\frac{-\mu}{\rho}\right)\rho x} \quad \text{Equation (1)}$$

where I_0 is the intensity of the emitted X-ray beam, and I is the beam's intensity after it cross a thickness of material x , characterized by a linear attenuation coefficient μ . ρ is the

linear density of the material and the term μ / ρ is the mass attenuation coefficient (cm^2g^{-1}) (150).

The fundamental components of any micro-CT instrument are a penetrating ionizing radiation, a sample manipulator, and a detector. X-rays are generated by a micro-focus x-ray tube, which uses a beam of electrons accelerated by a voltage of up to 240 kV and are focused onto a tungsten or similar metal target. The interaction between the fast-moving electrons and the metal target is responsible for creating x-rays. The x-rays are then directed through the sample before being collected on a 2D x-ray detector(151). In Figure 3.8 the basic principle of the acquirement of a projection image of the specimen is illustrated. The obtained 2D X-ray shadow image represents a two-dimensional projection from the scanned object. With the approximation of a parallel irradiation, each point on the shadow image contains the integration of absorption information inside the three-dimensional object along the path of the corresponding partial X-ray beam. (152) (153) The sample is placed on a rotating stage and during the acquisition the object rotates over 180 or 360 degrees with a fixed rotation step. At each angular position a shadow image is captured. The Data acquired at this stage is a matrix $N \times N$ (N is defined by the number of pixels of the angular projection image). Each pixel value corresponds to absorption values in the reconstructed cross section and the grey scale is related to the material's density. The interval of the density window can be selected by the operator. Depending on the choice of the user, all attenuation values below the minimum will be black while everything above the maximum will be displayed as white. The reconstructed array will be shown as a half-tone image of the cross section with linear conversion to grey-scale inside the selected density interval.(151)

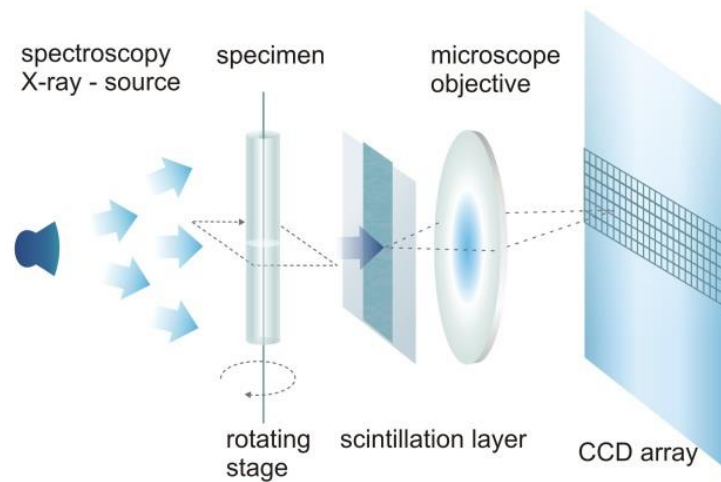


Figure 3.8 Configuration of a micro-CT scanner (adapted from (154))

The tested scaffolds were placed on the stage and inserted inside the x-ray chamber.

The SkyScan equipment, providing a dedicated software, enabled the possibility to change the acquisition parameters to obtain the best imaging performances. After the optimization of the parameters three samples for each type (PCL, PCL/10 Sr-nHa, PCL/20Sr-nHa) were tested. The stage was moved toward the x-Ray beam reaching an image Pixel Size of 10.00 μm . The voltage source was set to 30 kV and the current source was set to 250 μA . The images were taken after an exposition time of 48 ms during a rotation of the stage from 0 to 180 degrees with steps of 0.2 degrees. The supplied SkyScan NRecon package software was used to reconstruct cross-section images from tomography projection images. In Figure 3.9 the graph interface used to choose the density scale on a random cross-sectional image is shown

The volume rendering CTVol program was used to process the cross-section images and display the reconstructed results as a realistic 3D model. The 3D models are created in the program CT-analyser ("CTAn"). The two SkyScan programs CTAn and CTVol working together in a complimentary way allow the operator to take best advantage of the functions of images binarization plus the image processing steps such as despeckling to remove noise dots, and many more functions. (155)

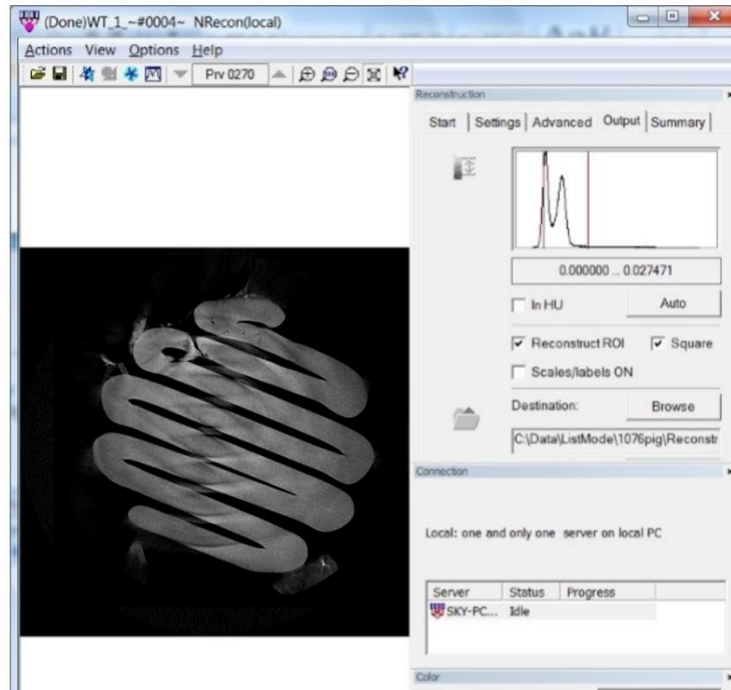


Figure 3.9 Choice of the density scale operating with NRecon software on a random cross-section image

CT-Analyzer was also used for measuring quantitative parameters of interest such as the open and close porosity of the scaffolds. The workflow of the five different steps achieved by CT-An software for the processing of the cross-sectional images is illustrated in Figure 3.10.

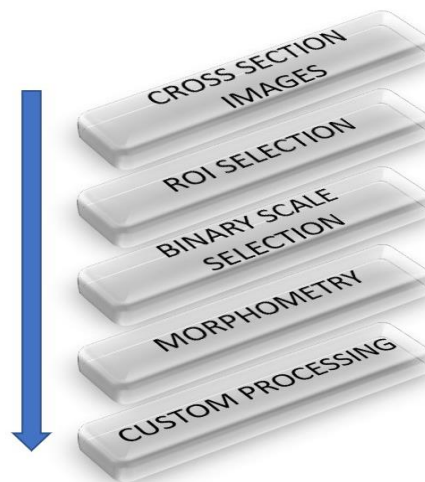


Figure 3.10 CT-Analyzer is organised into five stages for optimal and intuitive workflow

3.2.7 Theoretical calculation of scaffold's porosity

In this study the theoretical porosity was evaluated directly from the built geometry since the structure was projected and designed by CAD programs before the printing process. For the calculation the following formula was used (156):

$$\text{Porosity} = 1 - \frac{\pi d_1^2}{4d_2d_3} \quad \text{Equation (2)}$$

In which d_1 represents the diameter of the single strand of the scaffold, d_2 represents the gap between two adjoining strands calculated as the distance between the centres of the longitudinal axes of the strands and finally d_3 represents the height of each scaffold's layer. In Figure 3.11 a graphical representation of the parameters used in Equation (2) is presented.

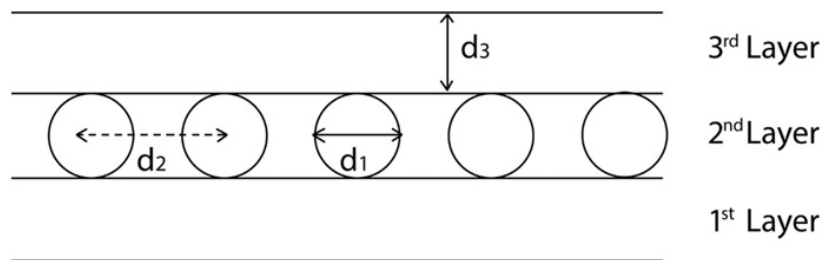


Figure 3.11 Illustration of the parameters used for the theoretical porosity calculation (3)

For the purpose, the parameters values were slightly adjusted for the calculation since it was noticed that the geometry of the printed strands was not perfectly round, but the shape of the extrusion was every time dilatated in the lateral direction because of the weight of the strands printed on the following layers. The corrective factors were calculated by analysing the micro CT cross sections and measuring the effective distances of the samples. In particular, the correction for $d_1 = 1.2$ and for $d_3 = 0.75$.

3.3 *In vitro* characterisation

In order to test the biocompatibility and the cytocompatibility of the printed materials, *in vitro* tests have been conducted on the printed samples. The purpose of the study was to test the two printed material formulations, and for this reason, it was decided to disassemble the two different phases of the scaffolds testing them separately (PCL, PCL/10Sr-nHa, PCL /20Sr-nHa). PCL scaffolds with the same geometry (7mm of diameter and 2.5 mm of height) were printed as a positive control for each test.

In this study Human Bone Osteosarcoma Epithelial Cells (U2OS Line) were cultured in McCoy's growth Medium (modified with L-glutamine, phenol-red and sodium bicarbonate) containing 10% of Fetal Bovine Serum, Heat-Inactivated (FBS-HI, Gibco) and 1% of antibiotic agent (Penicillin-Streptomycin, Gibco).

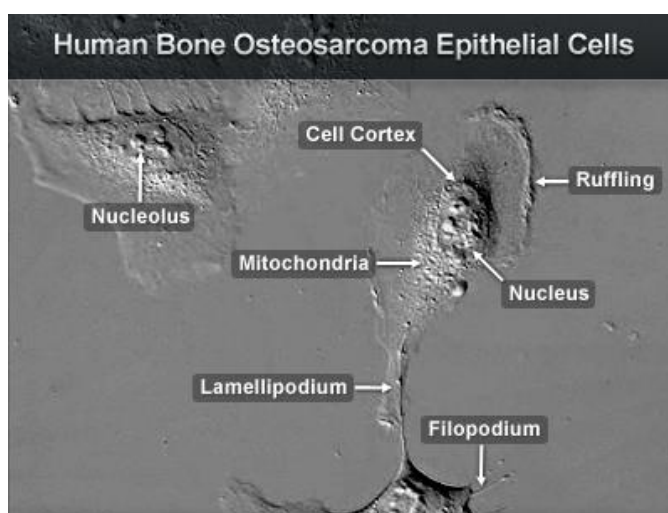


Figure 3.12 U2OS epithelial cells, Fluorite 40x magnification captured with a Nikon TE2000/DIC (157)

The entire work was carried on using a laminar flow hood that, providing an aseptic working area allows the minimization of infectious splashes or aerosols generated by many microbiological procedures. The Microflow Peroxide Class II advanced biological safety cabinet (Astec Microflow) present in the Lab, provides operator and product protection for work with up to category 3 pathogens. During the experiments all the items used and placed inside the hood were disinfected by spraying them with 70% ethanol and the workspace was wiped clean in order to avoid every kind of contamination during the study.

Figure 3.13 show the flume hood used in this study loaded with some of the items described: flasks, waste bin microtubes and Pasteur pipettes.



Figure 3.13 The flume hood (Astec Microflow) containing the main items used for the study.

3.3.1 Scaffolds sterilization

After the manufacturing process the three different types of printed samples were placed into a 24 well plate and sterilized before the start of the cell work. The sterilization was conducted in two steps. First, working inside the hood, 1ml of IPA (Honeywell, Isopropyl alcohol) was added in each well completely submerging the scaffolds' geometry. After 15 minutes the solution was removed, and the samples were washed three times with PBS (Phosphate-buffered saline, Sigma Aldrich) and transferred into a new well plate. Then, the samples were placed under an UV lamp (BioSan DNA/ RNA UV cleaner, $\lambda = 253.7$ nm) for 20 minutes. The irradiation was repeated for on the bottom surfaces of the scaffolds by turning them on the other sides by sterile forceps. The well plates were wrapped with parafilm tape and placed in sterile conditions into the hood until the following test procedure

3.3.2 Cell seeding

Cells were seeded on the top surface of the cylindrical scaffolds. The flask containing the U2OS cells at passage 7 was used once cells reached approximately the 70% of confluence. The culture medium was removed from the flask and cells were washed with 10 ml of PBS before the detachment. 4 ml of Trypsin (Sigma-Aldrich, 0.25% concentration, UK) were added and the flask was placed in incubation for 4 minutes (37 °C, 5 % CO₂, 95 % air). This protease enzyme, catalyzing the hydrolysis of peptide bonds, produces the break of proteins into smaller peptides and is used to cleave proteins holding the cultured cells to the plates. The re-suspended cells were then counted using a color staining assay. Briefly, in this procedure, 30 ul of Trypan Blue solution (0.4%, liquid, sterile-filtered, Sigma-Aldrich, UK) were mixed with 30 μm of cells suspension into a sterile microtube. 10 μl of the mixed solution was displaced on the glass and placed under the cells counter equipment. The blue dye penetrating into live cells' membranes allows the measurement of cells viability from the device, providing also information about the percentage of the dead cells into the suspension. Once its concentration was calculated, the cells suspension was centrifuged (Thermo Scientific TX) at 1000 RPM for ten minutes and the supernatant was carefully poured into the waste bin leaving the cells pellet attached on the bottom of the vial. New fresh media was added in order to reach a final concentration of cells into the suspension of 100 000 cells/ml. Scaffolds were finally seeded by placing a drop (50 μl) of cells' suspension on their top surfaces. The pipetting action was performed carefully to let the drop to remain above the surface avoiding its absorption inside the sample's pores. Substrates were incubated under standard conditions (37 °C, 5 % CO₂, 95 % air, humidified environment) for 3 hours after which 950 μl of fresh media was added in every well reaching a total volume of 1 ml. The well plates were placed into the incubator and maintained under the same standard conditions. The media was changed every three days in order to replenish nutrients and keep the correct pH for the entire studies' duration.

3.3.3 Cell viability: MTT for cells metabolism measurement

The MTT assay is a colorimetric assay used in this study to assess cells' metabolic activity (158).

MTT is a yellow tetrazole that is reduced to purple formazan in living cells. This reduction is generally assumed to be dependent on NAD(P)H-dependent oxidoreductase enzymes largely present in the cytosolic compartment of the cell. The reduction of the two molecules is illustrated in Figure 3.14. A solubilization promoting agent is added to dissolve the insoluble purple formazan product into a colored solution. The absorbance of this colored solution can be quantified by measuring at a certain wavelength (usually between 500 and 600 nm) by using a spectrophotometer and it provides a direct connection with the cellular metabolic activity and consequently with cells' viability. (159) (160)

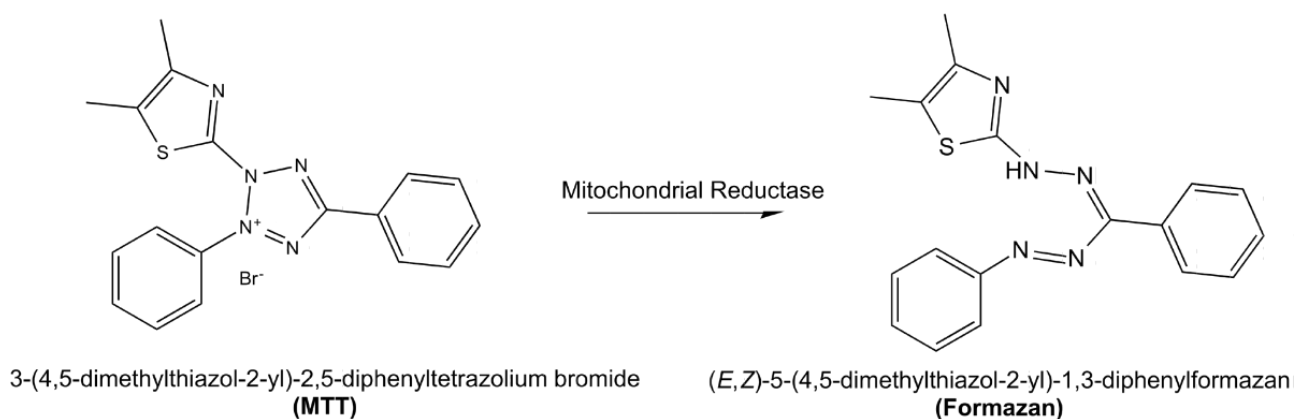


Figure 3.14 The reagent and the product of the MTT reduction catalyzed by the mitochondrial reductase (159)

The test was carried on at different time points: 1, 3, 7 days and in triplicate. The MTT solution (Sigma-Aldrich, 4% weight/volume), once prepared, was retained in small aliquots and stored in a dark place at 2°C. During the test, 100 µl of the solution was added in each well (10% of total well volume). The wells were left in incubation for 3 h at 37°C, 5% CO₂ with protection from light allowing the MTT reduction and the formazan's crystals formation. After the reaction, the liquid was removed from each well and replaced with 800 µl of IPA (Honeywell) solvent. Samples were placed for 30 minutes at room temperature with light protection on a mechanical shaker set with an angular velocity of 40 RPM encouraging the formazan dissolution into the IPA solvent. The liquid was mixed up and down using a pipette in order to obtain a homogeneous solubilization. Subsequently, 200 µl of volume were dispensed inside a 96 well plate in order to quantify the MTT reaction occurred in each sample. The plate was placed into a microplate reader of a scan equipment (Sunrise™, Tecan) and the absorbance of each well was spectrophotometrically measured at a wavelength of 562 nm. The Magellan™ software,

connected to the device, was used as interface to set the measurement's parameters and obtain the absorbance lecture of the test.

3.3.4 Cell viability: DAPI assay

DAPI is a cytofluorometric assay used in this study to evaluate cells' attachment on the examined substratum, additionally to the fact that it can provide a total count of the cells. DAPI (4',6-diamidino-2-phenylindole) is a blue-fluorescent stain that binds strongly to Adenine–Thymine rich regions in DNA. It can permeate inside cells' membranes and, when it is bounded to double-stranded DNA, has an absorption maximum at a wavelength of 358 nm (ultraviolet) and its emission maximum is at 461 nm (blue). The use of the fluorescence microscopy enables then the nuclei visualization after the staining assay and provides information about cells' proliferation and migration inside the scaffold's pores (161).

Epi-fluorescence microscopy is the technology that assists to observe the fluorescence produced by substances called fluorophores. The system contains a light source for excitation (usually mercury lamps) and a filter block to separate the excitation light from the fluorescence. Filter blocks consist of an excitation filter, an emission filter and a dichroic mirror. The excitation filter (a bandpass filter) is the optical element that passes only the wavelength of light necessary for excitation from the excitation light source to the fluorophore. The dichroic mirror, rotated of 45° to the incidence light, reflects the wavelength of the exposition light and transmits the others, to achieve the separation between source light and detected fluorescence. Barrier filters are optical elements that separate fluorescence emanating from the fluorophore from other background light. This last filter is necessary for images visualizations because of the weakness of intensity of the fluorescence light compared to the irradiation one (100,000:1). In the whole process, then, the light filtered through the excitation filter is deflected by 90° and directed to the specimen. The fluorescence emitted passes through the dichroic mirror and is filtered by the Barrier filter and directed toward the digital camera for the acquisition (162). In Figure 3.15 a scheme of the filter block in fluorescence microscopy is presented.

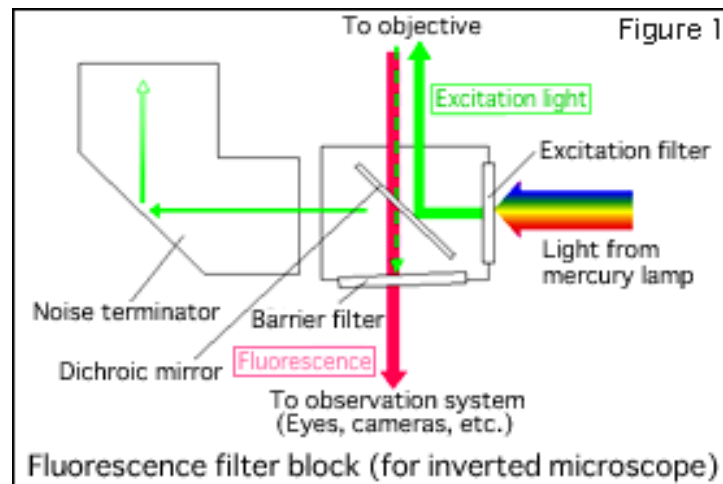


Figure 3.15 Scheme of the filter block in fluorescence microscopy (162)

The test was performed at two different time points: 3 and 7 days after seeding. The test was carried out by testing two samples of each printed formulation for both time points. During a preliminary step of the procedure, the DAPI intermediary dilution (300 μ M) was produced by diluting the DAPI Thermo Fisher STOCK solution (5 mg/ml, 14.3 mM) in PBS with a DF of 47.6 and stored in the dark at 2°C until use. The DAPI working solution (300 nM) was prepared in the hood through a further dilution of the previous one in PBS, with a DF of 1000, and used for the staining assay.

The medium was removed from the culture well plates and scaffolds were washed two times with 1 ml of sterile PBS. Cells were chemically fixed on the scaffold's surface by adding 1 ml of PFA (Paraformaldehyde, Sigma-Aldrich, 4% in PBS, pH 7.4) and leaving it for 8 minutes at room temperature. The formaldehyde is a toxic transparent gas that reacts with primary amines on proteins and nucleic acids to form partially reversible methylene bridge crosslinks. The PFA (polymerized formaldehyde), formed by precipitation in aqueous formaldehyde solutions, was used for fixing cells since it causes covalent cross-links between molecules, effectively gluing them together into an insoluble meshwork, enabling the following membranes' penetration of the DAPI staining (163). The PFA was removed and cells were washed two times with PBS. 800 μ l of DAPI solution was added in each well to completely submerge the scaffold's volume into the staining reagent. After 10 minutes of incubation in a dark place at room temperature, samples were washed two times with 1 ml of PBS. Then samples were stored by fixing them to microscope glass slides with a drop of transparent nail varnish, adding 1-2 drops of mounting medium (Sigma-Aldrich, UK) and covering the top layer with a glass cover slip. Samples were placed in the freezer at 2-8 °C, in

dark until images' acquisition. For the purpose, an upright Fluorescence Microscope (Nikon ECLIPSE 80i) was used. A filter with a range between 350 to 450 nm of wavelength was set because the DAPI's absorbance peak is included in this interval. The samples were placed on the stage and the portion was moved to be viewed into the optical path. Different images were captured using 20x and 10x objective to investigate the scaffold's surface and the cells' dispersion at different levels of magnification. A filter number four was applied to minimize the autofluorescence of the PCL that would affect the images in term of contrast between the nuclei and the background noise.

3.3.5 Cell morphological analysis

Cell adhesion to a tissue engineering scaffold is. SEM technologies are used in in this study to investigate cells' attachment on the substrates, as important regulator of cell behaviour and tissue regeneration, and to analyse their morphology after the seeding time.

The test was conducted after 1, 7 and 14 days and two samples of each material were seeded for each time point. During the procedure, the Medium was removed from the well plates and cells were washed twice with sterile PBS. Cells were then chemically fixed to the substrates by adding 1ml of 2.5 % Glutaraldehyde in deionized water. After 45 minutes of incubation at room temperature the fixing reagent was removed, and the samples were washed with 1 ml of PBS three times. The plates were then moved to another fume hood designated to osmium work. Cells were fixed on the substrates' surfaces by adding 3-4 drop of osmium (Sigma-Aldrich, 1% Osmium Tetroxide solution in water), just enough to cover substrates. The Osmium Tetroxide was used as a post fixator element. In fact, it is used to enhance and preserve the strength of crosslinks between cells and surfaces before the electron scansion(164). After 10 minutes' samples were washed three times with deionized water. The following passage involved a dehydration of cells using alcohol series. 1 ml of crescent ethanol concentration 25, 50, 75, 90 % in deionized was were added to the well plate and left for 10 minutes before the substitution of the following dilution. Later on, 1 ml of ethanol 99.9% of concentration was added and left inside the well plate for 10 minutes. Finally, cells were chemically dried in 100 % Hexamethyldisilane (HMDS, Sigma Aldrich) by adding 3-4 drops on the scaffolds' surfaces. The well plate was left overnight at room temperature with protection for light. Samples were stored and then analyzed by

the same scanning electron microscope (SEM) device previously described to investigate cell's attachment on their surfaces. The setting parameters used were chosen to not cause any cells' damage and guarantee a production of good resolution images at different depths. The Electron beam was accelerated by 5 kV of voltage and the current source was 30 A. Different pictures were captured at different level of resolution trying to maintain the working distance (approximately 6mm) of each image unchanged as far as possible. In order to investigate the surfaces' characterization at different levels of magnification, the resolutions were 500 μm ,100 μm and 20 μm respectively.

3.3.6 Osteogenic potential

For the test, a set of three scaffolds for each formulation were printed, seeded and harvested on days 7, 14, 21 and 28. The procedure used started by removing the Medium from the wells and samples were washed three times with sterile PBS. A solution of 4% Paraformaldehyde in deionized water (Sigma-Aldrich Ph 7.4) was added to the wells and the plate was incubated for 15 minutes at room temperature. After the completion of the fixing process, cells were washed three times with DPBS/ 0.1% TWEEN20 solution (Sigma-Aldrich, polysorbate 20, Polyoxyethylene Sorbitan monolaurate, PEG) (20). Surfactants (surface acting agents) are amphiphilic molecules, containing both hydrophilic and hydrophobic regions commonly used as detergents to break protein-protein, protein-lipid and lipid-lipid association. TWEEN20 is a polysorbate surfactants with a fatty acid ester moiety and a long polyoxymethylene chain and it is used for its gentle reaction with membranes' proteins, promoting their effective solubilization without any alteration on their activity.(165) Into the wells was then added 1 ml of water/0.1M Tris solution (Sigma-Aldrich). Tris is used to make a basic buffering solution since the alkalisation of the substrate is crucial for ALP release. After 25 minutes of incubation the alkaline solution was replaced in wells with 1 ml of liquid yellow ALP solution (*p*NPP Sigma Life Science). Samples were incubated at room temperature in dark and placed on a mechanical shaker at 40 RPM for 30 minutes. After the ALP reaction, 100 μl of solution was then taken from each well and placed in a 96-well plate to quantify the enzyme activity. The reading was performed in spectrometer using a Tecan Scan™ equipment at 405 nm. The absorbance measurements were then connected to the concentration of the enzyme by creating a standard calibration 8-points curve 8 different known concentrations from 200 to 0 ng/mL

(200, 100, 50, 25, 12.5, 6.2, 3.1, 0 ng/ml) to the wells. The calculation of the standard curve was processed by Matlab and the obtained values were fitted with best fit method, interpolating the minimum squared error of each measure.

To obtain an information about the amount of the ALP enzyme over the total number of cells the information was normalized on the measurement of the total amount of proteins in each sample. For the purpose, the BCA test was carried on (Thermofisher, Pierce™ BCA Protein Assay Kit). The principle of the assay is based on the measure of the spontaneous reduction of Cu^{2+} to Cu^{1+} by proteins in an alkaline medium. The first step is the chelation of copper with protein in an alkaline environment (Biuret reaction) to form a light blue complex. In the second step, bicinchoninic acid (BCA) reacts with the reduced (cuprous) cation that was formed in step one producing an intense purple-colored reaction product, results from the chelation of two molecules of BCA with one cuprous ion. The absorbance measured at 562 nm is related to the amount of the complex formed during the reaction and consequently to the total protein concentrations. (166) (167) Following the procedure of the kit, the Medium was removed from the wells and cells were washed three times with 1 ml of sterile PBS. Into each well was added 1 ml of Tryple Express (Gibco TrypLE Thermofisher scientific) /1% Triton X-100 (Sigma Aldrich) and the plate was placed in incubator at 37°C for 30 minutes. Triton X is a non-ionic surfactant used to permeabilize cells' membranes facilitating protein's release during the process while the Tryple Express is a highly purified, recombinant cell-dissociation enzymes preferred to trypsin because of its gentle action on cells' surface proteins protecting their epitope's shape (168). After the incubation the detergent produced the detachment of cells from the substrates and the cell suspension was collected into sterile microtubes using sterile pipettes, trying to carefully wash the sample inside the porosity to completely detach cells. Microtubes were then freeze at -85° C for 8 minutes and let them thaw. The process was repeated three time following the same procedure. After the completely thawing, samples were micro centrifuged at 14 000 RFC at 4°C for 10 minutes to separate cells bodies deposited as a pellet on the bottom of the microtubes, and collect the supernatant containing the released proteins. 600 µl of the supernatant was collected and transferred into new sterile microtubes using plastic pipettes. For the test the BCA working reagent provided by the kit was prepared. Aliquot of samples (10 µl per well) were transferred into a 96 well plate and performed in triplicate. Into the wells 200 ul of the BCA working reagent were added. The

plate was cover in foil and mixed for 5 minutes on a plate rotator (40 RPM) and incubated for 30 minutes at 37°C. Afterwards, the plate was cooled down and rested at room temperature for 30 minutes. The Tecan Sunrise™ equipment was used at this stage to measure the absorbance of the samples at 562 nm. To a 9-points standard BCA curve was created (2000, 1500, 1000, 750, 500, 250, 125, 25, 0 µg/ml). The dilutions were prepared from the BCA standard stock provided at a concentration of 2 µg/ml and the diluent was the same used to dilute the proteins into cells suspension (Tryple Express/ 1%Triton X-100). The ALP/ total proteins content ratio was the indicator used to evaluate the transition between the proliferative and the differentiative phase in cells' growth and quantify the differentiative phenomenon during the time of the experiment.

3.3.7 Scaffold's mineralization potential

The alizarin red staining was used with the purpose to get qualitative images to investigate the mineralization potential of the scaffolds in terms of production of hydroxyapatite by cells. The aim of the study was to compare the reaction of the stain on the three materials and check the different mineralization in scaffolds containing SrHa particles (10 and 20 % (w/w). Alizarin Red (3,4-Dihydroxy-9,10-dioxo-2-anthracenesulfonic acid sodium salt) is a commonly used stain to identify calcium in tissue sections and cultured cells in vitro. Calcium forms an Alizarin Red S-calcium complex in a chelation process, and the product is characterized by the formation of a bright red stain (169).

In this biochemical colorimetric assay two printed specimens for each formulation were tested. In order to evaluate the progressive action of mineralization in cells culture the test was achieved after 7, 14, 21 days. Furthermore, a different bunch of scaffolds was prepared to perform the same assay without seeding cells on the surface (this will be Day 0 of the study). The dye solution was prepared by adding the Alizarin red powder (Sigma Aldrich) in deionized water (2% Weight/volume). The Medium was removed from the wells and 1 ml of the staining solution was added in each of them. After an incubation time of 30 minutes, the Alizarin red solution was removed, and scaffolds were washed 8 time until the complete removal of the dye. Scaffolds were then transferred into a new well plate and the top surface morphology was analysed by optical microscopy. The device used was an Olympus™ CKX53 Inverted Microscope equipped with a 5X magnification objective. Images

were taken with the same magnification contrast and resolution to guarantee the reliability of the prove.

3.4 Statistical Analysis

All the experiments were repeated at least three times to ensure the reproducibility and the reliability of the test. The results are reports as means± Standard deviation (STD) to provide information about dispersion of the set data values obtained during the tests. The results were than analysed by two-way ANOVA followed by Dunnett's test of significance with a significance level of $\alpha=5\%$. P values ($p<0.05$) was considered statistically significant. Dunnett's test is a multiple comparison procedure, used for the calculation of the simultaneous inference of one consider set of data to others subset of parameters selected. In this study the PCL represents the positive control and the comparisons of the other materials were performed to the measure of this data set. (170) The analyses were performed by using Prism8 software.

Chapter 4: Results

4.1 Introduction

This chapter aims to show the results derived from the physico-chemical and *in vitro* characterization of the tri-phasic printed scaffold made of Sr-nHa ceramic phase and PCL matrix. The PCL scaffold was used as a comparative control in each test in order to test both the geometry and the enhancing biomimetic properties obtained by the introduction of the bio-ceramic component into the polymeric phase.

The first section of the chapter is dedicated to the presentation of the scaffold's design and its physico-chemical and mechanical characterization. The investigation of the precursor materials used for the printing process and the manufacturing process's optimisation results will be presented. The FTIR spectra of the three tested material (PCL, PCL/10Sr-nHa, PCL /20Sr-nHa) of the extruded surfaces are compared with the ones achieved by the analysis of the precursor materials' powders. The thermogravimetric curves obtained from the TGA will characterize the thermal stability of the used materials moreover providing evaluation about the % amount of the ceramic Sr-Ha content inside the extrusions. Will follow the results of the contact angle measurement and the presentation of the SEM images for the morphological and topographical characterization of the printed strands' surfaces. The images of scaffolds' volume reconstruction, obtained by micro-CT technology, will be presented for the morphological characterization of the scaffold geometry and the resulting calculation of scaffold's porosity will be compared with the theoretical one. For the mechanical evaluation, the stress- strain curves obtained from compressive tests are presented as well as the results of the Elastic modulus calculation.

In the second section of the chapter, the results relative to the cell work carried on the printed samples are shown. The aim was to test the biocompatibility of the two materials (PCL/10Sr-nHa, PCL /20Sr-nHa) that form the Tri-layered scaffold separately and compare every prove with the PCL positive control scaffold with the same design. Cells' viability is presented by quantitative analysis obtained from the MTT enzymatic assay and by qualitative visualization of the cell's nuclei attached on the substrates by DAPI cytofluorometric assay. The following presentation of the images, captured using the SEM

technology, will allow the investigation of cells' attachment and morphology on the different substrates after their chemical fixation on the surfaces. Will follow the results of the ALP colorimetric assay, as a marker of osteogenic potential. The results of the absorbance measure are shown normalized to the total amount of proteins, calculated by BCA assay. The 8-point calibration curves, calculated for the concentrations' measurement of both the assay, will be also tabled. Finally, mineralisation potential results of the scaffolds assessed through Alizarin Red staining are shown as qualitative images taken *via* inverted microscopy.

4.2 Characterization of precursor powders and extruded filaments

4.2.1 FTIR analysis

The precursors ceramic powders were investigated by FTIR.

For this purpose, the spectra of the PCL powder, the Sr-doped Hydroxyapatite powder and the two polymeric/ceramic mixture (10% w/w and 20% w/w) were compared. In Figure 4.1 the presence of the polymeric (PCL) and ceramic (Sr-nHa) content is evident in both formulations (PCL/10Sr-nHa, PCL /20Sr-nHa). In particular, the PCL presence is shown by the absorbance peaks characterized by the C-H stretching (2943 and 2865 cm^{-1}), the C=O carbonyl group at 1720 cm^{-1} , and the CH₂ deformation band $1165\text{-}1468\text{ cm}^{-1}$, the backbone C–O and C–C stretching in the crystalline phase 1293 cm^{-1} , as well as the C–O–C symmetric and asymmetric band at 1239 cm^{-1} , 1164 cm^{-1} , 1107 cm^{-1} , 1047 cm^{-1} (171). At the same time, O-H and PO₄³⁻ groups, contained into SrHa hexagonal crystalline structure, form intensive IR absorption bands at 560 and 600 cm^{-1} and at 1041 cm^{-1} (172).

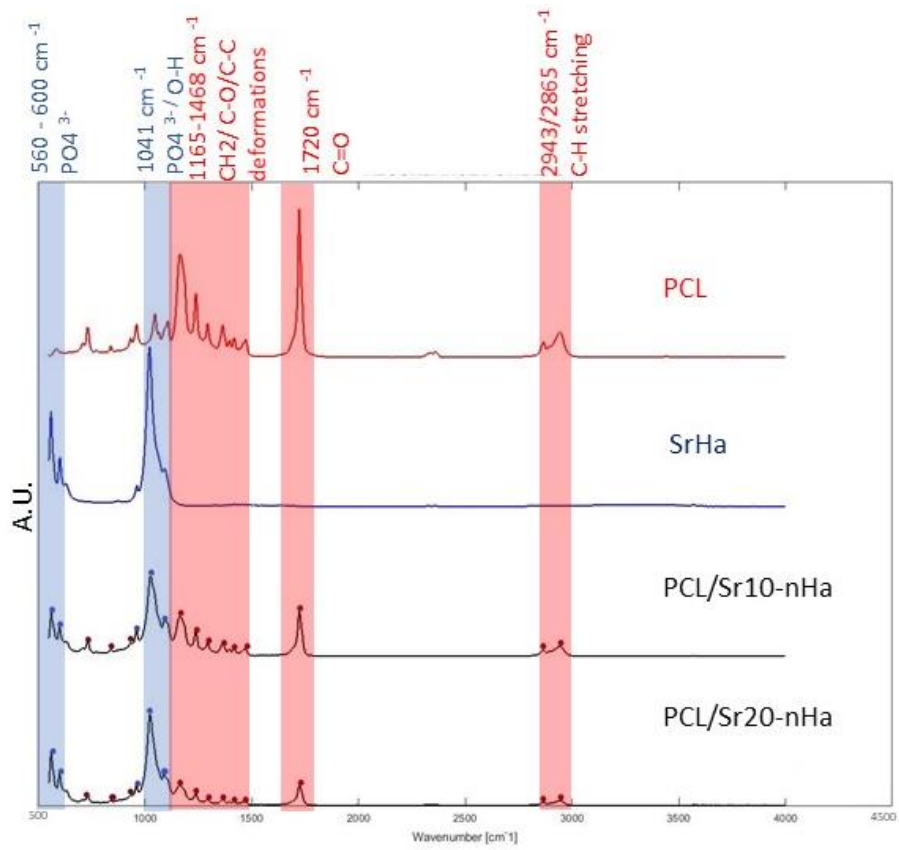


Figure 4.1 FTIR Spectra of powders (PCL, PCL/10 Sr-nHa, PCL /20Sr-nHa)

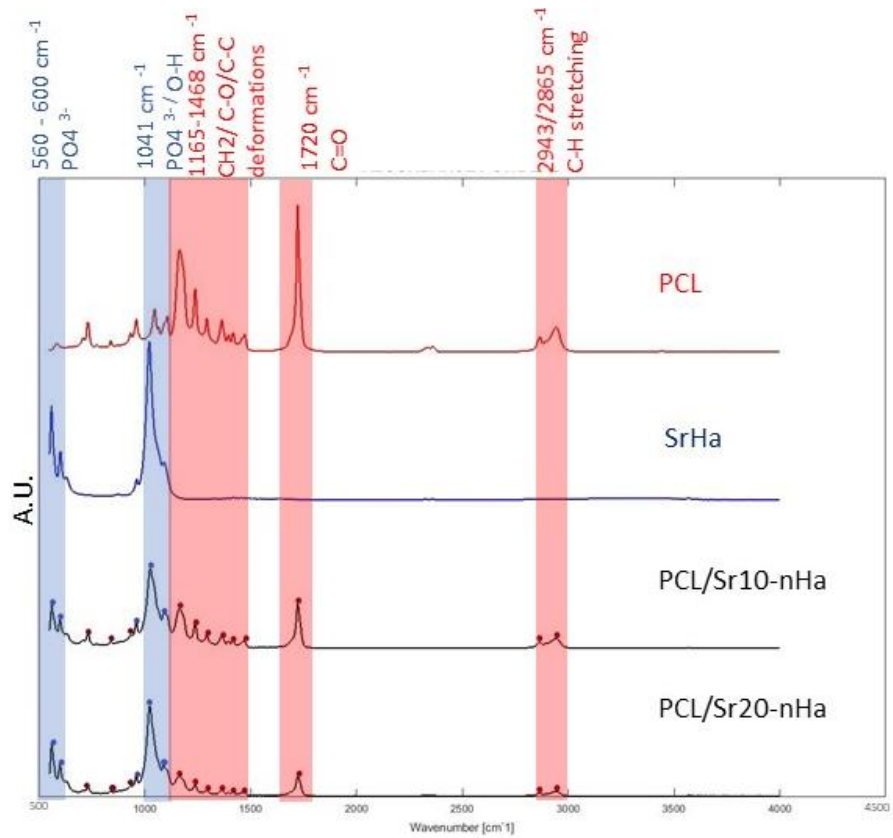


Figure 4.2 FTIR spectra of extrusions (PCL, PCL/10 Sr-nHa, PCL /20Sr-nHa)

After the extrusion, the presence of the polymeric phase (PCL) and the ceramic one (SrHa) is still evident in both blended formulations (PCL/10 Sr-nHa, PCL /20Sr-nHa). In Figure 4.2 the absorbance spectra of the extruded materials are presented and they show the presence of the characteristic peaks of the precursor powders into the composite materials: the blue points represents again the SrHa peaks while the red points are connected to the PCL absorbance. The PCL spectra does not change before and after the extrusion. Furthermore, the qualitative comparison between the extruded and the powder forms of the blended materials evidences that the ratio between the amplitude of the SrHa and the PCL peaks results significantly lower after the extrusion, marking a predominant detection of the PCL matrix on the printed surfaces.

4.2.2 TGA analysis

The extrusions of the three materials were analysed by thermogravimetric analysis. The TGA graph, presented in Figure 4.3, is used to investigate the decomposition temperature, the amount of the percentage residue after the degradation and the % weight loss respect to temperature range of 25 to 800 °C. The PCL samples curves (black) show a complete degradation in a single step reaction that starts at around 350°C and ends at 550°C with a maximum decomposition peak at 490.2°C.) The composite PCL/Sr-nHa samples display one-step degradation similarly to PCL bare samples and a single weight loss phenomenon, corresponding to polymer pyrolysis in the same range of temperature. It is evidenced that the SrHa presence has not a significant influence on the PCL's thermal stability and its degradation process. Since the SrHa degradation is estimated to begin in the range 1050-1100°C (174), the amount of the material measured by the balance at the end of the test is related to the amount of the ceramic phase present into the tested samples.

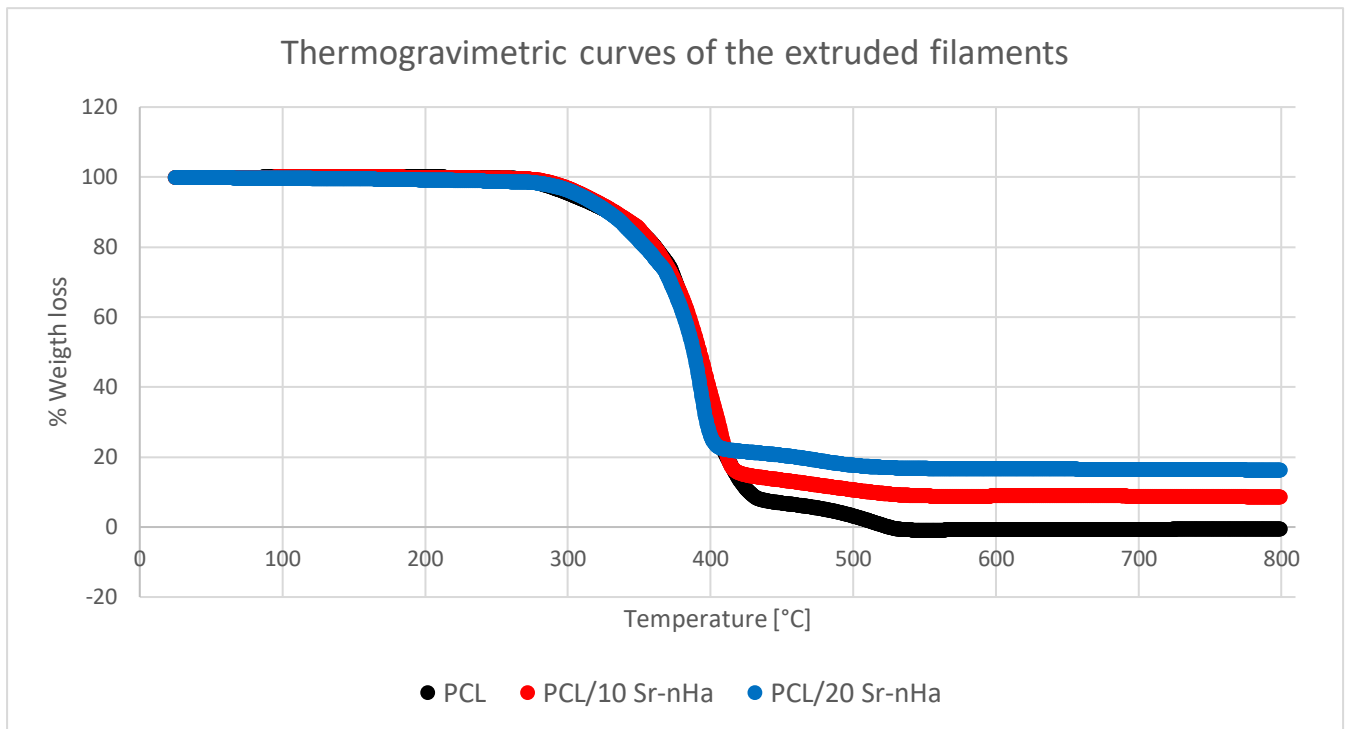


Figure 4.3 TGA analysis of a representative sample of each extruded composition PCL (black), PCL/10Sr-nHa (red) and PCL/20Sr-nHa (blue)

The % ceramic residue calculated as the average of three sample is reported in Figure 4.4. The results show that PCL/ SrHa 10% w/w presents an average residue of 8.75 +/- 0.94 % while the PCL/ SrHa 20% w/w of 17.3% +/- 3.45 % which are slightly lower than the designed materials.

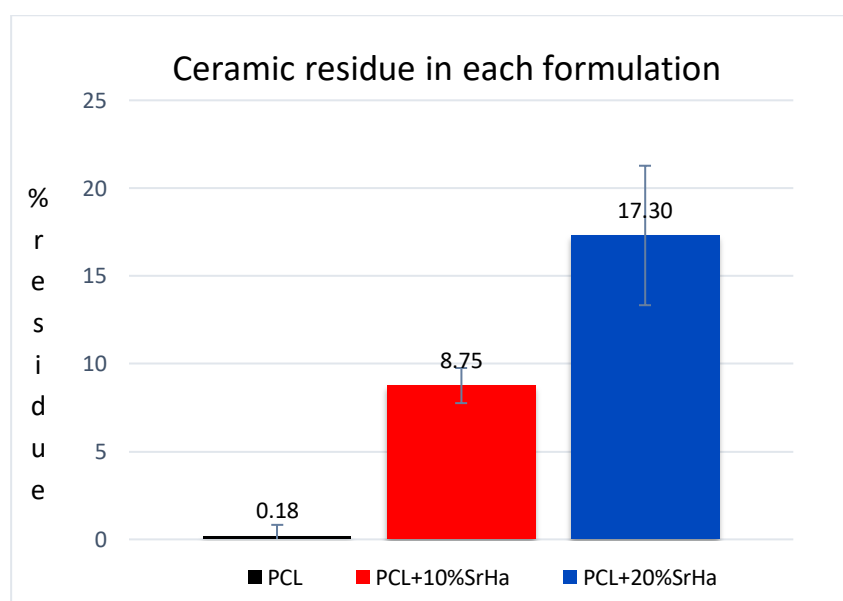


Figure 4.4 SrHa average % residue calculated in the TGA tes in PCL, PCL/10 Sr-nHa, PCL /20Sr-nHa samples

4.3 3D scaffold design and fabrication

The scaffold's design obtained by Solidworks software, used as a model for the 3D printing is presented in Figure 4.5, where the overall structure as well as the cross section of both designed scaffolds (the Tri-layered PCL/Sr-nHa (Figure 4.5. a,c) and the bare PCL control (Figure 4.5 b,d) are illustrated.

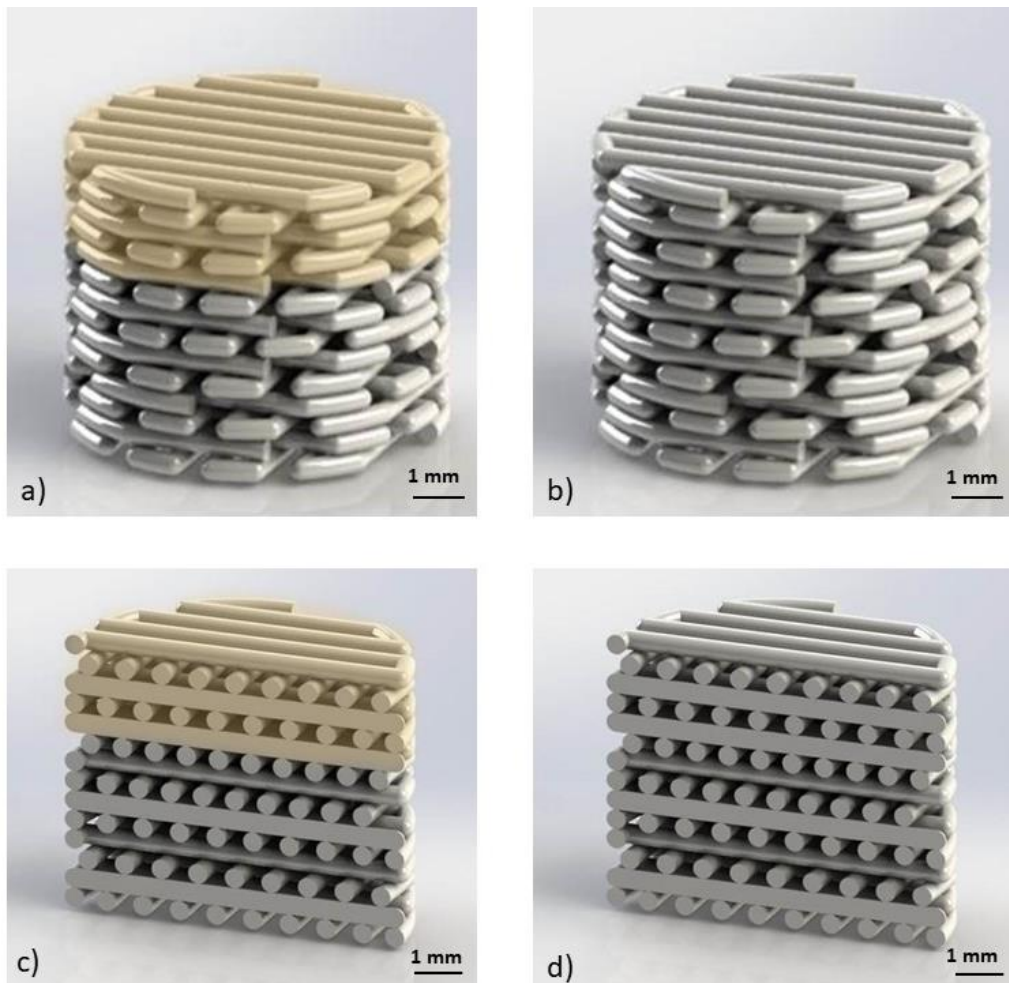


Figure 4.5 CAD images obtained by Solidworks software show the design and the cross section of the Trilayered scaffold (a,c). The upper part(yellow) is made of PCL/10 Sr-nHa samples while the bottom(grey) consists of PCL /20Sr-nHa samples formulation and the PCL control scaffold (b,d)

Before the printing of the multilayer-structured scaffold, the optimization of the printing parameters and the printing procedure relative to the different formulations was carried out. In Figure 4.6.a it is shown a frequent problem, especially observed during the printing of the PCL/Sr-nHa formulation, regarding the leak of air from the needle of the syringe, due

to an incomplete or inhomogeneous material's melting. The problem was solved by sieving the powder in order to reduce the SrHa particles agglomerates' dimension, and also by introducing the material necessary for every printing little by little, in order obtain a complete fusion of the materials before the extrusion. In Figure 4.6.b printed porous scaffolds made of the three different materials (PCL, PCL/10 Sr-nHa PCL/20 Sr-nHa) are presented, showing the reach of the aim to achieve a good level of printability for all of the formulations. Similar scaffolds were printed for the further cell work carried out in this study.

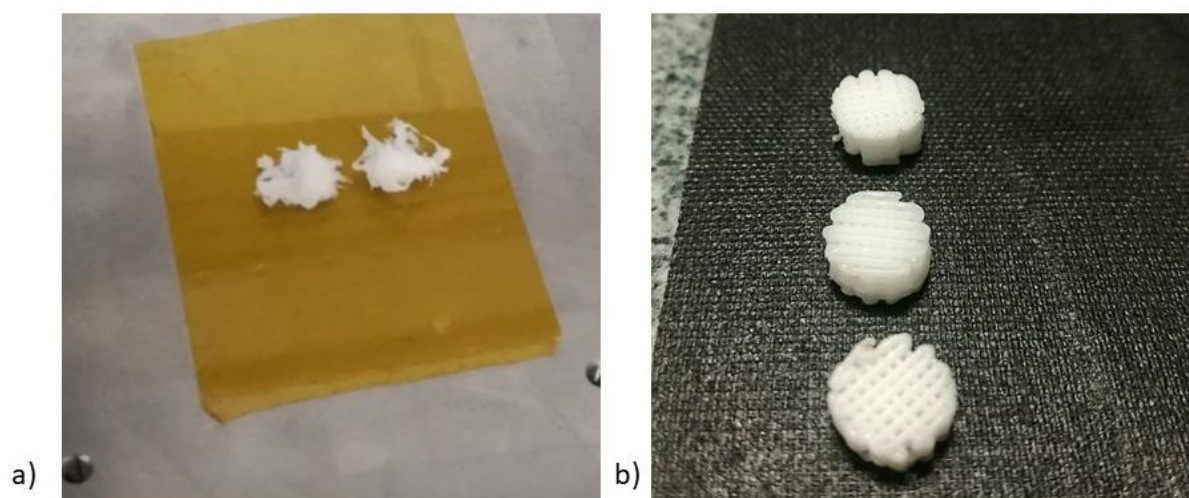


Figure 4.6 3D printed scaffolds: a) non-optimal vs b) optimal printing conditions

The 3D printed achieved scaffolds with the designed geometry are presented in Figure 4.7.b. The obtained morphology is the result of the optimization 3DP process aimed to achieve a good printability of the extruded materials, allowing the fabrication of continuous structures with high-level reproducibility over the structure's design and continuity between compartments. In Figure 4.7.a it is shown an effort in Trilayer scaffolds' fabrication, before the reach of the goal to set the proper calibration parameters, by the EnvisionTec Bioplotter software, necessary to direct the printing of the second material precisely on the top surface of the previous one, allowing to obtain a perfect match between the cylindrical geometry of the two printed parts. In the final structure it is visually possible to distinguish the stratified architecture since the denser material, (PCL/20 Sr-nHa) results wither than the PCL/10 Sr-nHa, due to the higher ceramic content into its composition.

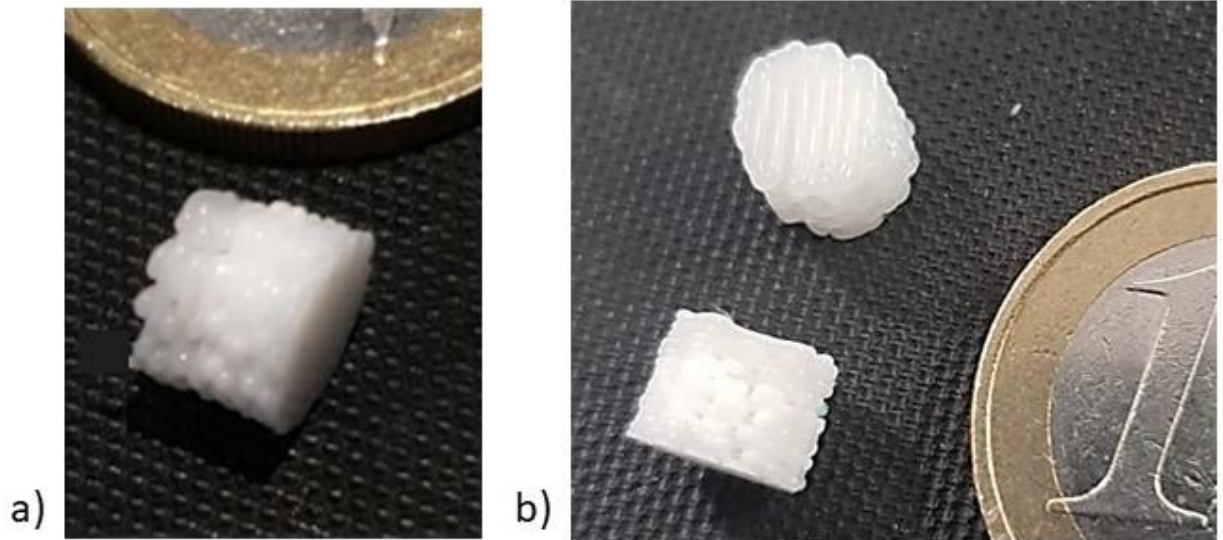


Figure 4.7 a) Trilayered scaffold that does not provide continuity between compartments b) Achieved PCL and Trilayered PCL/SrHa scaffolds showing good match with the designed morphology

4.4 Characterization of extruded surfaces

4.4.1 Contact angle analysis of printed materials

The wettability of the three materials was investigated by the contact angle measurement on flat surfaces. Figure 4.8 shows the results of the test conducted on five samples for each composition. It appears that the presence of the SrHa particles tends to increase the contact angle of the extruded surfaces. Specifically, the contact angle measured for the PCL samples was in average 72 degrees while the PCL/10Sr-nHa and the PCL/10Sr-nHa show measure of $82,5 \pm 0.69$ and $90,81 \pm 1.24$ degrees respectively.

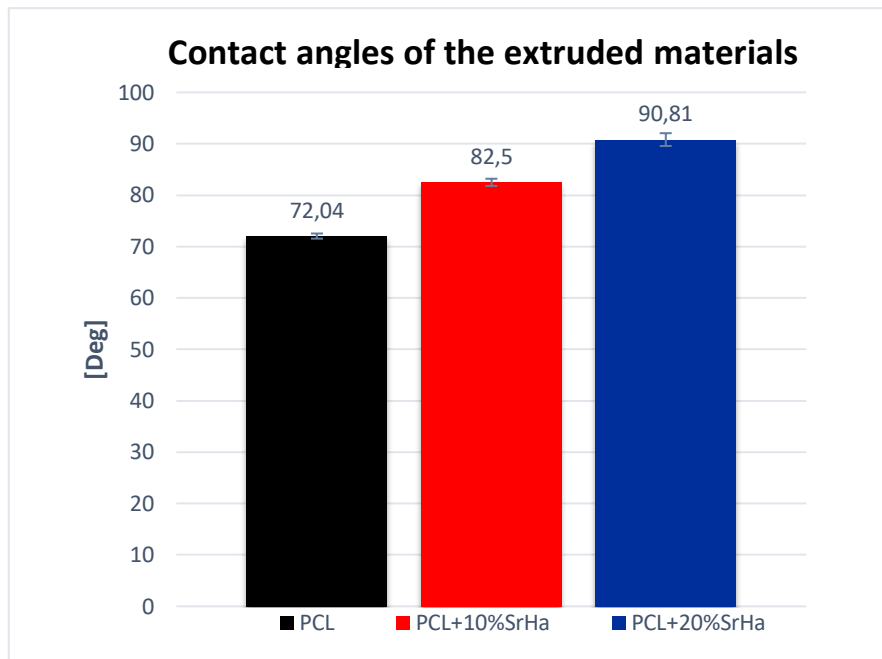


Figure 4.8 Contact angle measurement of the three printed formulations extruded PCL, PCL/10 Sr-nHa, PCL /20Sr-nHa

4.4.2 SEM analysis

The surfaces' topology and scaffold's morphology were investigated by Scanning Electron Microscopy (SEM). In Figure 4.9, the scaffolds are investigated at different level of magnification. From SEM images, the real strands' dimension has been calculated in order to check if the measure matched the theoretical geometry set during the design of the scaffold. For all the samples (PCL, PCL/10 Sr-nHa, PCL /20Sr-nHa) the measure appeared to be consistent with the theoretical value of the strand's diameter (0.42 mm). The macropore size was about 200 μm , resulting from the spacing between the strands., which is a functional value for cells infiltration and new tissues growth. Additionally, the pure PCL scaffold presents a smoother surface, compared to both the PCL/10 Sr-nHa, PCL /20Sr-nHa ones., where small caterers and irregular features are present onto the surface morphology.

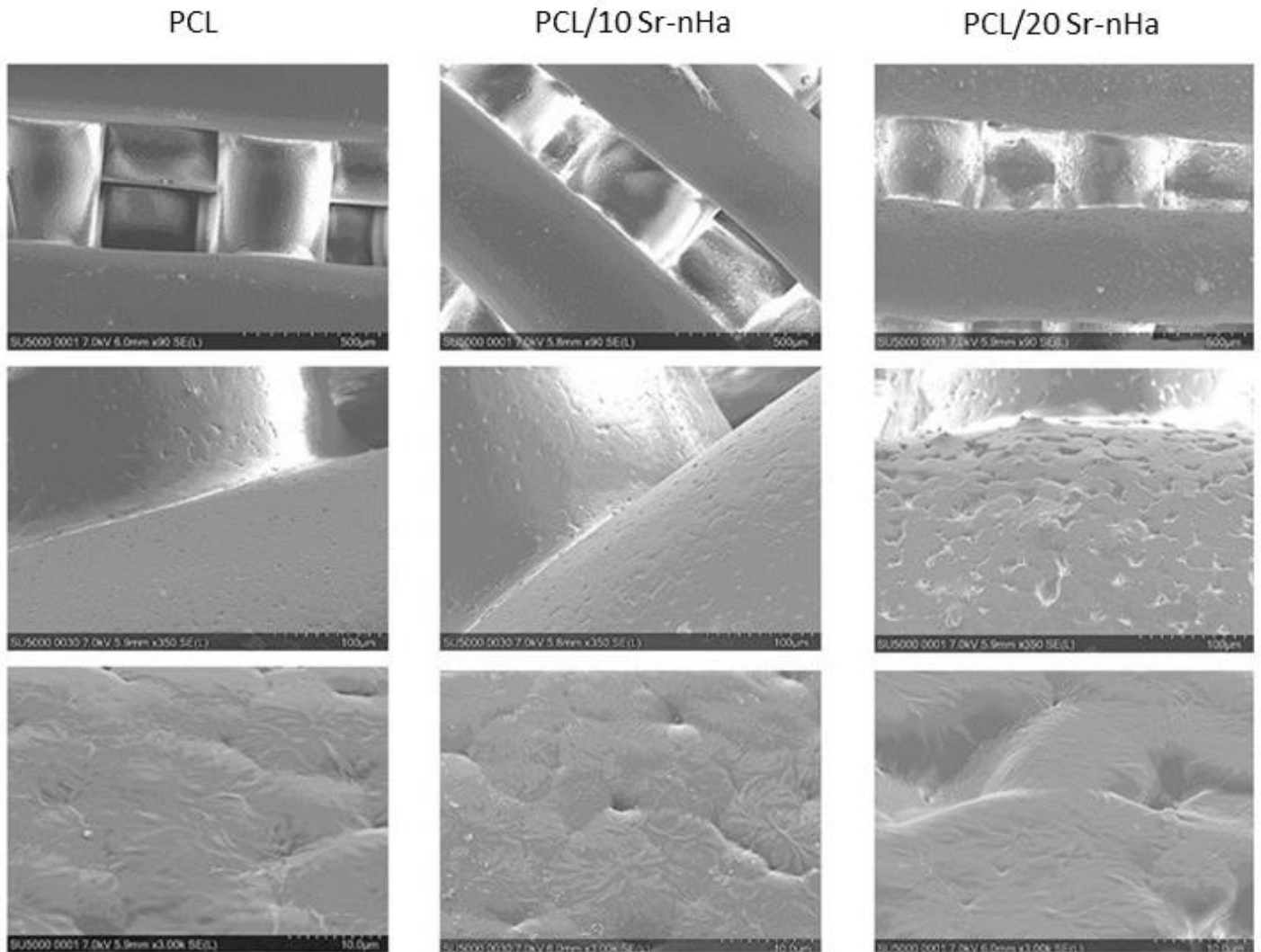


Figure 4.9 Characterization of the scaffold's surfaces at different magnifications (A.500 μm , B.100 μm and C.20 μm) obtained by SEM equipment (7kV 30A)

4.5 Characterization of scaffold's architecture

4.5.1 Micro CT analysis

The inner structure of the scaffolds was investigated using micro-CT technology. In Figure 4.10 the volume reconstructions of both the Trilayered PCL/SrHa scaffold and the bare PCL one are presented. The inner geometry of the scaffold's cross-section, investigated by cutting the scaffolds structure with a plane parallel to the cylinder's axes and

perpendicular to the strands' axis, is coherent with the scaffold design projected and the parameters of strands diameter and distance and are found to be reproducible and reliable for both the type of the scaffolds. The scans show the evident stratification of the two different composite phases. The bottom of the scaffold, made of a higher density material (PCL/20Sr-nHa), is characterized by a whither shade, while the top, made of PCL/10Sr-nHa is darker in the grey scale level, corresponding to the less absorption of the X-Ray beam from the material.

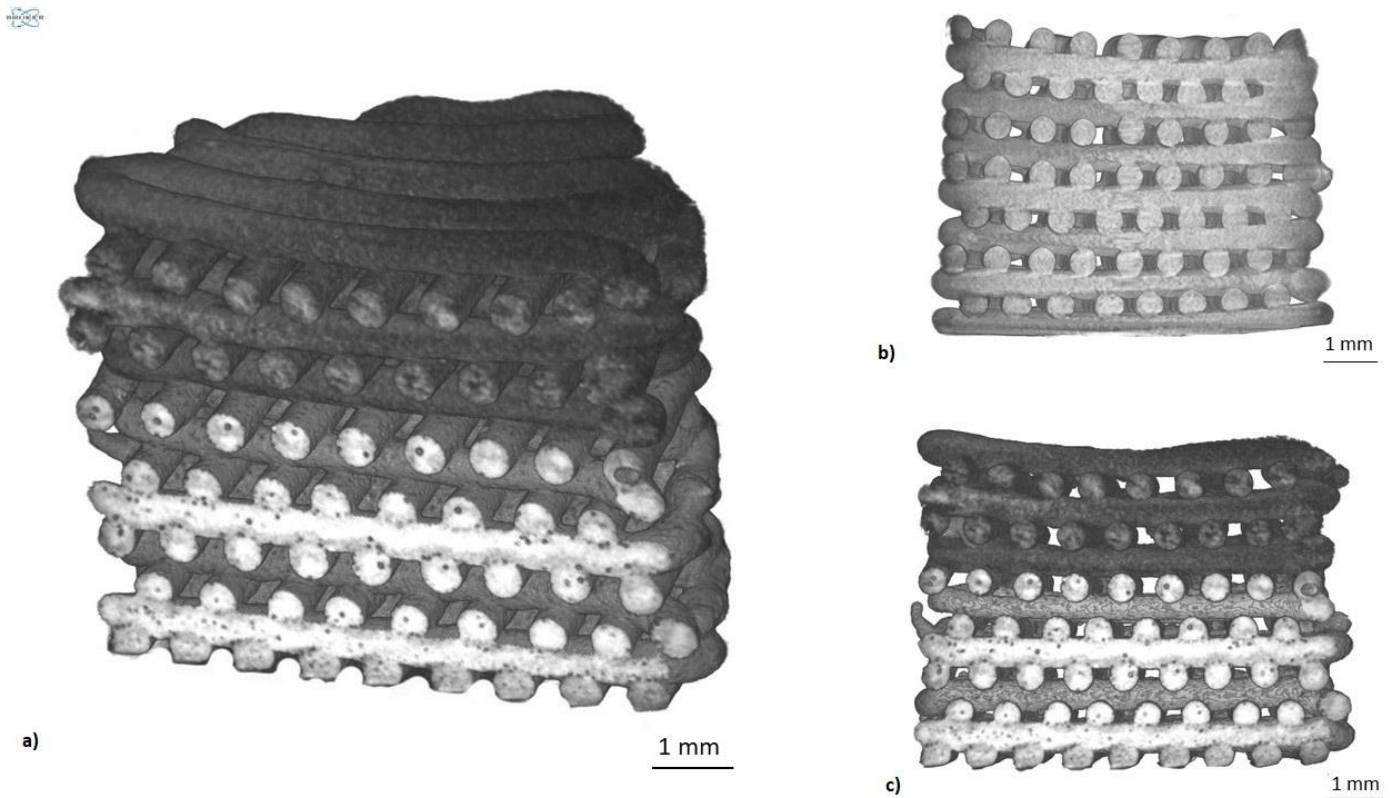


Figure 4.10 Micro CT reconstructions of the printed scaffolds a) c) Triilayer PCL/SrHa scaffold, b) PCL scaffold

Furthermore, the PCL scaffold shows a uniform colour due to the homogeneity of its composition. Similarly, the homogeneous colour for both composite formulations, indicating a uniform material density inside the sample's structure and good density distribution along the extruded filaments length. This allows to claim that the SrHa nanoparticles dispersion is uniformly distributed inside the sample's structure. However, in proximity of the strands' surfaces an enhanced radiopacity is noticed compared to the internal parts, resulting in the predominant presence of PCL in these regions. Finally, It is

evidenced the appearance into the PCL/20Sr-nHa composition portion of micro dimensional black spots, associated to the presence of air bubbles entrapped into the material during the extruding process.

4.5.2 Scaffold porosity

Porosity is expressed as the percentage of the void volume over the total volume in the engineered scaffolds. As the micro-CT images showed in the previous paragraph, the pore structure, consisting of connected channels merging adjacent cavities, results on the presence of fenestrations in the void walls in both samples is presented. The theoretical value was calculated by using the formula presented in Chapter 3 from the design parameters set for the scaffold project. In Table 1 the porosity characterization of the scaffolds is reported as average and standard deviation in terms of both open and close porosity of the Tri-layered Sr-nHa and PCL scaffolds. The theoretical porosity calculation obtained from the parameters set during the scaffold’s design process is also presented as a control over the porosity measurement and the manufacturing process’s reliability.

Table 4.1 Open and close porosity of the scaffolds

	Theoretical %	Open porosity %	Close Porosity %
PCL scaffolds	38.4	37.36 +/- 0.99	0.31 +/- 0.12
Trilayer PCL/SrHa scaffolds		39.02 +/- 0.51	1.04 +/- 0.26

4.6 Characterization of the mechanical properties of the 3D printed scaffolds

The mechanical compressive properties of the PCL/SrHa scaffold was tested and compared to those of PCL samples, taken as a control over the measurement. In Figure 4.11 the Stress-Strain curves of five samples for each type are shown. All the specimens ended the test within the first end condition set: the reaching of 490 N of solicitation over the surfaces, while the second condition of reaching a 50 % of strain was never achieved. The curves

present a similar behaviour for all the samples of the same type of scaffold when compressed evidencing the reliability of the test.

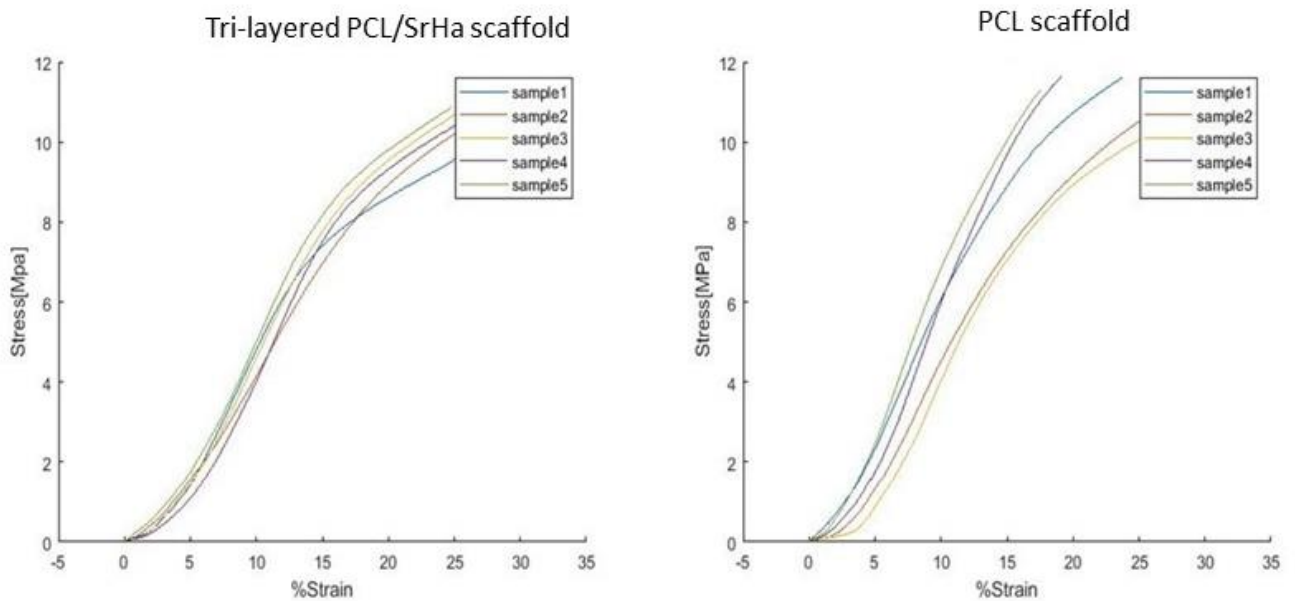


Figure 4.11 Stress-Strain curves of the two different type of scaffolds (PCL controls and Tri-layered PCL/ SrHa) obtained from compressive test.

The trend of the curves presents two different steps: an initial elastic phase in which the stress/strain ratio could be approximate to be linear (between 0 to 15 % strain) followed by a plastic region that shows a flexible plastic behave of both the materials. In the linear elastic region, the stress is assumed proportional to the strain, obeys the general Hooke 's law, the slope is Young's Modulus and the deformations are considered elastic and reversible. The end of this stage is defined by a point (Yield Strength) and represents the start of plastic irreversible deformations (175).

The stiffness of the scaffolds, assumed linear in the first part of the graph, was evaluated calculating the Elastic modulus of each curve as the ratio between the stress and the strain selecting two point of the most linear part of the function. Approximately the values were chosen for each sample in a range between 1 to 6 % of strain. In Figure 4.12 the average of the calculated measure of the Elastic modulus is presented. The PCL/SrHa scaffold's Elastic Modulus was found to be 56 ± 7 MPa while the PCL one was 49 ± 5 MPa. The results show that the presence of the ceramic component into the PCL matrix does not statistically

influence the stiffness of the structured scaffold. The Yield Strength, that marks the transition from the elastic to the plastic region, is more evident on the PCL/Sr-nHA scaffolds' graphs, as a clear change in terms of the slope of the curves, and it occurs at a lower value of stress compared to the PCL controls. The samples conditions at the end of the test show that the PCL scaffolds generally achieved a higher value of stress and associated to a minor deformation, suggesting a better ductile behaviour associated to the Trilayered-scaffold.

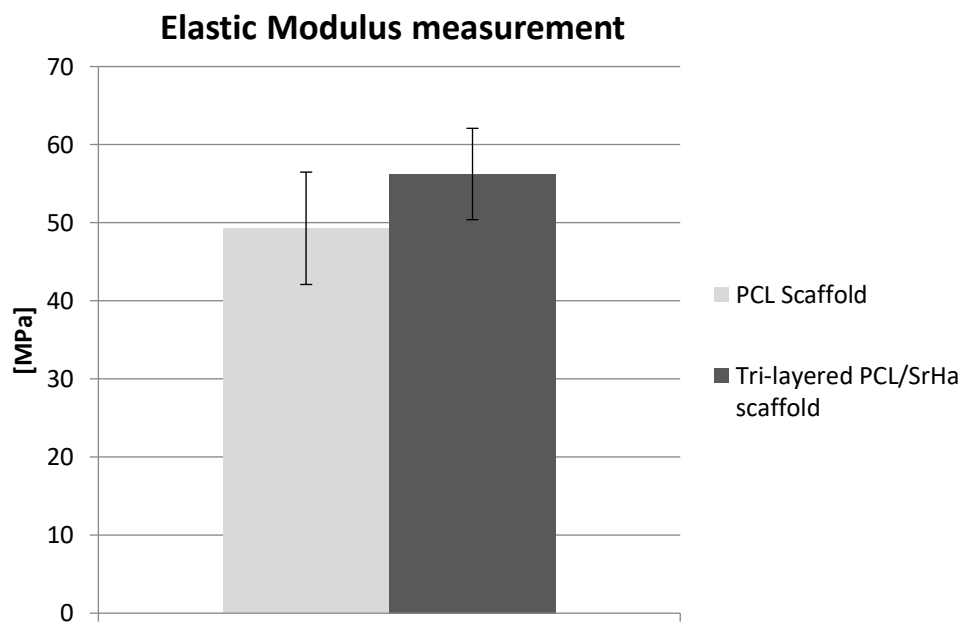


Figure 4.12 Elastic Modulus of the two different types of scaffolds PCL/Trilayered PCL/SrHa scaffolds.

4.7 Cell viability

4.7.1 Cell metabolism: MTT assay

The results of the MTT tetrazolium salt colorimetric assay are shown in Figure 4.13 The absorbance measured at 562 nm in each test is taken as an index of cytotoxicity level. Furthermore, it gives an indirect information about of the cell's count since the reduction of the salt is catalysed by an enzyme that is produced by live cells. The absorbance measured presents an increased trend after 3 and 7 days, evidencing a progressive increase of the U2OS cells' metabolic activity during the two timesteps. It is noticed that the values

obtained at day 7 are in average almost double of the values obtained at day 1. Since the salt formation of the Abcam kit used is assumed to be directly proportional to the number of the viable cells it is reasonable to claim that in this study, cells approximately redoubled their number after one week of seeding. (160) (176) During the procedure it was also noticed that after 7 days the formazan production, visible from the purple crystals formation, was not only enhanced but also better distribute inside the scaffolds' inner structure compared to day 1 and 3.

The comparison between the three materials evidences that at day 1 and 7 there are no differences in terms of metabolic activity within the groups while at day 3 PCL/20 Sr-nHa scaffold present a statistically significant enhancement compared to the PCL control.

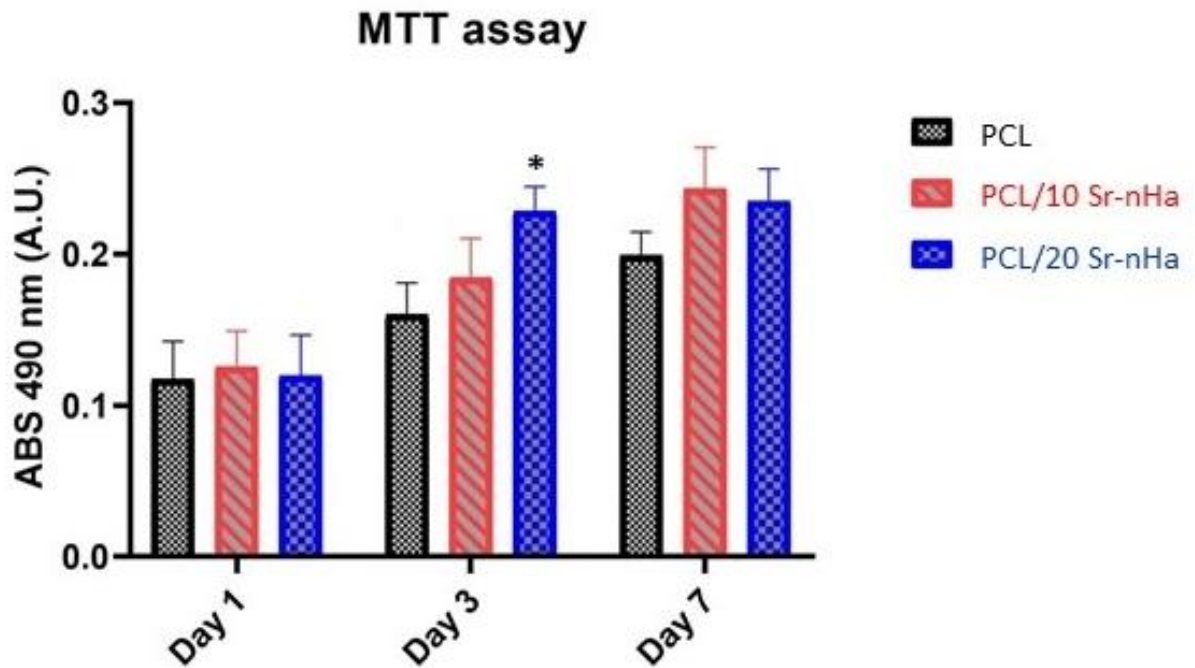


Figure 4.13 Absorbance measured at 490 nm in the three compositions at three different timesteps Data are presented as mean \pm standard deviation. $n = 3$ for each group, $*p < 0.05$.

4.7.2 Cell attachment: DAPI assay

The DAPI assay was used to provide qualitative analysis of cells' attachment on the scaffolds' surfaces. In Figure 4.14 the comparison of the three compositions at the two different time points is shown. The autofluorescence of the PCL in the same range of the

DAPI's fluorescence tends to influence the nuclei visualization, however it is possible to distinguish cells' nuclei and their dispersion over the surfaces of the strands. It appears that at day 7 the number of cells attached on all the substrates is visually higher than at day 3.

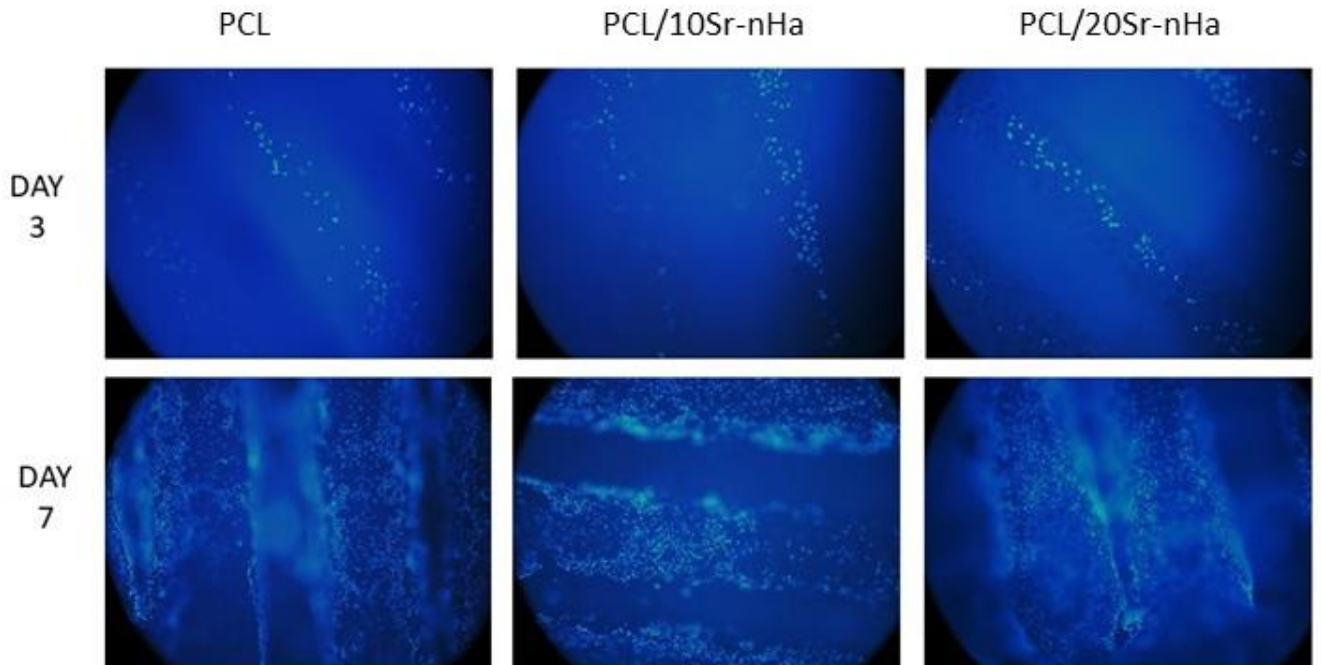


Figure 4.14 DAPI fluorescence at 360 nm captured with a Nikon 80i at 10X magnification

The proliferative activity, shown at day 7, evidences a simultaneous cells migration inside the scaffolds' porosity. In fact, comparing to day 3, in which cells are found to be especially attached on the top surfaces of the scaffolds, after one week of culture, it is possible to see a large number of cells scattered on the surfaces of the strands below. In Figure 4.15, images taken after 7 days of seeding with a magnification of 20X are presented while in Figure 4.16 the same scaffolds are shown using a lower magnification (10X). Because of the deepness of the scaffolds and the cylindrical shape of the strands it was difficult, with this equipment, the obtainment of images in which the cells attached on the first layer's surface as well as the cells attached on the deeper ones were focused. For this reason, in both of the figures, images taken at different depths are illustrated, representing a multiple view of the same strands of the tested scaffolds with progressive focus inside the depth of the

geometry. The adhesion seems to be overall uniform along the strand's cylindrical shape, slightly concentrated in the intersection area between two orthogonal strands.

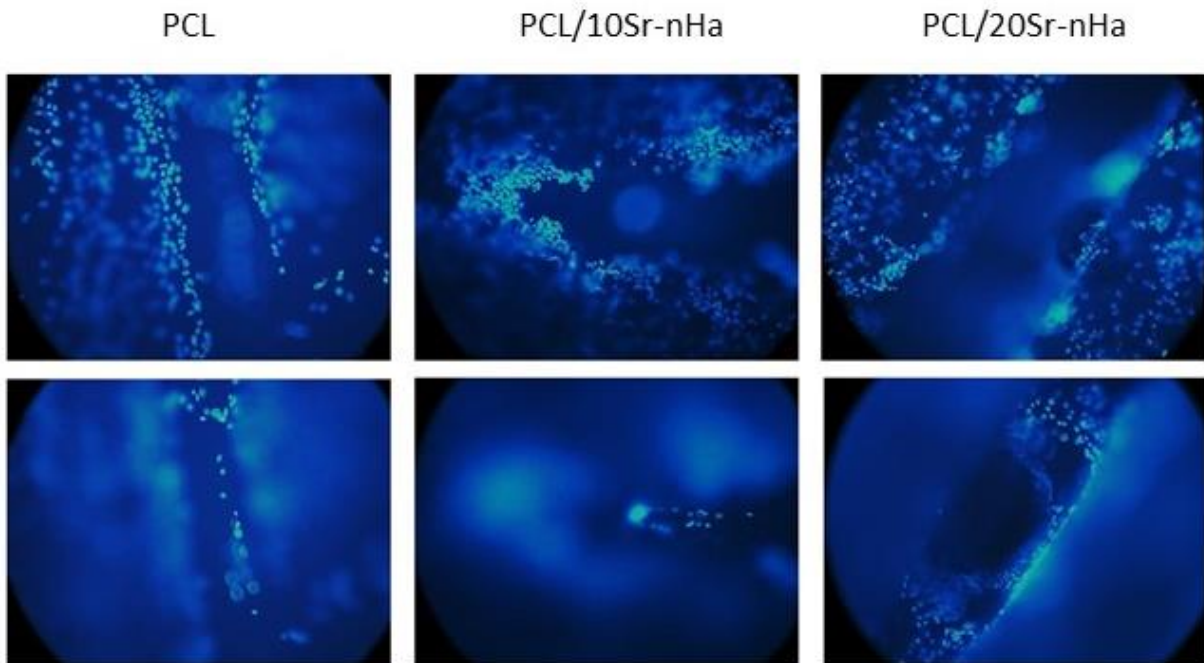


Figure 4.15 DAPI fluorescence at 390 nm captured with a Nikon 80i at 20X magnification

Furthermore, the examination provides a qualitative comparison between the three materials. It is noticed that the PCL/10 Sr-nHa and PCL/20 Sr-nHa present an higher level of DAPI fluorescence and an higher number of cells' nuclei are shown compared to the PCL control scaffold at both the magnifications. Moreover, cells' spreading seems to be more

uniform on the PCL scaffold than the others, that present a more clustered distribution of nuclei along the strands' surface .

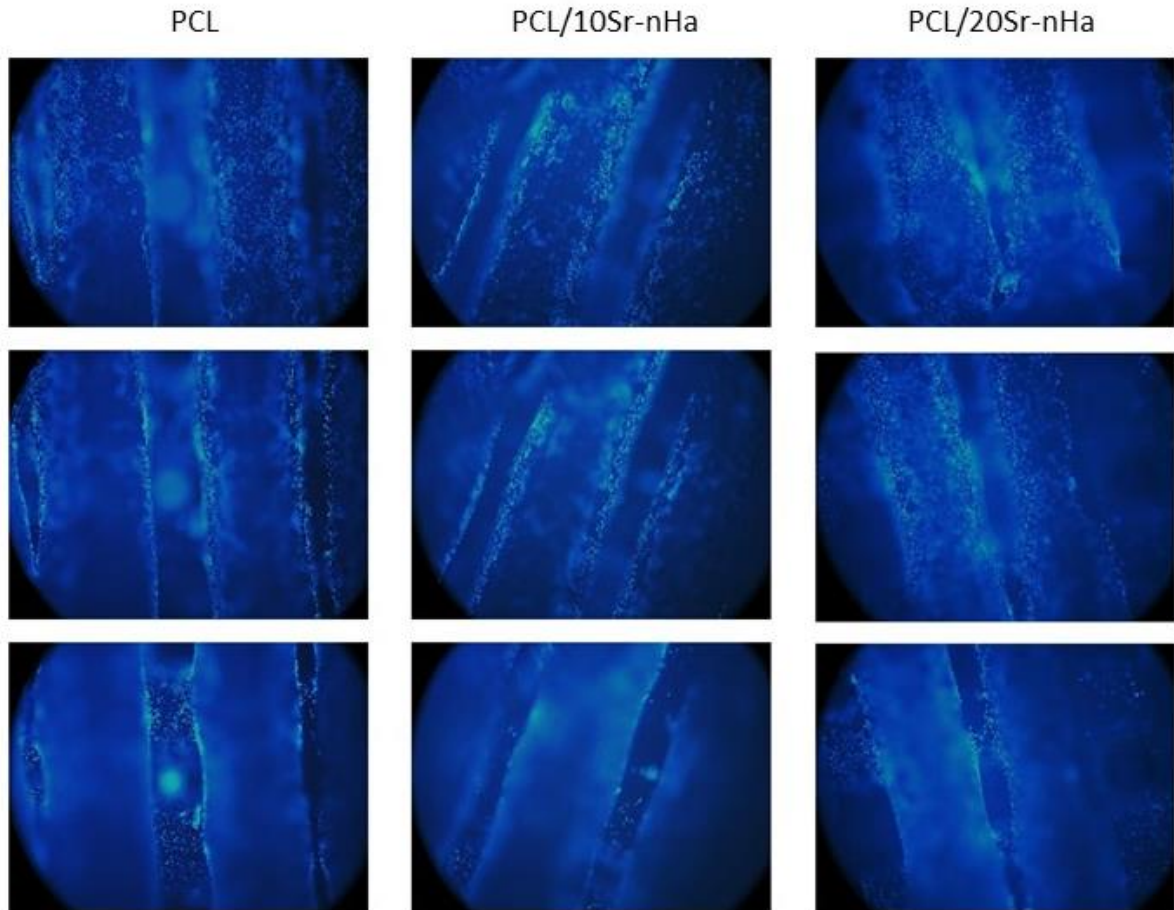


Figure 4.16 DAPI fluorescence at 390 nm captured with a Nikon 80i at 10X magnification

4.8 Cell adhesion and morphology

The images, obtained by SEM images, reported in Figure 4.17 show the presence of cells fixed on the top surfaces of the scaffolds after 14 days of culture.

In the lower resolution images (Figure 4.17 a) the strands' shape of the scaffold and their crossed pattern is evident as well as the cells' distribution allowing their visualization of also attached on the deeper layers of the scaffolds. The middle-resolution images (Figure

4.17 b) enable to distinguish the cells body's' shape over the scaffolds' surfaces. The attachment seems to be more clustered with a larger number of cells on the composite PCL/10Sr-nHa and even more on the PCL/20 Sr-nHa scaffolds compared to the PCL control one. In fact, in this scaffold the single cell is more recognizable and more separated from the adjoining ones while in the others it is more difficult to identify the single structure because they tend to grow one close to another, spreading to form a uniform layer (177). The higher resolution images (Figure 4.17 c) intend to isolate localized cells on the scaffolds' surfaces. The attachment presented in the PCL/10 Sr-nHa and PCL/20 Sr-nHa scaffolds seems to stimulate cell spreading and filopodia formation while, on the other hand, cells cultured on the PCL scaffold present a rounder shape and the filopodia are almost undiscernible.

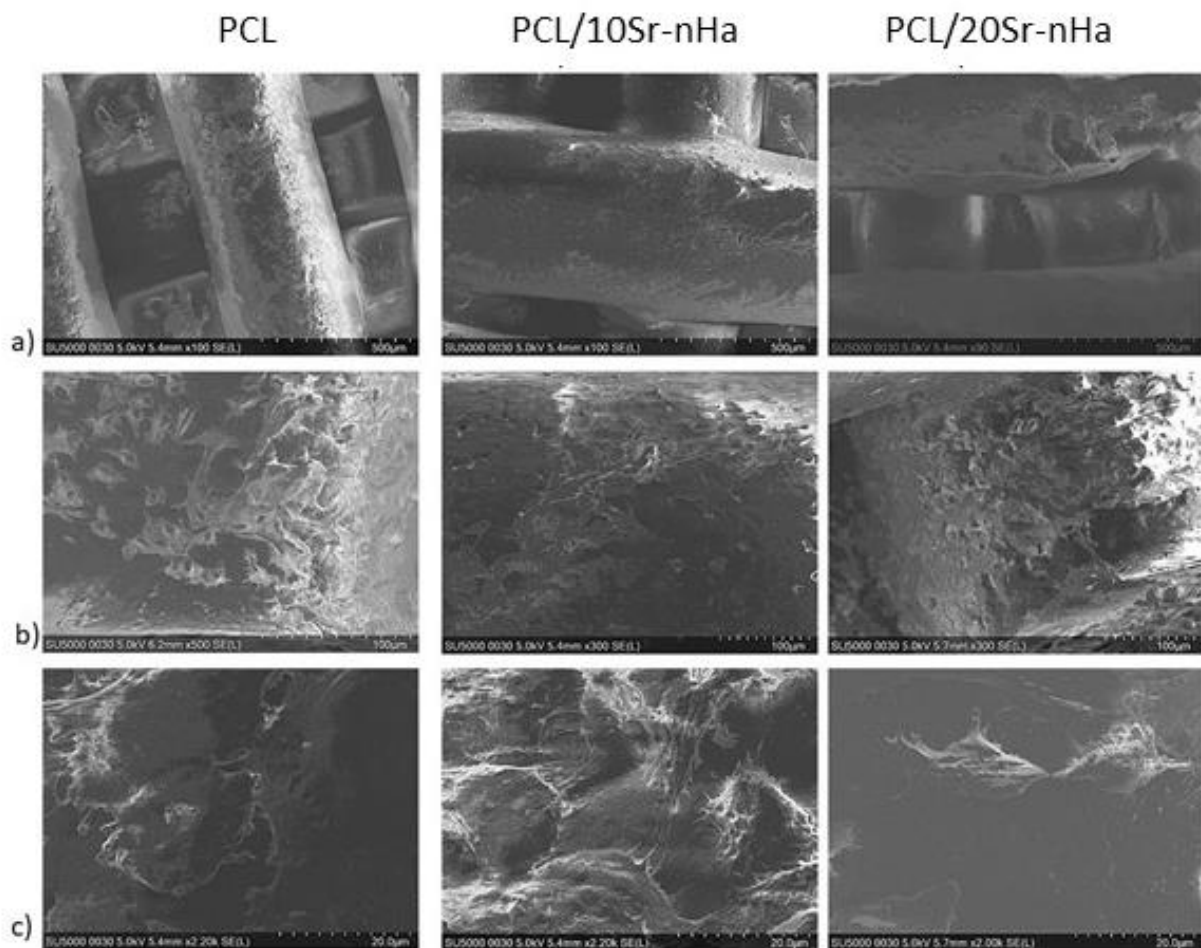


Figure 4.17 SEM images of the fixed cells on the seeded scaffolds at different resolutions a) 500 μm, b) 100 μm c) 20 μm

4.9 Osteogenic potential

In Figure 4.18 the standard 9 points calibration curve of the BCA assay (from 0 to 2000 $\mu\text{g/ml}$) and the 8 points standard dilution series curve (from 0 to 200 $\mu\text{g/ml}$) of the ALP assay, calculated with the best-fit method, are presented. These curves are used to quantify the total proteins concentration and the ALP enzyme presence.

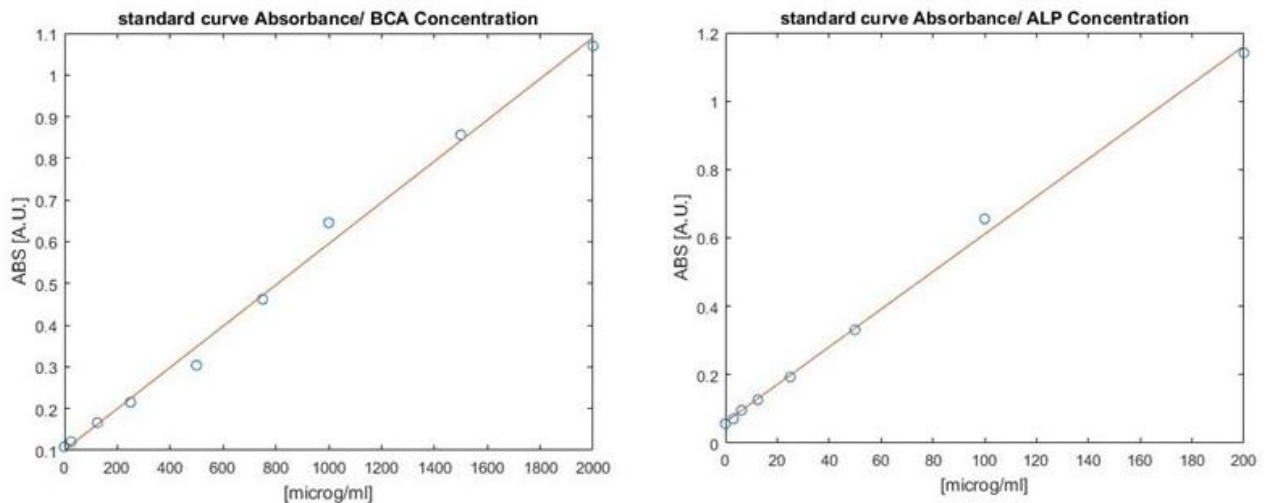


Figure 4.18 Standard calibration curves estimated for the BCA and ALP assays

The bar plots in Figure 4.19 shows the results of the assays, indicating the concentration quantified in each group in $\mu\text{g/ml}$. The BCA test evidences that during the first three weeks there is a progressive increase of the total proteins content while during the fourth week there isn't a significative increment in all the groups. The differences between the groups suggest a different metabolic activity induced by the three different materials. Statistically, the multi comparison tests show that the significance is consistent at 21 days for the PCL/10Sr-nHa and at 28 days for PCL/20Sr-nHa formulation. The ALP content first appears at day 14, increases up to day 21, and decreases thereafter in all the tested groups. The highest value of concentration reached at day 21 was found to be significant ($p < 0.05$) for both ceramic formulations (PCL/SrHa 10% w/w and PCL/SrHa 20% w/w) compared to the PCL control while in every other timesteps the difference between the groups are not found to be significantly different.

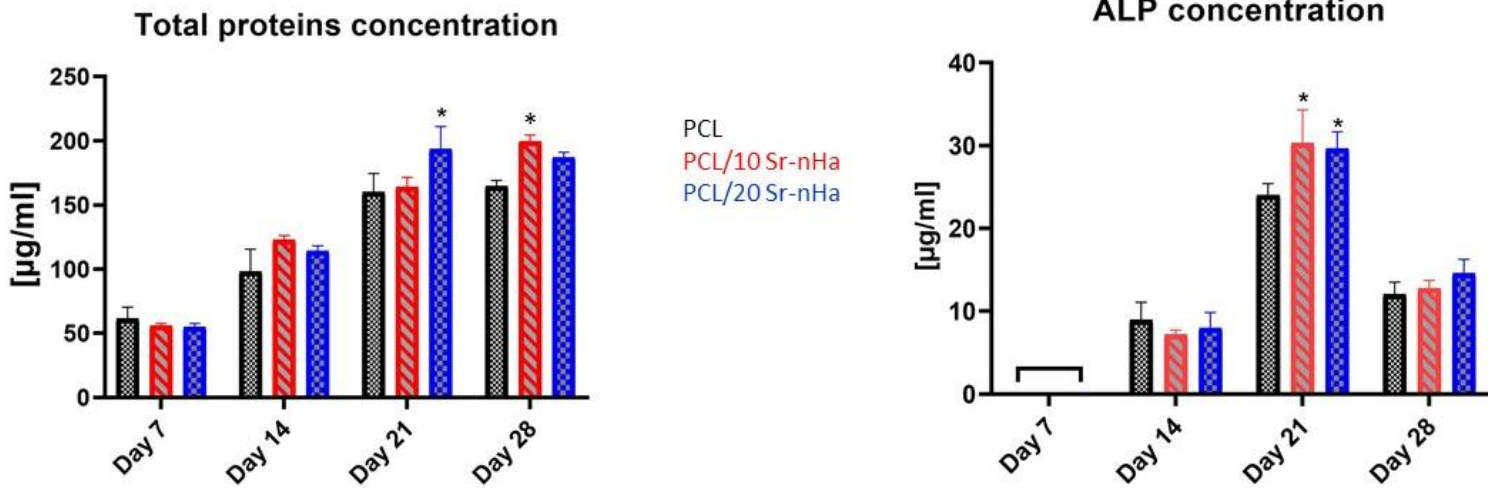


Figure 4.19 Total proteins and ALP concentrations measured by colorimetric assays
Data are presented as mean \pm standard deviation. $n = 6$ for each group, $*p < 0.05$.

In Figure 4.20 the percentage of ALP/total protein ratio is showed. This provides a measure of the ALP enzyme relative to the number of cells attached on every scaffold.

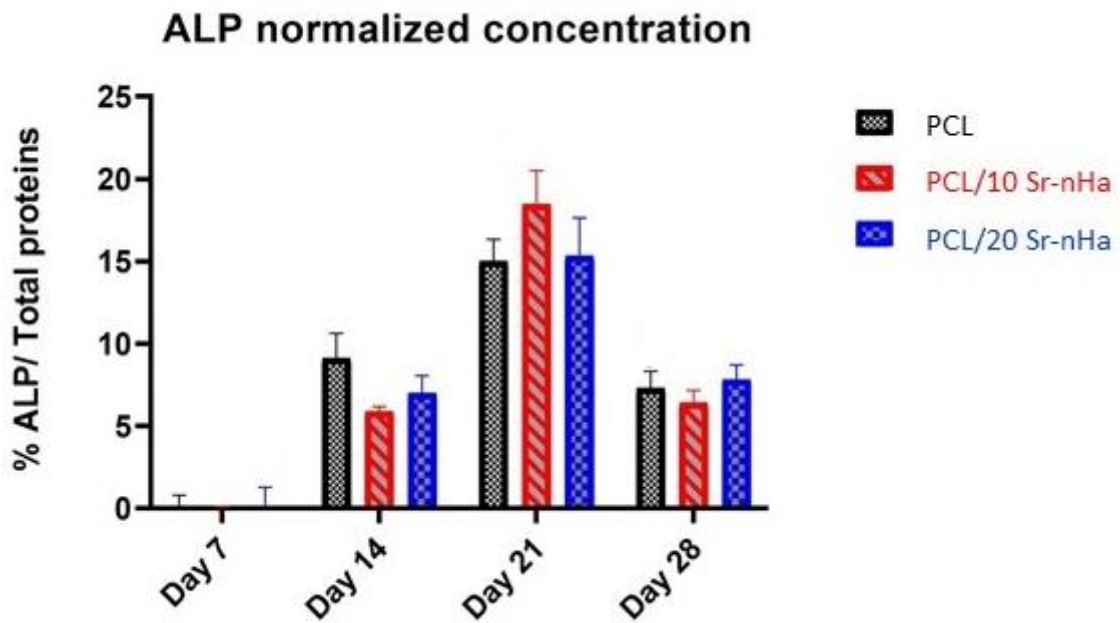


Figure 4.20 ALP/ total protein ratio
Data are presented as mean \pm standard deviation. $n = 6$ for each group, $*p < 0.05$.

The ALP/total protein ratio tended to increase between the 7th and the 21st day and to decrease at day 28th in all the groups. In this case was not found any significant difference

between the groups at the different time point evaluated. Therefore, evidencing that the enhanced ALP activity emerges with the simultaneous appearance of a higher number of proteins production in the composite scaffolds.

4.10 Mineralization potential

The Alizarin red assay, showing the presence of calcium deposits on the 3D scaffolds, enables to control the mineralization activity and localizes hydroxyapatite crystals formation. In Figure 4.21 qualitative images of the top treated surfaces at different timesteps are presented.

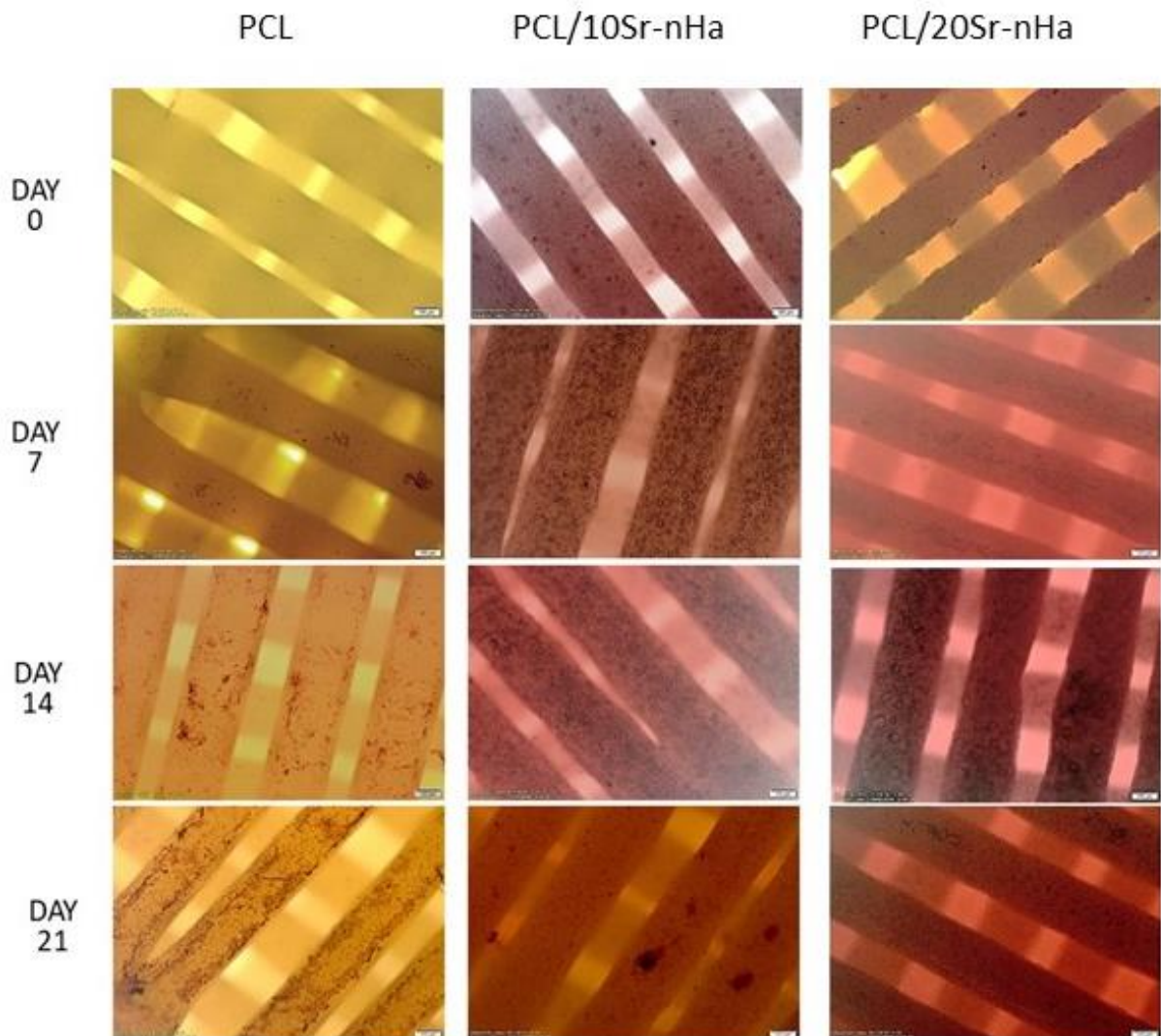


Figure 4.21 Alizarin red staining. Picture taken on the top layer of the scaffolds with inverted microscopy.

Day 0 represents a control over the test since it allows the visualization of the scaffold surface treated with the alizarin red staining without any cells seeded on the surface.

The mineralization of the scaffolds occurs in all the group since on all the sample surface appears the presence of calcium aggregates, linked to the new hydroxyapatite production promoted by the cells. According to Figure 20, scaffold mineralization is evident starting from Day 14 and maximised at Day 21, in which some big agglomerates of new inorganic calcium component are clearly visible.

Chapter 5: General discussions

5.1 Introduction

The main goal of this thesis was the design and optimisation of a 3D composite scaffold with a multi-layered architecture for OC tissue repair and regeneration. To overcome the current challenges for the treatments of OC diseases and develop a new cost-effective and patient specific strategy a 3D Bioplotter was used to print a multimaterial PCL/Sr-nHa-based scaffold to achieve a porous tissue-like structure with stratified design and tailorable properties in each layer, thus promoting targeted regenerative processes and providing a good stability at the interface between the cartilage and the bone-like tissue compartments.

Specifically, the study aimed to the achievement of five consequential objectives focused on: 1) the optimization of the biomaterial formulations toward the scaffold fabrication, 2) the optimization of the printing parameters for each material formulation, 3) the feasibility of the manufacturing of the 3D scaffold with a tailored design and a multi-layered composition, 4) the evaluation of the resulting 3D scaffold performance in terms of physico-chemical and mechanical properties, 5) the assessment of the biocompatibility and the biological performances of the scaffold.

5.2 Scaffold design and production

Following on the analysis of the main challenges in OC tissue regeneration, mainly related to the concurrent repair of bone and cartilage, AM techniques have emerged as promising new options for the development of strategies intended for heterogeneous tissues, such as the OC unit. In this study, PCL was chosen as main component of the printed scaffold for its good biocompatibility, printability, processability and physico-chemical stability (89) (178). To enhance the bioactivity of the 3D-printed, polymer-based scaffolds, the polymeric phase was combined with mineral deposits of Sr-nHa (179). Ha is a ceramic material widely used in bone TE, since it is bioactive, induces osteoconductivity, and it represents the main inorganic constituent part (85% of the dry weight) of bone tissue(23). Also, the addition of HA into a polymeric matrix, provides an enhancement on mechanical structure's stability (99). The Strontium substitution, into the Ha lattice, has been clinically tested to have a

favourable effect on bone turnover, promoting osteblastogenesis and inhibiting osteoclasts differentiation by targeting specific Ca²⁺-sensitive metabolic pathways (100) (101) (94) (102) (103). Also, it was found that the presence of the Sr-Ha has benefits on cartilage reconstruction inducing collagen type I synthesis, revealing as a promising material for the treatment of OC diseases. For this reason, it has been chosen in this work, as ceramic constituent part in the multilayered printed scaffold (97). Moreover, since the ECM features of natural OC tissue are nanometric in dimension, the use of the Sr-nHa to produce nanocomposite constructs was preferred for this work in order to stimulate cells growth and guide tissue regeneration, providing an enhanced biomimetic environment (10) (93). The content of the ceramic phase was chosen to decrease along the structure going from the bottom (subchondral bone layer, made of PCL/Sr-nHa 20% w/w) to the top (cartilaginous layer, made of PCL/ Sr-nHa; 10% w/w), which needs less stiffness and mineral deposits content for its regeneration. The scaffold's design was chosen to achieve a functional match between mechanical and biological properties, since the size, distribution and interconnection of the pores are considered important to guarantee cells migration, exchange of nutrients and metabolites and allow new bone tissue vascularization (127). Therefore, the designed parameters of the scaffold shown in Table 3.1 were chosen in order to satisfy different criteria. The ideal porosity of the scaffold is coherent with the porosity of the native tissues and OC grafting scaffolds recently developed in literature (67) (180). The macropore size, resulting from the spacing between the strands, was about 200 µm in dimension, which is a functional value for cells infiltration and new tissues growth. In fact, the ideal pore size in OC tissue regeneration seems to be approximately between 100 µm to 1200 µm. (181) (67). The strands' design and the inner pattern of the scaffold were found to guarantee high reproducible mechanical properties, compatible with the mechanical stiffness of the OC unit, allowing to structurally sustain OC tissue repair under biological load conditions (7) (182) (183) (184). Recent studies developed insights in the matters of the design and geometry of porous scaffolds for the best reproduction of the OC unit. The effects of the strands' distance and dimension, layers' orientation, and porosity distribution, on the mechanical and biological behaviour was investigated and the geometry with the shifted and perpendicularly oriented strands was found to guarantee a good matches and reproducible performances (7). The reduction of the strand's distance dimension in a selected part of the subchondral bone layer was finally aimed to mimic the

physiological calcified cartilage's thickness (1.5-2 mm) ,as interface between OC compartments, reproducing its harder mechanical properties; additionally acting on the biomimeticity of the OC tissue-like structure (185). The printing optimization process showed the achievement of good results for all the materials extruded allowing the production of a reproducible structure and further possibility to print multimaterial scaffolds. In Table 3.2 the printing optimized parameters of temperature, speed and pressure are presented. Further optimisation, both in terms of design and computational calibration was necessary to direct the printing of the second and third portion, and hence to allow the production of the multiphasic structure shown in Figure 4.7.

5.3 Chemical topographical and mechanical characterization of tri-layered printed PCL/ Sr-Ha scaffold

Scaffolds were printed according to the conditions presented in Table 3.2. At this stage, the realization of multi-material 3D printed structure (Figure 4.5) with computer-aided tailored design and high reproducibility was achieved. The nominal desired strand diameter (0.42 mm) as well as the uncompressed theoretical porosity of the scaffold, obtained from the parameters set in the scaffold 3D model, were compared with the geometrical measurement obtained by SEM images and μ -CT calculations, showing a good match between them (Table 4.1). As demonstrated, scaffolds were consistently printed with reasonable fidelity to the original CAD design, suggesting a good reliability of the extrusion printing process. The geometry and the porosity chosen were aimed to achieve a structure with good mechanical properties, also providing enough space for cell migration and proliferation. In literature, the correlation of the pore size and porosity on mechanical properties is strongly evidenced as well as its drastic influence on tissue ingrowth and cells migration (67). The calculation shows that the PCL scaffolds open porosity appears to be slightly lower (37.36 +/- 0.99%) while the Trilayer SrHa/PCL one slightly higher (39.02 +/- 0.51%) compared to the theoretical calculation (38.4%). The reason of this result might be related to the different printability of the materials and printing process's variables that seems to drastically influence strands' dimension (106). In a first analysis it was evidenced that the obtained values of porosity are coherent with the porosity of the native subchondral and cartilaginous tissues, allowing consideration about the potential

structural function of this structure in OC tissue regeneration (2). The measurement is found to be consistent with OC grafting scaffolds recently achieved (27-37% for cortical grafts, 40-50% for cartilaginous and trabecular tissues grafts (67) (180). Furthermore, different studies recently investigated the use AM for the achievement of OC tissue scaffolds with different pore size(107). In a recent research it was assessed a strict dependence between pore dimension and mechanical properties: small pore (0.2 mm) provide enhanced mechanical properties compared to the bigger and medium size ones (0.5, 0.9) in all the tested formulations(7). Additional analysis showed that the 3D manufacturing process does not induce significative chemical changes or thermal stability modifications in all the formulations printed (PCL, PCL/10Sr-nHa and PCL/20Sr-nHa). In fact, the comparison of the FTIR spectra (Figure 4.1, 4.2) of the materials' precursors powder with the extruded filaments' ones, showed the presence of the absorbance peaks, characteristic of the of blended formulations' in form of powder; while thermogravimetric curves (Figure 4.3) obtained from TGA analysis showed that within the range of the printing temperatures (130-140°) does not occur any material degradation. Moreover, the same tests evidenced that the ceramic n-SrHa dispersion into the PCL matrix does not chemically modify the polymeric structure after-processing and does not alter its thermal stability, since its degradation occurs in the same range of temperature for both blended formulations and bare PCL samples, which is approximately between 350 and 550 °C. From the FTIR spectra of the extruded material, it is also possible to notice that the ratio between the amplitude of the SrHa and PCL peaks is consistently lower than in powder conditions. This might suggest that during the printing process, in melted conditions, the PCL matrix tends to surround the SrHa nanoparticles. The morphological and topographical characterization of the scaffold's surfaces, revealed from SEM images analysis (Figure 4.6), support this phenomenon's evaluation. It is shown that the presence of the SrHa induces an enhancement of the surface roughness. The higher resolution images (Figure 4.8 C) show the presence of a large number of micro fractures, holes and surfaces imperfections in composite materials scaffolds, indicating that the SrHA particles have been successfully and homogeneously incorporated into the PCL bulks. The rougher surface, particularly observed in the PCL/20Sr-nHa samples, seems to be attribute to the contraction of the PCL chains during the cooling of the material, inducing the SrHa nanoparticles to remain incorporated into the PCL matrix, changing the surface's structure of the strands. The

enhanced roughness is connected to the results obtained from the contact angle analysis, in fact, it was observed that, the blended composite scaffolds, presenting an increased SrHa content and irregular surfaces were characterized by an enhanced contact angle measurement and consequently lower wettability. TGA analysis allowed the quantification of the ceramic content into the printed extrusions. The results show that for both the blended compositions, the amount of the percentage of SrHa over the weight was found to be slightly lower than the expected value (8.75 +/- 0.94 % for the PCL/10Sr-nHa and 17.3% +/- 3.45 % for the PCL/20Sr-nHa compositions). However, the ratio between the true value and the expected value appears to be consistent for both formulations (around 0.87). This means that, in average, the extruded filaments present a physical composition that contains an amount of ceramic particles 13% lower than the expected value. A similar behavior was achieved in other studies in which ceramic PCL-based scaffolds were tested (173). The tomographic reconstructions of the scaffolds' volume obtained by μ -CT (Figure 4.8) allow to obtain information about the materials distribution within the extruded filaments, architecture of the scaffolds, and hence inner porosity. Since the resolution of the equipment (3 μ m) results lower than nanoparticles dimension, it does not enable the SrHa localized visualization; however, both composite printed materials present a homogeneous density distribution inside the strands' cylindrical geometry, suggesting a uniform distribution of the ceramic phase into the polymeric matrix. Scaffold were also characterised in terms of mechanical properties through uniaxial compression tests. From the evaluation of the obtained stress/strain curves (Figure 4.9) of the tested scaffolds it can be concluded that the specimens of each group achieved a similar mechanical behaviour when tested in compression. This confirms that the 3D printing process is adequate to fabricate scaffolds with tailored design, and also reliable and consistent mechanical properties. The curves of the Tri-layered scaffolds show a more evident plastic region, evidenced from the reach of an enhanced deformation at the end of the test, suggesting a better ductile property, and better load absorption capacity during compression, associated to the introduction of the ceramic hydroxyapatite in the composite material (186). The Elastic Modulus calculation (Figure 4.10) in the elastic region of the curves was found to be 49 +/- 5 MPa for the PCL and 56 +/- 7 MPa for the Tri-layered scaffold calculated in this study. The result shows that both the measurements are found to be consistent with the rigidity of the native tissue as well as the stiffness values achieved in literature on

scaffolds with similar porosity (7). In fact, the range of the Elastic modulus, achieved in recent studies on scaffolds with similar composite materials, manufacturing technique and scaffolds design lies between 20 to 70 MPa (96,179,187,188), value compatible with both of the measurement of this study. The same studies also evidenced a strong relation between the % of the ceramic introduction into the scaffold's structure and the scaffold's stiffness starting from 20 % in weight ceramic/polymer and enhanced in the higher formulations, evidencing that the ceramic content tends to induce an enhancement on the mechanical rigidity of the scaffold. However, the measure shown in this study does not provide evidences of statistically differences between the two tested scaffolds. In fact to date, the reinforced mechanism of this phenomenon remains not well understood: for example in a recent study it was observed a reduction of the Young modulus in PCL/Ha scaffolds 10% w/w and an enhancement for the others compositions (111). In another study the reinforced phenomenon occurs for Ha-incorporated scaffolds but not in others ceramics such as TCP (179). Similarly, in another study no statistical differences in rigidity were found between PCL and PCL/ceramic scaffolds with multiple geometries (189)

5.4 In vitro response of U2OS cells cultured on PCL/Sr-nHa scaffold

The *in vitro* performance of the printed Tri-layered scaffold was assessed in terms of cell viability, cell attachment, osteogenic and mineralization potential of bone-like cells culture. The scaffold's design was found to be functional for cells' growth and proliferation, as it arises from the quantitative results of the MTT enzymatic assay (Figure 4.11), and the total proteins count obtained from the BCA assay (Figure 4.17). In these tests, an enhanced cell metabolic activity in all of the tested groups was observed since the first week of seeding. From the MTT results it is noticed that the values obtained at day 7 are in average almost double of the values obtained at day 1. Since the salt formation of the Abcam kit used is assumed to be directly proportional to the number of the viable cells it is reasonable to claim that in this study, cells approximately doubled their number after one week of seeding (160) (176). The qualitative images obtained with the DAPI cytofluorometric assay (Figure 4.12, 4.13, 4.14) showed a uniform cells' attachment on the strand's surfaces on all the sample types. Moreover, the enhanced proliferation of the first week is followed by the presence of cells into the scaffold's porosity, suggesting that the inner porous design

allowed cell migration into the sample's depth, leading cell growth into the internal 3D structure of the scaffold. Furthermore, the presence of the Sr-nHa into the scaffold's composition seems to influence cells' behaviour positively, confirming the Sr-nHa potential in promoting cell viability and cells' proliferation since an early stage of the process (190) (20). During *in vitro* tests cell-matrix attachment and spreading are two typical parameters observed to evaluate the goodness of the cell/substrate interaction. Images obtained by SEM microscopy (Figure 4.15) allowed the visualization of cells attached also on the deeper layers of the scaffolds, confirming the previous results. Cell attachment was evaluated from cell morphology in terms of cell spreading and enlargement on the scaffolds' surfaces, and length of the filopodia departing from their bodies (191). Cells attached on the composite scaffolds, especially the PCL/Sr20-nHa, were found to provide better adhesion with spread and irregular morphology; also, the presence of longer filaments compared to the rounder and more regular shape of the ones attached on PCL scaffolds was identified. The phenomenon is firstly ascribed to the composition of the samples, since it is proved that SrHa, influencing osteoblasts' Ca-dependent metabolic pathways and provides good stimuli to promote cell/substrate interaction. Furthermore, the roughness of the composite materials' surfaces, as derived from SEM analysis, could be identified as another reason determining the different cell/substrate interaction noticed in the images. In fact, rough surfaces are found to provide stable cell attachment and energetically favourable focal adhesions formation (4) (5)(192). Regarding the scaffold osteogenic potential, ALP assay was performed on the Trilayered scaffolds up to 28 days. ALP plays an important role in bone mineralisation and its expression is an indicator of type I collagen synthesis. ALP catalyses the hydrolysis of monophosphate esters (inorganic pyrophosphate) at high pH values, producing a local increase in the phosphates concentration, which together with calcium ions lead to the formation of hydroxyapatite crystals. (193) According to the results gained from the ALP assay (Figure 4.18), the osteogenic potential is detected from day 14, presenting a peak at day 21 and a decrease at day 28 with no significant differences within groups. In different studies it was found that the expression of the ALP in the later osteogenic stage evolves in the expression of other markers that promote tissue mineralization, such as osteopontin, osteonectin and osteocalcin (120). However, the process tends to strongly depend on the type of cells and the culture medium used for the study (122) (20). Finally, the mineralisation potential of the scaffold was assessed through

alizarin Red (3,4-Dihydroxy-9,10-dioxo-2-anthracenesulfonic acid sodium salt), which is a commonly used stain to identify calcium in tissue sections and cultured cells in vitro. Calcium forms an Alizarin Red S-calcium complex in a chelation process, and the product is characterized by the formation of a bright red stain (169). According to the qualitative results (Figure 4.19), the mineralisation potential arose at day 14 of seeding with the localization of calcium deposits on the scaffold's' surfaces, consistently with the ALP findings.

Chapter 6: Conclusions and future perspective

6.1 Conclusions

Osteochondral repair has become a growing topic of interest over the past few years in TE, followed by a crescent effort in the development of innovative and functional regenerative strategies. The initial study of mono- phasic solutions evolved in materials and design from a bulk cubic structure to porous and more complex architectures, such as bi-phasic, multiphasic and gradient-based. Recent developments in AM and 3DP techniques have shown promising results in the achievement of constructs with various design and composition for osteochondral TE, providing a high-level control over the scaffold's morphology and tailorable properties attribution in each layer. However, to date, these solutions are still largely limited to single gradients of either material or architecture, and surface's instability between layers, necessary to promote the simultaneous regeneration of the OC tissue compartments and simulate its inherent physical and mechanical characteristics.

In this study, PCL and PCL/Sr-nHA scaffold with a multi-layered architecture were fabricated via multimaterial 3DP technology. According to the experimental results can represent an innovative and functional strategy for the treatment of the OC unit diseases. The multi-layered architecture of the scaffold allows to simulate the complex hierarchical structure of the native OC tissue reproducing the physiological differences in composition, structure and mechanical properties of each compartments. Furthermore, this strategy enables to customise the properties each layer of the native OC tissue, promoting targeted regeneration process and providing a good interface stability between the cartilaginous and the bony phases. Specifically, the combination of polymeric and nanoceramic-based materials provided a good match to the physical, chemical and mechanical properties of both subchondral bone and cartilage. Also, the use of the Sr-nHa, as a widely accepted material for bone tissue regeneration due to its biocompatibility and osteoconductive functions, proved to positively impact on the mechanical and structural behaviour of the scaffold and at the same time to influence cell attachment and viability, as well as osteogenic and mineralization potential. The achievement of the seamless tri-phasic and biomimetic structure, obtained by using a single-step 3D manufacturing process may

represent a ground-breaking solution in TE, both from a manufacture and sustainable perspective, since reduce the cost and time of the production process as well as any waste related to it. Furthermore, it provides proof of concepts data in order to support further studies for the fabrication of custom and patient-specific structures, being based on the use of a CAD model that can be easily derived from MRI or CT scan data.

6.2 Future perspective

Further studies regarding the characterization of the physical properties of the printed scaffold might be addressed to assess the biodegradation rate of the structure and the long-term ion release, to quantify the bioactivity level achieved by the introduction of the Strontium ion into the scaffold composition. Furthermore, the investigation of the scaffold's mechanical behaviour after *in vitro* tests may evidence changes in the structural properties occurred after the implant's mineralization. In order further prove the osteogenic potential of the scaffold and complement the ALP assay and mineralization potential, PCR-based tests might be perused. Moreover, it would be interesting to evaluate the potential regenerative of the structure by conducting *in vivo* tests. It might be relevant to explore the level of new tissue promotion and eventual inflammatory reaction occurrence in the native tissue environment.

A possible development in order to enhance the developed scaffold performance, and hence further promote OC tissue repair and regeneration might be the incorporation of bioactive factors within 3D bioprinted implant. This promising strategy proposes the realization of constructs that can be used as a means to control the release of growth factors, promoting lineage-specific differentiation of stem cells, vascularization from the surrounding tissue, and enhanced healing. These implants might also likely include spatially defined patterns of cells, proteins and genetic material for the replacement of the damaged joint. Many recent studies showed good result in the matters of 3D printed cell-leaden hydrogels and cell encapsulation, promoting cell viability after scaffold's fabrication and allowing their proliferation and production of ECM products. Furthermore, the combination of culture systems with bioreactors and microfluidics with 3D interconnections has triggered alternative reporting great potential in joint resurfacing

applications. These systems are capable to resemble the native OC environment by the reproduction of multi-compartmentalized chambers with controlled gradients, allowing co-culture of chondrocytes and bone-like cells in spatially defined environments.

Bibliography

1. OAFI Osteoarthritis Foundation International. Available at: <https://oafifoundation.com/en/what-is-osteoarthritis/>
2. Goldring SR, Goldring MB. Changes in the osteochondral unit during osteoarthritis: structure, function and cartilage–bone crosstalk. *Nature Reviews Rheumatology*. novembre 2016;12(11):632–44.
3. Neogi T. The epidemiology and impact of pain in osteoarthritis. *Osteoarthritis and Cartilage*. settembre 2013;21(9):1145–53.
4. Wong M, Carter DR. Articular cartilage functional histomorphology and mechanobiology: a research perspective. *Bone*. luglio 2003;33(1):1–13.
5. Gs M. Osteoarthritis pathogenesis – a complex process that involves the entire joint. 2014;7(1):5.
6. Rönn K, Reischl N, Gautier E, Jacobi M. Current Surgical Treatment of Knee Osteoarthritis. *Arthritis*. 26 aprile 2011;2011:1–9.
7. Bittner SM, Smith BT, Diaz-Gomez L, Hudgins CD, Melchiorri AJ, Scott DW, et al. Fabrication and mechanical characterization of 3D printed vertical uniform and gradient scaffolds for bone and osteochondral tissue engineering. *Acta Biomaterialia*. maggio 2019;90:37–48.
8. Temenoff JS, Mikos AG. Review: tissue engineering for regeneration of articular cartilage. *Biomaterials*. marzo 2000;21(5):431–40.
9. Castro NJ, Hacking SA, Zhang LG. Recent Progress in Interfacial Tissue Engineering Approaches for Osteochondral Defects. *Annals of Biomedical Engineering*. agosto 2012;40(8):1628–40.
10. Zhang L, Hu J, Athanasiou KA. The Role of Tissue Engineering in Articular Cartilage Repair and Regeneration. *Critical Reviews™ in Biomedical Engineering*. 2009;37(1–2):1–57.
11. Ryan Longley, Ana Marina Ferreira and Piergiorgio Gentile. Recent Approaches to the Manufacturing of Biomimetic Multi-Phasic Scaffolds for Osteochondral Regeneration. *Molecular Science*. 13 giugno 2018;
12. Jeon JE, Vaquette C, Theodoropoulos C, Klein TJ, Hutmacher DW. Multiphasic construct studied in an ectopic osteochondral defect model. *Journal of The Royal Society Interface*. 2 aprile 2014;11(95):20140184–20140184.
13. Seo S-J, Mahapatra C, Singh RK, Knowles JC, Kim H-W. Strategies for osteochondral repair: Focus on scaffolds. *Journal of Tissue Engineering*. 21 febbraio 2014;5:204173141454185.
14. Kilic Bektas C, Kimiz I, Sendemir A, Hasirci V, Hasirci N. A bilayer scaffold prepared from collagen and carboxymethyl cellulose for skin tissue engineering applications. *Journal of Biomaterials Science, Polymer Edition*. 22 settembre 2018;29(14):1764–84.

15. Yan L-P, Silva-Correia J, Oliveira MB, Vilela C, Pereira H, Sousa RA, et al. Bilayered silk/silk-nanoCaP scaffolds for osteochondral tissue engineering: In vitro and in vivo assessment of biological performance. *Acta Biomaterialia*. gennaio 2015;12:227–41.
16. Chen W-H, Liu Y-Y, Zhang F-H, Yu Y-Z, Chen H-P, Hu Q-X. Osteochondral integrated scaffolds with gradient structure by 3D printing forming. *International Journal of Automation and Computing*. aprile 2015;12(2):220–8.
17. Alexander PG, Gottardi R, Lin H, Lozito TP, Tuan RS. Three-dimensional osteogenic and chondrogenic systems to model osteochondral physiology and degenerative joint diseases. *Experimental Biology and Medicine*. settembre 2014;239(9):1080–95.
18. Jaconi M, Gridavilla G, Pagni F, Munegato D, Zatti G. Istopatologia della patologia artrosica. :29.
19. Cristofolini L, Femiano A. MECCANICA DEI TESSUTI BIOLOGICI LM. :101.
20. Czeakańska EM. In vitro cell and culture models for osteoblasts and their progenitors. :297.
21. Joseph Feher. Osteoclasts resorb bone. In: *Quantitative Human Physiology*. Second.
22. Javad Parvizi MD. Osteoclasts basic and Hystology. *High Yield orthopaedics*.
23. Madry H, van Dijk CN, Mueller-Gerbl M. The basic science of the subchondral bone. *Knee Surgery, Sports Traumatology, Arthroscopy*. aprile 2010;18(4):419–33.
24. Milz S, Eckstein F, Putz R. The thickness of the subchondral plate and its correlation with the thickness of the uncalcified articular cartilage in the human patella. *Anat Embryol [Internet]*. novembre 1995 [citato 21 maggio 2019];192(5). Available at: <http://link.springer.com/10.1007/BF00240376>
25. Milz S, Eckstein F, Putz R. Thickness distribution of the subchondral mineralization zone of the trochlear notch and its correlation with the cartilage thickness: an expression of functional adaptation to mechanical stress acting on the humeroulnar joint? :9.
26. Müller-Gerbl M, Putz R, Hodapp N, Schulte E, Wimmer B. Computed tomography-osteodensitometry for assessing the density distribution of subchondral bone as a measure of long-term mechanical adaptation in individual joints. *Skeletal Radiol*. novembre 1989;18(7):507–12.
27. Burch J, Rice S, Yang H, Neilson A, Stirk L, Francis R, et al. Systematic review of the use of bone turnover markers for monitoring the response to osteoporosis treatment: the secondary prevention of fractures, and primary prevention of fractures in high-risk groups. *Health Technology Assessment [Internet]*. febbraio 2014 [citato 21 maggio 2019];18(11). Available at: <https://www.journalslibrary.nihr.ac.uk/hta/hta18110/>
28. Zhang Y, Wang F, Tan H, Chen G, Guo L, Yang L. Analysis of the Mineral Composition of the Human Calcified Cartilage Zone. *Int J Med Sci*. 2012;9(5):353–60.
29. Poole AR, Kojima T, Yasuda T, Mwale F, Kobayashi M, Laverty S. Composition and Structure of Articular Cartilage: A Template for Tissue Repair. *Clinical Orthopaedics and Related Research*. ottobre 2001;391:S26–33.

30. Vyas C, Poologasundarampillai G, Hoyland J, Bartolo P. 3D printing of biocomposites for osteochondral tissue engineering. In: *Biomedical Composites* [Internet]. Elsevier; 2017 [citato 26 giugno 2019]. pag. 261–302. Available at: <https://linkinghub.elsevier.com/retrieve/pii/B9780081007525000135>
31. Hunziker EB, Quinn TM, Häuselmann H-J. Quantitative structural organization of normal adult human articular cartilage. *Osteoarthritis and Cartilage*. luglio 2002;10(7):564–72.
32. Matsiko A, Levingstone T, O'Brien F. Advanced Strategies for Articular Cartilage Defect Repair. *Materials*. 22 febbraio 2013;6(2):637–68.
33. Hsieh Y-H, Shen B-Y, Wang Y-H, Lin B, Lee H-M, Hsieh M-F. Healing of Osteochondral Defects Implanted with Biomimetic Scaffolds of Poly(ϵ -Caprolactone)/Hydroxyapatite and Glycidyl-Methacrylate-Modified Hyaluronic Acid in a Minipig. *International Journal of Molecular Sciences*. 9 aprile 2018;19(4):1125.
34. Nguyen LH, Kudva AK, Saxena NS, Roy K. Engineering articular cartilage with spatially-varying matrix composition and mechanical properties from a single stem cell population using a multi-layered hydrogel. *Biomaterials*. ottobre 2011;32(29):6946–52.
35. Allen KD, Golightly YM. State of the evidence: Current Opinion in Rheumatology. *maggio 2015*;27(3):276–83.
36. Zhang Y, Jordan JM. Epidemiology of Osteoarthritis. *Clinics in Geriatric Medicine*. agosto 2010;26(3):355–69.
37. Lawrence RC, Felson DT, Helmick CG, Arnold LM, Choi H, Deyo RA, et al. Estimates of the prevalence of arthritis and other rheumatic conditions in the United States: Part II. *Arthritis & Rheumatism*. gennaio 2008;58(1):26–35.
38. Hootman JM, Helmick CG. Projections of US prevalence of arthritis and associated activity limitations. *Arthritis & Rheumatism*. gennaio 2006;54(1):226–9.
39. Amirah Al Idrus. Research Nanoparticle injection wards off osteoarthritis in injured mice.
40. van Saase JL, van Romunde LK, Cats A, Vandenbroucke JP, Valkenburg HA. Epidemiology of osteoarthritis: Zoetermeer survey. Comparison of radiological osteoarthritis in a Dutch population with that in 10 other populations. *Annals of the Rheumatic Diseases*. 1 aprile 1989;48(4):271–80.
41. Memon AR, Quinlan JF. Surgical Treatment of Articular Cartilage Defects in the Knee: Are We Winning? *Advances in Orthopedics*. 2012;2012:1–6.
42. Braun HJ, Gold GE. Diagnosis of osteoarthritis: Imaging. *Bone*. agosto 2012;51(2):278–88.
43. Kellgren JH, Lawrence JS. Radiological Assessment of Osteo-Arthrosis. *Annals of the Rheumatic Diseases*. 1 dicembre 1957;16(4):494–502.
44. Rodríguez-Merchán EC, Gómez-Cardero P. The Outerbridge Classification Predicts the Need for Patellar Resurfacing in TKA. *Clinical Orthopaedics and Related Research®*. maggio 2010;468(5):1254–7.

45. Altman RD, Gold GE. Atlas of individual radiographic features in osteoarthritis, revised. *Osteoarthritis and Cartilage*. 2007;15:A1–56.
46. Akizuki S, Mow VC, Müller F, Pita JC, Howell DS, Manicourt DH. Tensile properties of human knee joint cartilage: I. Influence of ionic conditions, weight bearing, and fibrillation on the tensile modulus: TENSILE MODULUS OF HUMAN KNEE CARTILAGE. *J Orthop Res*. 1986;4(4):379–92.
47. Pritzker KPH, Gay S, Jimenez SA, Ostergaard K, Pelletier J-P, Revell PA, et al. Osteoarthritis cartilage histopathology: grading and staging. *Osteoarthritis and Cartilage*. gennaio 2006;14(1):13–29.
48. Zhou S, Thornhill TS, Meng F, Xie L, Wright J, Glowacki J. Influence of osteoarthritis grade on molecular signature of human cartilage: OSTEOARTHRITIS AND GENE EXPRESSION. *J Orthop Res*. marzo 2016;34(3):454–62.
49. Imhof H, Sulzbacher I, Grampp S, Czerny C, Youssefzadeh S, Kainberger F. Subchondral Bone and Cartilage Disease: A Rediscovered Functional Unit. *Investigative Radiology*. ottobre 2000;35(10):581–8.
50. Sanchez C, Deberg MA, Piccardi N, Msika P, Reginster J-YL, Henrotin YE. Subchondral bone osteoblasts induce phenotypic changes in human osteoarthritic chondrocytes. *Osteoarthritis and Cartilage*. novembre 2005;13(11):988–97.
51. Goldring SR. Alterations in periarticular bone and cross talk between subchondral bone and articular cartilage in osteoarthritis. *Therapeutic Advances in Musculoskeletal Disease*. agosto 2012;4(4):249–58.
52. Bradley JD. Comparison of an antiinflammatory dose of ibuprofen, an analgesic dose of ibuprofen, and acetaminophen in the treatment of patients with osteoarthritis of the knee. In 1991.
53. Felson DT. Osteoarthritis: New Insights. Part 2: Treatment Approaches. *Annals of Internal Medicine*. 7 novembre 2000;133(9):726.
54. Gomoll AH, Filardo G, de Girolamo L, Esprequeira-Mendes J, Marcacci M, Rodkey WG, et al. Surgical treatment for early osteoarthritis. Part I: cartilage repair procedures. *Knee Surgery, Sports Traumatology, Arthroscopy*. marzo 2012;20(3):450–66.
55. Gill TJ, Macgillivray JD. The technique of microfracture for the treatment of articular cartilage defects in the knee. *Operative Techniques in Orthopaedics*. aprile 2001;11(2):105–7.
56. Mithoefer K, Iii RJW, Warren RF, Potter HG, Spock CR, Jones EC, et al. Chondral Resurfacing of Articular Cartilage Defects in the Knee with the Microfracture Technique. 2006;88:11.
57. Benya P. Dedifferentiated chondrocytes reexpress the differentiated collagen phenotype when cultured in agarose gels. *Cell*. agosto 1982;30(1):215–24.
58. Nash WJ, Al-Nammari S, Khan WS, Pengas IP. Surgical Management of the Forefoot in Patients with Rheumatoid Arthritis - A Review Article. *The Open Orthopaedics Journal*. 31 marzo 2015;9(1):78–83.

59. Swieszkowski W, Tuan BHS, Kurzydowski KJ, Hutmacher DW. Repair and regeneration of osteochondral defects in the articular joints. *Biomolecular Engineering*. novembre 2007;24(5):489–95.
60. Orthopaedic Research and Biotechnology, Research Building, The Children’s Hospital at Westmead, Locked Bag 4001, Westmead, NSW 2145, Australia, Murphy C, O’Brien F, Little D, Schindeler A. Cell-scaffold interactions in the bone tissue engineering triad. *eCM*. 20 settembre 2013;26:120–32.
61. Mhanna R, Hasan A. *Introduction to Tissue Engineering*. :32.
62. Beaman JJ. *3D Printing, Additive Manufacturing, and Solid Freeform Fabrication: The Technologies of the Past, Present and Future*. :43.
63. Tamayol A, Akbari M, Annabi N, Paul A, Khademhosseini A, Juncker D. Fiber-based tissue engineering: Progress, challenges, and opportunities. *Biotechnology Advances*. settembre 2013;31(5):669–87.
64. Chan BP, Leong KW. Scaffolding in tissue engineering: general approaches and tissue-specific considerations. *Eur Spine J*. dicembre 2008;17(S4):467–79.
65. Khademhosseini A, Langer R. A decade of progress in tissue engineering. *Nat Protoc*. ottobre 2016;11(10):1775–81.
66. Nukavarapu SP, Dorcemus DL. Osteochondral tissue engineering: Current strategies and challenges. *Biotechnology Advances*. settembre 2013;31(5):706–21.
67. Torres-Sanchez C, Al Mushref FRA, Norrito M, Yendall K, Liu Y, Conway PP. The effect of pore size and porosity on mechanical properties and biological response of porous titanium scaffolds. *Materials Science and Engineering: C*. agosto 2017;77:219–28.
68. JULIAN R. JONES. *Scaffolds for tissue engineering. Biomaterials, Artificial Organs and Tissue Engineering*. 2005;
69. Chu CR. *Articular cartilage repair using allogeneic perichondrocyte-seeded biodegradable porous polylactic acid (PLA): a tissue-engineering study*. 1995;
70. Malda J, Woodfield TBF, van der Vloodt F, Wilson C, Martens DE, Tramper J, et al. The effect of PEGT/PBT scaffold architecture on the composition of tissue engineered cartilage. *Biomaterials*. gennaio 2005;26(1):63–72.
71. Deng T, Lv J, Pang J, Liu B, Ke J. Construction of tissue-engineered osteochondral composites and repair of large joint defects in rabbit: TE osteochondral composites repair large defect in joint. *J Tissue Eng Regen Med*. luglio 2012;n/a-n/a.
72. Hung CT, Lima EG, Mauck RL, Takai E, LeRoux MA, Lu HH, et al. Erratum to “Anatomically shaped osteochondral constructs for articular cartilage repair” [*J. Biomech*. 36 (2004) 1853–1864]. *Journal of Biomechanics*. dicembre 2004;37(12):1953.
73. Dorcemus DL, Nukavarapu SP. *Novel and Unique Matrix Design for Osteochondral Tissue Engineering*. *MRS Proceedings [Internet]*. 2014 [citato 30 maggio 2019];1621. Available at: http://www.journals.cambridge.org/abstract_S1946427414002851

74. Li X, Ding J, Wang J, Zhuang X, Chen X. Biomimetic biphasic scaffolds for osteochondral defect repair. *Regenerative Biomaterials*. settembre 2015;2(3):221–8.
75. Schek RM. Engineered Osteochondral Grafts Using Biphasic Composite Solid Free-Form Fabricated Scaffolds. :11.
76. O'Reilly A, Kelly DJ. A Computational Model of Osteochondral Defect Repair Following Implantation of Stem Cell-Laden Multiphase Scaffolds. *Tissue Engineering Part A*. gennaio 2017;23(1–2):30–42.
77. Han F, Zhou F, Yang X, Zhao J, Zhao Y, Yuan X. A pilot study of conically graded chitosan-gelatin hydrogel/PLGA scaffold with dual-delivery of TGF- β 1 and BMP-2 for regeneration of cartilage-bone interface: CONICALLY GRADED SCAFFOLD OF HYDROGEL/PLGA. *Journal of Biomedical Materials Research Part B: Applied Biomaterials*. ottobre 2015;103(7):1344–53.
78. Clearfield D. Biomimetic multidirectional scaffolds for zonal osteochondral tissue engineering via a lyophilization bonding approach. 2018;
79. Levingstone TJ, Matsiko A, Dickson GR, O'Brien FJ, Gleeson JP. A biomimetic multi-layered collagen-based scaffold for osteochondral repair. *Acta Biomaterialia*. maggio 2014;10(5):1996–2004.
80. Li X, Li Y, Zuo Y, Qu D, Liu Y, Chen T, et al. Osteogenesis and chondrogenesis of biomimetic integrated porous PVA/gel/V-n-HA/pa6 scaffolds and BMSCs construct in repair of articular osteochondral defect: PVA/Gel/V-n-HA/pa6 Scaffolds and BMSCS Construct. *Journal of Biomedical Materials Research Part A*. ottobre 2015;103(10):3226–36.
81. Nguyen LH, Kudva AK, Guckert NL, Linse KD, Roy K. Unique biomaterial compositions direct bone marrow stem cells into specific chondrocytic phenotypes corresponding to the various zones of articular cartilage. *Biomaterials*. febbraio 2011;32(5):1327–38.
82. Yousefi A-M, Hoque ME, Prasad RGSV, Uth N. Current strategies in multiphasic scaffold design for osteochondral tissue engineering: A review: Current Strategies in Multiphasic Scaffold Design. *Journal of Biomedical Materials Research Part A*. luglio 2015;103(7):2460–81.
83. Kim SH, Kim SH, Jung Y. Bi-layered PLCL/(PLGA/ β -TCP) composite scaffold for osteochondral tissue engineering. *Journal of Bioactive and Compatible Polymers*. marzo 2015;30(2):178–87.
84. Sartori M, Pagani S, Ferrari A, Costa V, Carina V, Figallo E, et al. A new bi-layered scaffold for osteochondral tissue regeneration: In vitro and in vivo preclinical investigations. *Materials Science and Engineering: C*. gennaio 2017;70:101–11.
85. Filardo G, Perdisa F, Gelinsky M, Despang F, Fini M, Marcacci M, et al. Novel alginate biphasic scaffold for osteochondral regeneration: an in vivo evaluation in rabbit and sheep models. *Journal of Materials Science: Materials in Medicine [Internet]*. giugno 2018 [citato 27 giugno 2019];29(6). Available at: <http://link.springer.com/10.1007/s10856-018-6074-0>
86. Tampieri A, Sandri M, Landi E, Pressato D, Francioli S, Quarto R, et al. Design of graded biomimetic osteochondral composite scaffolds. *Biomaterials*. settembre 2008;29(26):3539–46.

87. Levingstone TJ, Thompson E, Matsiko A, Schepens A, Gleeson JP, O'Brien FJ. Multi-layered collagen-based scaffolds for osteochondral defect repair in rabbits. *Acta Biomaterialia*. marzo 2016;32:149–60.
88. Han F, Zhou F, Yang X, Zhao J, Zhao Y, Yuan X. A pilot study of conically graded chitosan-gelatin hydrogel/PLGA scaffold with dual-delivery of TGF- β 1 and BMP-2 for regeneration of cartilage-bone interface: CONICALLY GRADED SCAFFOLD OF HYDROGEL/PLGA. *Journal of Biomedical Materials Research Part B: Applied Biomaterials*. ottobre 2015;103(7):1344–53.
89. Joydip Kundu. Biomaterials for Biofabrication of 3D Tissue Scaffolds. In: *Biodegradable synthetic polymers*. 2013.
90. Gong T, Xie J, Liao J, Zhang T, Lin S, Lin Y. Nanomaterials and bone regeneration. *Bone Research* [Internet]. dicembre 2015 [citato 31 maggio 2019];3(1). Available at: <http://www.nature.com/articles/boneres201529>
91. Yang X, Chen X, Wang H. Acceleration of Osteogenic Differentiation of Preosteoblastic Cells by Chitosan Containing Nanofibrous Scaffolds. *Biomacromolecules*. 12 ottobre 2009;10(10):2772–8.
92. Yang H-W, Lin M-H, Xu Y-Z, Shang G-W, Wang R-R, Chen K. Osteogenesis of bone marrow mesenchymal stem cells on strontium-substituted nano-hydroxyapatite coated roughened titanium surfaces. :8.
93. Zhang L, Webster TJ. Nanotechnology and nanomaterials: Promises for improved tissue regeneration. *Nano Today*. febbraio 2009;4(1):66–80.
94. Ge M, Ge K, Gao F, Yan W, Liu H, Xue L, et al. Biomimetic mineralized strontium-doped hydroxyapatite on porous poly(L-lactic acid) scaffolds for bone defect repair. *International Journal of Nanomedicine*. marzo 2018;Volume 13:1707–21.
95. Kim J-W, Shin K-H, Koh Y-H, Hah MJ, Moon J, Kim H-E. Production of Poly(ϵ -Caprolactone)/Hydroxyapatite Composite Scaffolds with a Tailored Macro/Micro-Porous Structure, High Mechanical Properties, and Excellent Bioactivity. *Materials*. 22 settembre 2017;10(10):1123.
96. Chen B, Sun K. Mechanical and dynamic viscoelastic properties of hydroxyapatite reinforced poly(ϵ -caprolactone). *Polymer Testing*. dicembre 2005;24(8):978–82.
97. Sun N, Shi T, Fan Y, Hu B. Experimental Study on 3D Chi - Hap Scaffolds for Thyroid Cartilage Repairing. *IOP Conference Series: Materials Science and Engineering*. gennaio 2018;301:012018.
98. Kolmas J, Velard F, Jaguszewska A, Lemaire F, Kerdjoudj H, Gangloff SC, et al. Substitution of strontium and boron into hydroxyapatite crystals: Effect on physicochemical properties and biocompatibility with human Wharton-Jelly stem cells. *Materials Science and Engineering: C*. ottobre 2017;79:638–46.
99. Panzavolta S, Torricelli P, Casolari S, Parrilli A, Fini M, Bigi A. Strontium-Substituted Hydroxyapatite-Gelatin Biomimetic Scaffolds Modulate Bone Cell Response. *Macromolecular Bioscience*. luglio 2018;18(7):1800096.

100. Saidak Z, Marie PJ. Strontium signaling: Molecular mechanisms and therapeutic implications in osteoporosis. *Pharmacology & Therapeutics*. novembre 2012;136(2):216–26.
101. Liu D, Nie W, Li D, Wang W, Zheng L, Zhang J, et al. 3D printed PCL/SrHA scaffold for enhanced bone regeneration. *Chemical Engineering Journal*. aprile 2019;362:269–79.
102. Li L, Lu X, Meng Y, Weyant CM. Comparison study of biomimetic strontium-doped calcium phosphate coatings by electrochemical deposition and air plasma spray: morphology, composition and bioactive performance. *Journal of Materials Science: Materials in Medicine*. ottobre 2012;23(10):2359–68.
103. Montesi M, Panseri S, Dapporto M, Tampieri A, Sprio S. Sr-substituted bone cements direct mesenchymal stem cells, osteoblasts and osteoclasts fate. Kim J-E, curatore. *PLOS ONE*. 14 febbraio 2017;12(2):e0172100.
104. Wong KV, Hernandez A. A Review of Additive Manufacturing. *ISRN Mechanical Engineering*. 2012;2012:1–10.
105. Rafiq I. Noorani. *Rapid Prototyping: Principles and Applications*. 2005.
106. Kalsoom U, Nesterenko PN, Paull B. Recent developments in 3D printable composite materials. *RSC Adv*. 2016;6(65):60355–71.
107. Bracaglia LG, Smith BT, Watson E, Arumugasaamy N, Mikos AG, Fisher JP. 3D printing for the design and fabrication of polymer-based gradient scaffolds. *Acta Biomaterialia*. luglio 2017;56:3–13.
108. Neufurth M, Wang X, Wang S, Steffen R, Ackermann M, Haep ND, et al. 3D printing of hybrid biomaterials for bone tissue engineering: Calcium-polyphosphate microparticles encapsulated by polycaprolactone. *Acta Biomaterialia*. dicembre 2017;64:377–88.
109. Sherwood JK, Riley SL, Palazzolo R, Brown SC, Monkhouse DC, Coates M, et al. A three-dimensional osteochondral composite scaffold for articular cartilage repair. *Biomaterials*. dicembre 2002;23(24):4739–51.
110. Gonçalves EM, Oliveira FJ, Silva RF, Neto MA, Fernandes MH, Amaral M, et al. Three-dimensional printed PCL-hydroxyapatite scaffolds filled with CNTs for bone cell growth stimulation. *Journal of Biomedical Materials Research Part B: Applied Biomaterials*. agosto 2016;104(6):1210–9.
111. Kim MH, Yun C, Chalisserry EP, Lee YW, Kang HW, Park S-H, et al. Quantitative analysis of the role of nanohydroxyapatite (nHA) on 3D-printed PCL/nHA composite scaffolds. *Materials Letters*. giugno 2018;220:112–5.
112. Salerno A, Zeppetelli S, Di Maio E, Iannace S, Netti PA. Design of Bimodal PCL and PCL-HA Nanocomposite Scaffolds by Two Step Depressurization During Solid-state Supercritical CO₂ Foaming. *Macromolecular Rapid Communications*. 3 agosto 2011;32(15):1150–6.
113. Verhaegen J, Clockaerts S, Van Osch. TruFit plug for repair of osteochondral defects—where is the evidence? *Review of Literature Cartilage*. 2015;6:12–9.
114. Chondrofix® Osteochondral Allograft Surgical Technique. :16.

115. Kon E, Filardo G, Perdisa F, Venieri G, Marcacci M. Clinical results of multilayered biomaterials for osteochondral regeneration. *Journal of Experimental Orthopaedics* [Internet]. dicembre 2014 [citato 29 maggio 2019];1(1). Available at: <http://www.jeo-esska.com/content/1/1/10>
116. Oliver S. SCHINDLER. Current concepts of articular cartilage repair. 2011;
117. Howard D, BATTERY LD, Shakesheff KM, Roberts SJ. Tissue engineering: strategies, stem cells and scaffolds. *Journal of Anatomy*. luglio 2008;213(1):66–72.
118. Bruder SP, Kurth AA, Shea M, Hayes WC, Jaiswal N, Kadiyala S. Bone regeneration by implantation of purified, culture-expanded human mesenchymal stem cells. *J Orthop Res*. marzo 1998;16(2):155–62.
119. Yang XB, Roach HI, Clarke NMP, Howdle SM, Quirk R, Shakesheff KM, et al. Human osteoprogenitor growth and differentiation on synthetic biodegradable structures after surface modification. *Bone*. dicembre 2001;29(6):523–31.
120. Lian JB, Stein GS. Concepts of Osteoblast Growth and Differentiation: Basis for Modulation of Bone Cell Development and Tissue Formation. *Critical Reviews in Oral Biology & Medicine*. aprile 1992;3(3):269–305.
121. A.B. Ulrich, P.M. Pour. Cell Lines. In: *Encyclopedia of Genetics*,. 2001.
122. Quarles LD, Yohay DA, Lever LW, Caton R, Wenstrup RJ. Distinct proliferative and differentiated stages of murine MC3T3-E1 cells in culture: An in vitro model of osteoblast development. *Journal of Bone and Mineral Research*. 3 dicembre 2009;7(6):683–92.
123. Harris SA, Enger RJ, Riggs LB, Spelsberg TC. Development and characterization of a conditionally immortalized human fetal osteoblastic cell line. *Journal of Bone and Mineral Research*. 3 dicembre 2009;10(2):178–86.
124. Billiau A, Edy VG, Heremans H, Van Damme J, Desmyter J, Georgiades JA, et al. Human Interferon: Mass Production in a Newly Established Cell Line, MG-63. *Antimicrobial Agents and Chemotherapy*. 1 luglio 1977;12(1):11–5.
125. Rodan SB, Imai Y, Thiede MA, Wesolowski G, Thompson D, Bar-Shavit Z, et al. Characterization of a Human Osteosarcoma Cell Line (Saos-2) with Osteoblastic Properties. :7.
126. Ponten J, Saksela E. Two established in vitro cell lines from human mesenchymal tumours. *International Journal of Cancer*. 15 settembre 1967;2(5):434–47.
127. Chang H-I, Wang Y. Cell Responses to Surface and Architecture of Tissue Engineering Scaffolds. In: Eberli D, curatore. *Regenerative Medicine and Tissue Engineering - Cells and Biomaterials* [Internet]. InTech; 2011 [citato 6 giugno 2019]. Available at: <http://www.intechopen.com/books/regenerative-medicine-and-tissue-engineering-cells-and-biomaterials/cell-responses-to-surface-and-architecture-of-tissue-engineering-scaffolds>
128. Gumbiner BM. Cell Adhesion: The Molecular Basis of Tissue Architecture and Morphogenesis. *Cell*. febbraio 1996;84(3):345–57.

129. Wei J, Igarashi T, Okumori N, Igarashi T, Maetani T, Liu B, et al. Influence of surface wettability on competitive protein adsorption and initial attachment of osteoblasts. *Biomed Mater.* agosto 2009;4(4):045002.
130. Jung H, Kwak B, Yang HS, Tae G, Kim J-S, Shin K. Attachment of cells to poly(styrene-co-acrylic acid) thin films with various charge densities. *Colloids and Surfaces A: Physicochemical and Engineering Aspects.* febbraio 2008;313–314:562–6.
131. Hatano K, Inoue H, Kojo T, Matsunaga T, Tsujisawa T, Uchiyama C, et al. Effect of surface roughness on proliferation and alkaline phosphatase expression of rat calvarial cells cultured on polystyrene. *Bone.* ottobre 1999;25(4):439–45.
132. Kim M-H, Kino-oka M, Kawase M, Yagi K, Taya M. Response of human epithelial cells to culture surfaces with varied roughnesses prepared by immobilizing dendrimers with/without d-glucose display. *Journal of Bioscience and Bioengineering.* febbraio 2007;103(2):192–9.
133. Ruprecht V, Monzo P, Ravasio A, Yue Z, Makhija E, Strale PO, et al. How cells respond to environmental cues – insights from bio-functionalized substrates. *Journal of Cell Science.* 1 gennaio 2017;130(1):51–61.
134. Engler AJ, Sen S, Sweeney HL, Discher DE. Matrix Elasticity Directs Stem Cell Lineage Specification. *Cell.* agosto 2006;126(4):677–89.
135. Roh H-S, Myung S-W, Jung S-C, Kim B-H. Fabrication of 3D Scaffolds with Nano-Hydroxyapatite for Improving the Preosteoblast Cell-Biological Performance. *Journal of Nanoscience and Nanotechnology.* 1 agosto 2015;15(8):5585–8.
136. Knudson , Knudson W. *Cartilage proteoglycans.* 2001.
137. K G. Endochondral Ossification in Cartilage Repair Tissue Hampers Bone Marrow Stimulating Techniques. *Rheumatology [Internet].* 2012 [citato 1 luglio 2019];01(S2). Available at: <https://www.omicsonline.org/endochondral-ossification-in-cartilage-repair-tissue-hampers-bone-marrow-stimulating-techniques-2161-1149.S3-002.php?aid=5274>
138. Envision Tec Bioplotter [Internet]. Envision Tec. Available at: <https://envisiontec.com/3d-printers/3d-bioplotter/>
139. Honigs, D. E. *Fourier Transform Infrared Spectrometry.* 1986.
140. Peter R. Griffiths, James A. De Haseth. *Fourier Transform Infrared Spectrometry.* Second Edition.
141. DataPhysics Instruments GmbH Contact angle.
142. Peter Haines SG. *Principles of Thermal Analysis and Calorimetry: Edition 2.*
143. David Dollimore CJK. *An introduction to thermogravimetry.*
144. Longbottom RJ, Monaghan BJ, Chowdhury AA, Reid MH, Zhang G, Mahoney MR, et al. Effect of Mineral Matter on the Reactivity of Coke and its Replication in a Coke Analogue. *ISIJ International.* 2016;56(9):1553–8.
145. M. J. Katz. *Vacuum Microbalance Techniques, Volume 3.*

146. Scanning Electron Microscope A To Z. :32.
147. Anjam Khursheed. Scanning Electron Microscope Optics and Spectrometers.
148. Tursunov O, Dobrowolski J, Klima K, Kordon B, Ryczkowski J, Tylko G, et al. The Influence of Laser Biotechnology on Energetic Value and Chemical Parameters of Rose Multiflora Biomass and Role of Catalysts for bio-energy production from Biomass: Case Study in Krakow-Poland. *World Journal of Environmental Engineering*. :9.
149. Antonis Nanakoudis. Spot size in scanning electron microscopy (SEM): why it matters! ThermoFisher Scientific.
150. A. Beer. Bestimmung der Absorption des rothen Lichts in farbigen Flüssigkeiten. In: *Annalen der Physik und Chemie*. 1852.
151. du Plessis A, Broeckhoven C, Guelpa A, le Roux SG. Laboratory x-ray micro-computed tomography: a user guideline for biological samples. *GigaScience* [Internet]. 1 giugno 2017 [citato 4 giugno 2019];6(6). Available at: <https://academic.oup.com/gigascience/article/doi/10.1093/gigascience/gix027/3737665>
152. Manual for Bruker-microCT CT-Analyser v. 1.13. 2013;1:139.
153. Salmon P. Bruker-MicroCT method note: 3D volume analysis. :19.
154. Gregor T, Kochov P, Eberlov L, Nedorost L, Proseck E, Lika V, et al. Correlating Micro-CT Imaging with Quantitative Histology. In: Goswami T, curatore. *Injury and Skeletal Biomechanics* [Internet]. InTech; 2012 [citato 4 giugno 2019]. Available at: <http://www.intechopen.com/books/injury-and-skeletal-biomechanics/correlating-micro-ct-imaging-with-quantitative-histology>
155. Nv S. NRecon User Manual. 2011;23.
156. Gómez-Lizárraga KK, Flores-Morales C, Del Prado-Audelo ML, Álvarez-Pérez MA, Piña-Barba MC, Escobedo C. Polycaprolactone- and polycaprolactone/ceramic-based 3D-bioplotted porous scaffolds for bone regeneration: A comparative study. *Materials Science and Engineering: C*. ottobre 2017;79:326–35.
157. Human Bone Osteosarcoma Epithelial Cells (U2OS Line) [Internet]. Available at: <https://www.microscopyu.com/gallery-images/human-bone-osteosarcoma-epithelial-cells-u2os-line>
158. Bahuguna A, Khan I, Bajpai VK, Kang SC. MTT assay to evaluate the cytotoxic potential of a drug. *Bangladesh Journal of Pharmacology*. 8 aprile 2017;12(2):8.
159. Cell Proliferation Kit I (MTT) [Internet]. Available at: sigma-aldrich.com
160. MTT Assay Kit (Cell Proliferation) (ab211091) [Internet]. Available at: <https://www.abcam.com/mtt-assay-kit-cell-proliferation-ab211091.html?productWallTab=ShowAll>
161. Kapuscinski J. DAPI: a DNA-Specific Fluorescent Probe. *Biotechnic & Histochemistry*. gennaio 1995;70(5):220–33.

162. Nikon, Filters for Fluorescence Microscopy [Internet]. Available at: <https://www.nikon.com/products/microscope-solutions/explore/microscope-abc/learn-more-microscope/filters/index.htm>
163. Fixation Strategies and Formulations Used in IHC Staining. ThermoFisher Scientific [Internet]. Available at:) <https://www.thermofisher.com/it/en/home/life-science/protein-biology/protein-biology-learning-center/protein-biology-resource-library/pierce-protein-methods/fixation-strategies-formulations.html>
164. Comis SD, Pickles JO, Osborne MP. Osmium tetroxide postfixation in relation to the crosslinkage and spatial organization of stereocilia in the guinea-pig cochlea. *Journal of Neurocytology*. 1 febbraio 1985;14(1):113–30.
165. Mary Johnson. Detergents: Triton X-100, Tween-20, and More. Labome, the world of laboratories.
166. BCA Protein Assay Kit, ThermoFisher [Internet]. Available at: <https://www.thermofisher.com/order/catalog/product/23225>
167. y J.S.C. Olson and John Markwell. Assays for Determination of Protein Concentration UNIT 3.4. In: *Current Protocols in Protein Science*. 2008.
168. TrypLE Reagents, ThermoFisher [Internet]. Available at: <https://www.thermofisher.com/it/en/home/life-science/cell-culture/mammalian-cell-culture/reagents/trypsin/tryple-express.html>
169. Z. Marczenko. Separation, Preconcentration and Spectrophotometry in Inorganic Analysis. *Analytical Spectroscopy Library* 10(4). gennaio 2002;
170. Upton G. & Cook I. *A Dictionary of Statistics*. 2006.
171. Shoja M, Shameli K, Ahmad MB, Zakaria Z. PREPARATION AND CHARACTERIZATION OF POLY (ϵ - CAPROLACTONE)/TiO₂ MICRO-COMPOSITES. :7.
172. Berzina-Cimdina L, Borodajenko N. Research of Calcium Phosphates Using Fourier Transform Infrared Spectroscopy. In: Theophanides T, curatore. *Infrared Spectroscopy - Materials Science, Engineering and Technology* [Internet]. InTech; 2012 [citato 6 maggio 2019]. Available at: <http://www.intechopen.com/books/infrared-spectroscopy-materials-science-engineering-and-technology/research-of-calcium-phosphates-using-fourier-transformation-infrared-spectroscopy>
173. Aliah NN, Ansari MNM. Thermal analysis on Characterization of Polycaprolactone (PCL) – Chitosan Scaffold for Tissue Engineering. 2017;6(2):5.
174. Jain S. *PROCESSING OF HYDROXYAPATITE BY BIOMIMETIC PROCESS*. 2010;46.
175. Waveland Press. *Mechanical Behavior of Materials*. 2005.
176. Bahuguna A, Khan I, Bajpai VK, Kang SC. MTT assay to evaluate the cytotoxic potential of a drug. *Bangladesh Journal of Pharmacology*. 8 aprile 2017;12(2):8.
177. Allion A, Baron J-P, Boulange-Petermann L. Impact of surface energy and roughness on cell distribution and viability. *Biofouling*. gennaio 2006;22(5):269–78.

178. Dávila JL, Freitas MS, Inforçatti Neto P, Silveira ZC, Silva JVL, d'Ávila MA. Fabrication of PCL/ β -TCP scaffolds by 3D mini-screw extrusion printing. *Journal of Applied Polymer Science*. 15 aprile 2016;133(15):n/a-n/a.
179. Nyberg E, Rindone A, Dorafshar A, Grayson WL. Comparison of 3D-Printed Poly- ϵ -Caprolactone Scaffolds Functionalized with Tricalcium Phosphate, Hydroxyapatite, Bio-Oss, or Decellularized Bone Matrix <sup/>. *Tissue Engineering Part A*. giugno 2017;23(11–12):503–14.
180. Nava MM, Draghi L, Giordano C, Pietrabissa R. The effect of scaffold pore size in cartilage tissue engineering. *JABFM*. 2016;14(3):0–0.
181. Akay G, Birch MA, Bokhari MA. Microcellular polyHIPE polymer supports osteoblast growth and bone formation in vitro. *Biomaterials*. agosto 2004;25(18):3991–4000.
182. Speirs M, Humbeeck JVan, Schrooten J, Luyten J, Kruth JP. The Effect of Pore Geometry on the Mechanical Properties of Selective Laser Melted Ti-13Nb-13Zr Scaffolds. *Procedia CIRP*. 2013;5:79–82.
183. Choi K, Kuhn JL, Ciarelli MJ, Goldstein SA. The elastic moduli of human subchondral, trabecular, and cortical bone tissue and the size-dependency of cortical bone modulus. *Journal of Biomechanics*. gennaio 1990;23(11):1103–13.
184. Tanck E, Van Donkelaar CC, Jepsen KJ, Goldstein SA, Weinans H, Burger EH, et al. The mechanical consequences of mineralization in embryonic bone. *Bone*. luglio 2004;35(1):186–90.
185. Mente PL, Lewis JL. Elastic modulus of calcified cartilage is an order of magnitude less than that of subchondral bone. *Journal of Orthopaedic Research*. settembre 1994;12(5):637–47.
186. Scandelli G. Caratterizzazione meccanica scaffold per tessuti ossei realizzati con stampa 3D e validazione modello computazionale. :87.
187. Hutmacher DW, Schantz T, Zein I, Ng KW, Teoh SH, Tan KC. Mechanical properties and cell cultural response of polycaprolactone scaffolds designed and fabricated via fused deposition modeling. *Journal of Biomedical Materials Research*. maggio 2001;55(2):203–16.
188. Huang B, Caetano G, Vyas C, Blaker J, Diver C, Bártolo P. Polymer-Ceramic Composite Scaffolds: The Effect of Hydroxyapatite and β -tri-Calcium Phosphate. *Materials*. 14 gennaio 2018;11(1):129.
189. Klammert U, Gbureck U, Vorndran E, Rödiger J, Meyer-Marcotty P, Kübler AC. 3D powder printed calcium phosphate implants for reconstruction of cranial and maxillofacial defects. *Journal of Cranio-Maxillofacial Surgery*. dicembre 2010;38(8):565–70.
190. Kamarajan BP, Murugan R, Muthusamy A. Evaluation of selective laser sintered polyamide/hydroxyapatite composite compositions –in vitro and in vivo. 2017;9.
191. Katsen-Globa A, Peter L, Zöllner S, Dörge T, Daffertshofer M, Preckel H, et al. A Novel Approach for Automated Analysis of Cell Attachment and Spreading Based on Backscattered Electron Imaging by Scanning Electron Microscopy. *Materials*. 24 settembre 2009;2(3):1402–16.

192. Gentile F, Tirinato L, Battista E, Causa F, Liberale C, di Fabrizio EM, et al. Cells preferentially grow on rough substrates. *Biomaterials*. ottobre 2010;31(28):7205–12.
193. Harris H. The human alkaline phosphatases: What we know and what we don't know. *Clinica Chimica Acta*. gennaio 1990;186(2):133–50.